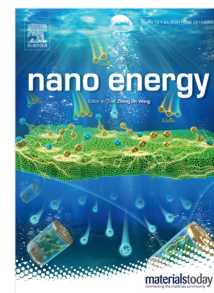


## Journal Pre-proof

Comparison of miniaturized mechanical and osmotic energy harvesting systems

Nan Wu, Timothée Derkenne, Corentin Tregouet, Annie Colin



PII: S2211-2855(23)00841-8  
DOI: <https://doi.org/10.1016/j.nanoen.2023.109004>  
Reference: NANOEN 109004

To appear in: *Nano Energy*

Received date: 1 May 2023  
Revised date: 22 August 2023  
Accepted date: 19 October 2023

Please cite this article as: N. Wu, T. Derkenne, C. Tregouet et al., Comparison of miniaturized mechanical and osmotic energy harvesting systems, *Nano Energy* (2023), doi: <https://doi.org/10.1016/j.nanoen.2023.109004>.

This is a PDF file of an article that has undergone enhancements after acceptance, such as the addition of a cover page and metadata, and formatting for readability, but it is not yet the definitive version of record. This version will undergo additional copyediting, typesetting and review before it is published in its final form, but we are providing this version to give early visibility of the article. Please note that, during the production process, errors may be discovered which could affect the content, and all legal disclaimers that apply to the journal pertain.

© 2023 Elsevier Ltd. All rights reserved.

# Comparison of miniaturized mechanical and osmotic energy harvesting systems

Nan Wu, Timothée Derkenne, Corentin Tregouet, Annie Colin<sup>1,\*</sup>

*ESPCI Paris, PSL Research University, MIE-CBI, CNRS UMR 8231,10, Rue Vauquelin, F-75231 Paris Cedex 05, France*

---

## Abstract

IoT stands for Internet of Things. It refers to the network of physical objects or "things" embedded with sensors, softwares, and other technologies that enable them to connect and exchange data with other devices and systems over the internet. The IoT has the potential to transform many areas of our lives, including home automation, healthcare, transportation, manufacturing, etc. By collecting and analyzing data from connected devices, businesses and organizations can gain insights that can help them make better decisions, improve efficiency, and reduce costs. Naturally, IoT requires energy to work and many techniques have been developed to limit the power consumption of the devices. These objects now need very little power to work, of the order of the mW or the  $\mu$ W. However, the IoT devices need to run for long periods of time without being replaced or recharged. This is especially important for devices deployed in remote or hard-to-reach locations. In this framework, it is of great importance to develop energy harvesting systems for IoT. It is of prime importance to use energy from their environment rather than relying on conventional power sources like batteries or mains electricity. By reducing the need for disposable batteries, energy harvesting can help to reduce waste and minimize the environmental impact of IoT devices. Energy can be found in ambient light, temperature differences, vibrations, or electromagnetic radiation. In this review article we will focus on the recovery of energy from mechanical vibrations and on the recovery of mixing energy: these methods have in common to be based on material surface charges. We will detail different modes of operation: the realization of sensors that do not need power, the realization of energy recovery generators which store energy for sensor consumption, and finally the realization of energy recovery generators feeding directly sensors. We will describe the different physical mechanisms of these processes. We will then illustrate them with examples of outstanding achievements.

*Keywords:* Energy Harvesting for IoT, Osmotic energy, Electrets, Triboelectricity, Piezoelectricity, Electrostriction

---

## 1. Introduction

The Internet of Things (IoT) refers to a network of intelligent objects which are able to collect information, communicate, exchange data and possibly react towards environmental changes[1, 2, 3]. In addition to the conventional electronic objects, such as computers, tablets, and smart phones, IoT could also connect ordinary physical objects of all scales which are embedded with sensors, and living objects as humans and animals. The conception of IoT could facilitate automation process and thus derive new ser-

vices and applications. The IoT market has maintained rapid growth in recent years, with its market size reaching 650 billion USD by the year of 2026, corresponding to a compound annual growth rate (CAGR) of 16.7%[4]. In terms of application areas, the IoT market is segmented into industries including healthcare, agriculture, automotive, manufacturing, predictive maintenance[5] and smart cities. According to a report by MarketsandMarkets, the healthcare IoT market is expected to reach USD 158.07 billion by 2025, growing at a CAGR of 30.8% from 2020 to 2025[4]. The IoT industry is a fast-growing and promising market with a wide range of applications and opportunities.

---

\*Corresponding author

In terms of electrical consumption, the IoT-related energy is estimated to be around 200 TWh per year in 2025, which corresponds to 0.7% share of the global electrical consumption[6]. Considering an estimation of 40 billion connected objects in 2025, the energy consumption in IoT is estimated to be 0.6 mW per device, which is considered as a rather low consumption. However, most of these devices need to operate disconnected from the electrical grid for an extended working time, in conditions where battery replacement is impractical. Such is the case for vibration and stress sensors inserted in bridge structures or for medical use. Thus, development of miniaturized power supply systems for intelligent IoT objects remains a key issue [7].

To tackle the above-mentioned power-supply problem, the first step is to reduce power consumption. Various factors can affect IoT power consumption. By choosing suitable hardware devices, i.e., microcontrollers, sensors, and wireless modules, it is possible to manage power consumption and extend the device battery life. The communication protocols used in IoT devices can also affect power consumption. For example, compared with Wi-Fi and cellular connectivity, Bluetooth or Zigbee consume much less power, which are certainly more suitable for low-power applications. Additionally, sending data at high frequencies would quickly drain the device's battery: it is thus important to optimize data transmission and minimize the frequency of data transfers. In the last decades, significant progress was achieved in electronics technologies for the development of ultra-low consumption devices. To name of few, the Phoenix processor has a sleep power consumption of only 3 pW in sleep mode and 200 nW in active mode[8], and Lin et al. developed a temperature sensor which consumes only 220 nW[9].

The second step is to design self-powered IoT objects by integrating energy harvesting systems to exploit energy sources in surrounding environments. Such design could decrease or even eliminate the use of batteries in IoT objects. In fact, large quantities of untapped energy sources could be considered for IoT objects powering. These sources either come from human activities or derive from ambient energies, such as chemical energy (chemistry, biochemistry), thermal energy (fatal heat, temperature gradients, variations), radiant energy (sun, infrared, radio frequencies) and mechanical sources (vibrations, deformations)[10]. The energy-harvesting process extracts energy from the surrounding environment and

converts it into electrical energy.

A natural idea is to miniaturize the existing mature technologies for energy harvesting, such as wind technology. However, due to its bulky and complex structure, the miniaturization remains difficult. Considering the energy densities of untapped sources, outdoor solar energy is the highest energy source with a power density of  $15,000 \mu\text{W}\cdot\text{cm}^{-3}$ [10]. It drops to  $100 \mu\text{W}\cdot\text{cm}^{-3}$  for indoor environments. The theoretical limit of solar cell on a single junction is 29.1%. The world record for solar-cell efficiency of 46% was achieved by using multi-junction concentration cells[11]. Based on exotic materials such as gallium arsenide, this technology remains until now economically non-viable.

The second untapped environmental energy source is mechanical vibrations which can be found almost everywhere, from human bodies to industrial installations. The source of mechanical energy can be a vibrating structure (a bridge, a building, a window in a noisy street) or a moving object (a washing machine). Each vibration is characterized by a frequency  $f$  and an amplitude of oscillations  $Y_0$ . The mechanical power generated by vibrations can be harvested using an inertial device composed of a seismic mass  $m$  and a spring with an elastic constant  $k$ . In such a device, the amount of power generated is proportional to the cube of the vibration frequency. The generated power writes  $\frac{mY_0^2 8\pi^3 f^3}{4\xi}$  where  $\xi$  is the damping factor[12]. Using this framework, we can estimate the power of classical vibrations in daily life. For example, common activities as walking corresponds to a source of mechanical energy with a power of 67 W, breathing of 0.83 W, finger typing of 0.01 W. These values correspond to the energy consumption of the IoT objects. A typical harvesting power density is of the order of  $100 \mu\text{W}/\text{cm}^3$ [13].

Close to mechanical energy, osmotic energy is considered as the third ambient environmental sources. When  $1 \text{ cm}^3$  of river water is mixed with  $1 \text{ cm}^3$  of sea water, an energy of 2.73 J is released. Considering all the rivers and effluents running to the sea, a global power of around 2 Terawatts is estimated, which corresponds to 75% of the world's electrical power consumption in 2021[14, 15]. The current devices for the recovery of osmotic energy based on selective membranes enable the recovery of  $100 \mu\text{W}\cdot\text{cm}^{-2}$ , which makes this form of energy, nicknamed blue energy, the second most important source of recoverable energy on a par with the energy recoverable from mechanical vibrations. Thermal gradient, thermal variation,

Infrared sources, radio frequency are energy sources present in our environment but at lower available energy levels [16]. For this reason, and because the corresponding harvesting technologies are less mature, we have decided not to deal with them here. Mechanical vibrations and osmotic energy seem to be suitable energy sources to power sensors. The potentially recoverable values are in agreement with power demand of IoT objects. In this review, we will focus on energy-harvesting systems both for mechanical-vibration energy sources and osmotic energy sources.

They have indeed a lot in common since they are both based on surface-charge effect. Several technologies have been developed for converting mechanical waste energy. They present different advantages or disadvantages, in particular according to the intended application. A classic principle for converting mechanical vibrations into electricity is to use electromagnetic generators. The operating principle of an electromagnetic mechanical vibration energy sensor involves the use of a magnet, a coil and a mass-spring system [17]. When the sensor is subjected to mechanical vibrations, the mass-spring system undergoes oscillations, causing the magnet and coil to move relatively to each other. This relative movement induces a changing magnetic flux through the coil in accordance with Faraday's law of electromagnetic induction. The changing magnetic flux induces an electromotive force (EMF) in the coil, generating a voltage across it. This voltage can be used to pass an electric current through a load, for example to charge a battery or power electronic devices. Electromagnetic energy generation is a well-established technology, and the use of this transduction mechanism in small-scale energy harvesting applications is the subject of much research. Fundamental principles and analysis of generators tested to date clearly show that electromagnetic devices do not lend themselves to downscaling [18]. The normalized power measured for an acceleration of  $1\text{m}\cdot\text{s}^{-2}$  is less than  $0.5\mu\text{W cm}^{-3}$  and decreases for smaller size [17]. For this reason, we have decided not to mention these generators in the review and to focus on piezoelectric device, electrostrictive materials, electrets device and triboelectricity.

In all these situations, vibrations induce an alternative capacitive current that requires rectification before use.

In the osmotic energy situation, selective membranes or highly charged membranes are used to produce an ionic flux which is converted at the elec-

trode level into an electronic current. The electrodes can be capacitive (generation of an alternative current) or faradaic (generation of a continuous current). In this review, we will focus on the development of energy-harvesting systems to power miniaturized sensors based on material surface charge. In each case, we will describe the main working principles, discuss the limitations and advantages, and then illustrate the process by describing practical applications. There are numerous reviews in the literature on each of these technologies (see [19, 20, 21, 22] for triboelectric nanogenerators, [23, 24, 25, 26] for piezoelectric device, [27, 28, 29] for electrostrictive materials, [30, 15, 31] for osmotic energy). The originality of our work consists in presenting 4 different energy-recovery modes and comparing them.

## 2. Mechanical vibration energy harvesting using piezoelectric materials for sensor powering

### 2.1. Piezoelectricity

Piezoelectricity was discovered by Pierre and Jacques Curie in 1880 while studying quartz and tourmaline crystals [32]. Piezoelectric materials have the ability to produce voltage when deformed due to vibrations (direct effect). Conversely, they deform when subjected to an externally applied voltage (inverse effect).

Piezoelectricity originates from the distribution of ions of certain crystals. A piezoelectrical crystal has no center of symmetry [33, 34]. In the absence of deformation, the electric dipoles created by the charge distribution cancel each other out exactly, which leads to the absence of net charge on the crystal faces. When the crystal is compressed, the absence of a center of symmetry of the lattice induces that the barycenters of the positive and negative charges no longer coincide. In this case, the electric dipoles no longer cancel each other out, which leads to the appearance of net positive and negative charges on the opposite sides of the crystal.

There are 32 crystallographic classes, out of which 21 are non-centrosymmetric (lacking center of symmetry). 20 of them exhibit direct piezoelectricity, with the 21st one being the cubic class [35]. However, in most cases, these materials are not a perfect crystal. This is always the case with polymers which are never in a monocrystalline form. To obtain a piezoelectric response of these materials, it is necessary to orientate the dipoles in the material at rest.

This requires an important process called "poling" during which the molecular dipoles of the material are reoriented by exerting a high electric field in the range of 5-100 MV m<sup>-1</sup> at high temperature (300 oC), followed by a subsequent cooling.

The electro-mechanical behavior of piezoelectric materials can be described by two constitutive equations.

$$S = [s^E]T + [d]E \quad (1)$$

$$D = [d^t]T + [\epsilon^T]E \quad (2)$$

where  $S$  is the strain tensor, vector  $D$  is the dielectric displacement vector in N.mV<sup>-1</sup> or C.m<sup>-2</sup>,  $[\epsilon^T]$  is the permittivity tensor,  $[s^E]$  the elastic compliance tensor,  $E$  is the applied electric field vector in V.m<sup>-1</sup>, and  $T$  is the shear stress. The superscripts  $T$  and  $E$  indicate that the quantity is measured at constant stress and constant electric field, respectively.  $[d]$  is the direct piezoelectric-effect matrix,  $[d^t]$  is the matrix which describes the converse piezoelectric effect. In this situation, the superscript  $t$  determines the transposition matrix.

Axis 3 is generally chosen according to the direction of the remanent polarization field. The axes 1, 2 and 3 form a direct trihedron. The piezoelectric-effect matrix  $d$  has coefficients  $d_{ij}$ . The first index  $i$  corresponds to the direction of the electric field, i.e. the direction perpendicular to the electrodes, the second index to the direction of the mechanical action. The material can be used according to the mode 33 or 31 depending on the mechanical stress is perpendicular or parallel to the electrodes. Usually, the mode 33 show better performances in term of electromechanical properties than the mode 31. The electromechanical coefficient  $k_{ij}$  is typically used to attest the quality of the electromechanical conversion. For a mechanical stress perpendicular to the electrodes,  $k_{ij}$  can be expressed as  $k_{ij}^2 = \frac{d_{ij}^2}{\epsilon_{ij}^T s_{ij}^E}$ . The coefficient  $k_{ij}^2$  corresponds to the energy conversion ratio, i.e. the value of the stored electrical energy divided by the input mechanical energy. A high coupling factor  $k_{ij}$  does not necessarily quantify the energy harvesting capability of a material. Instead, it is associated with the efficiency of converting input mechanical or electrical energy into stored electrical or mechanical energy and not energy harvested by the circuit. Piezoelectric energy harvesters, on the other hand, need to convert mechanical energy into useable, or output, electrical energy. Based upon this analysis, Roscow et al [36]

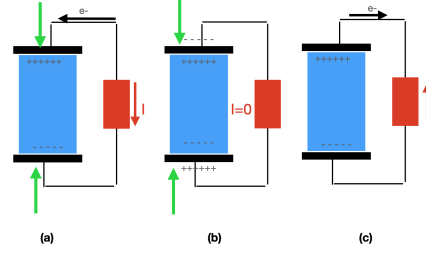


Figure 1: Piezoelectric material based energy harvesting system. (a) The piezoelectric material is loaded between two electrodes. A force is applied on the material and create charges. An electronic current appears to balance these charges. (b) The dipole created by the force is balanced by the charges. The current intensity is zero. (c) the Force is released. The charges go back to their initial position. An inverse electronic current is produced.

defined under applied strain the factor of merit as the ratio of the output harvested energy divided by the input mechanical energy is given by :  $FoM = \frac{d_{ij}^2 Y^2}{\epsilon_{ij}^T}$ .

There are 4 main classes of piezoelectric materials: ceramics (lead zirconate titanate (PZT) [37, 38], BaTiO<sub>3</sub> [39], LiNbO<sub>3</sub> [40]), metal-oxide single crystals (PMN-PT [41, 42] a solid solution of lead-magnesium-niobate (PMN) and lead titanate (PT)) polymers (Polyvinylidene fluoride (PVDF) [43, 44]) and composites (PZT polymer composite[45, 46], BaTiO<sub>3</sub> PDMS composite[47], flexible cellulose nanofibril/MoS<sub>2</sub> nanosheet composite [48]). Lead (Pb) based ceramics such as PZT, exhibit high piezoelectric coefficients. However, their rigidity, brittleness, and toxicity limit their applications [49]. Polymers are neither rigid nor brittle. However, they present much weaker piezoelectric properties than other materials which exhibit huge polarization in their crystalline structure. As an example, the  $k_{33}$  coefficients of the PZT-5H ceramic is equal to 0.75 [50], that of the PVDF to 0.22 [51] and that of the single crystal PMN-32PT with (001) orientation to 0.93 [50].

## 2.2. Piezoelectric materials and Piezotronics

In the applications linked to energy harvesting from mechanical vibrations, the direct piezoelectric effect is used [53, 23]. In order to recover energy from vibrations, piezoelectric materials are integrated into host oscillating structures such as cantilevers. The polarized material is placed between two electrodes which are connected by an electrical circuit.

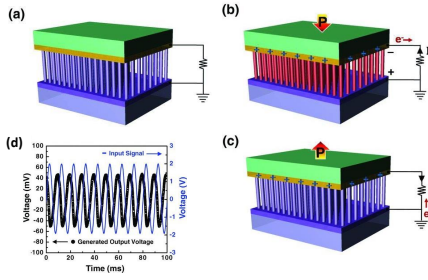


Figure 2: Production of electric current by a piezoelectric. (a) Piezoelectric ZnO nanowire arrays placed between two electrodes coated with Platinum. (b) The pressure wave creates a dipole and the appearance of charge on the electrodes. This leads to a potential difference between the top and the bottom of the polarized sample and thus to an electron flow which balances the charges and equalizes the electric potentials on both sides. (c) the decompression causes the cancellation of the internal dipole and thus the transfer of charges in the opposite direction. A current of opposite direction appears. (d) The input signal for the generation of a sound wave and the output voltage from the piezoelectric ZnO nanowire arrays due to the sound wave. The phase difference between the signals is due to the impedance of the intrinsic capacitance and reactance within the piezoelectric circuit. Figures and captions reproduced from [52] with permission from John Wiley and Sons, copyright 2010.

The mechanical compression induces the appearance of charge on the crystal and a flow of electrons from the electrode in the electric circuit. This flow stops when the electric field created by the distribution of electrons in the electric circuit cancels the electric field created by the compression of the material. At this stage the current is zero. When the compression is released, the electric dipoles of the material are no longer deformed. Thus the barycenter of positive and negative charges coincide again and the charges disappear on the faces of the crystal. The electrons initially displaced in the electric circuit will then return to their initial position. This will lead to an electric current of opposite direction in the circuit. In the situation of piezoelectric materials, there is no transfer of electrons from the piezoelectric material to the external circuit and the system behaves like a simple capacitor. The generated electric signal by the piezoelectric material under mechanical vibrations is thus an alternating capacitive signal. The voltage may have positive and negative minima, as well as areas of zero values (Figure 1). To exploit the harvested energy, a rectifier bridge is required to convert the alternative signals into direct ones.

Wang et al. [54] introduced a new field coined

piezotronics [55, 56]. This field is based on piezoelectric materials that display semiconductor properties. In those situations, electrical charges can be transferred from the material to the electrode. We will start with the situation where such a material is placed between two platinum electrodes. This situation is illustrated in the Figure 2 where a ZnO-based device is used under a sound wave. At the level of the electrodes, the ZnO-Pt contacts are Schottky diodes. In the compressive mode, whatever the phase of the displacement, one of the two diodes is polarized in the wrong direction, which prevents the departure of the charges from ZnO. The generated current is capacitive and alternating. There is no transfer of electrons between the electrodes and the material in this situation. The system behavior is close to the one involved in classical piezoelectric materials as a simple capacitor.

The main breakthrough of piezotronics appears when the contacts between the material and the electrodes involve an ohmic contact on one side and a Schottky diode contact on the other. In this situation it is possible to produce a direct current [57, 58]. Wang et al. developed a nanogenerator fabricated with vertically aligned arrays of zinc oxide nanowires (ZnO NWs) placed under a zigzag metal electrode with a small gap. Mechanical vibrations move the electrode up and down to bend and/or vibrate the nanowires. Unlike the previous device, the zinc nanowires are connected with a silver plate at bottom and with a platinum plate on top. It is to mention that the ZnO-silver contact is ohmic, while the ZnO-platinum contact is a Schottky diode.

When the platinum-covered tooth of the electrode deforms the nanowire, the curvature of the piezoelectric material causes a dipole to appear perpendicular to the main direction of the nanowire [54] (Figure 3). In the stretched area, the potential of the nanowire is higher than the potential of the platinum metal. The Schottky diode is reverse biased and no electrons are allowed to pass in the electrical circuit. This phase corresponds to an electron displacement in the nanowire from the stretched area to the compressed area perpendicular to the main direction of the nanowire. When the tooth is placed deeper, the nanowire twists more and the contact is made with the compressed zone. The potential of this zone is lower than the potential of the platinum, the diode allows the current to flow and electrons can circulate in the closed circuit. Their passage tends to make the lateral potential difference disappear which closes the

Schottky diode again. The current from the nanowire decreases and is cancelled. The global measured current is the sum of these milli-currents all oriented in the same direction. The output electricity generated is continuous and stable. The output averaged power density is comprised between 1 and 4  $\text{W.m}^{-3}$  [59].

The output power of piezoelectric and piezotronic devices depends both on intrinsic parameters, including the piezoelectric and mechanical properties of the material and the resonance frequency of the piezoelectric element, and extrinsic factors such as the features of the mechanical vibrations (frequency, amplitude) and the mechanical features of the host structure. This explains why in the literature, the level of power output of piezoelectric energy harvesters varies greatly from  $100 \mu\text{W.cm}^{-3}$ [60] to  $10000 \text{mW.cm}^{-3}$  (KNN/MNC material[61]). In order to fix ideas, we propose in the following a series of outstanding examples which enable the performance comparison between piezoelectric systems and the other energy recovery systems.

Using PZT-5H piezoceramics, Roundy et al. [62] reported an average outpower of  $60 \mu\text{W}$  for a volume of  $1 \text{cm}^3$  and an acceleration of  $2.25 \text{m.s}^{-2}$ . Platt et al. [63] showed that by stacking 145 layers of PZT in a  $2 \text{cm}^3$  volume, they measured an average outpower of  $1.6 \text{mW}$  ( $800 \text{W.m}^{-3}$ ) under a  $900 \text{N}$  load and at a vibration frequency of  $1 \text{Hz}$ . PMN-25-PT single crystal [41] displays an outpower density of  $60 \text{mW.cm}^{-3}$  ( $60000 \text{W.m}^{-3}$ ) for a vibration of an amplitude of  $150 \mu\text{m}$  and a frequency of  $900 \text{hertz}$ . Under the same conditions, a device containing PZT ceramics displays a 20-time-lower power density[64].

PVDF is the most frequently used piezoelectric polymer. Compared with piezoelectric ceramics, PVDF has much lower piezoelectric performances. For comparison, Kendall [65] showed that under  $2 \text{Hz}$  excitation and  $68 \text{kg}$  weight, a PVDF-based sole flexing system provides an output power of  $0.6 \text{mW}$ , while the same device with a PZT-based sole could reach a power output of  $5 \text{mW}$ . Wind energy harvesters using PVDF films were studied as well. their performances does not exceed  $2 \text{mW.cm}^{-3}$  in  $7 \text{m.s}^{-1}$  wind [66]. A way to improve polymer properties is to make thin film stacks. Godard et al. [67] showed that a stack of 10 thin layers of poly(vinylidene fluoride trifluoroethylene) screen printed on a polymer substrate harvests up to  $0.97 \text{mW}$  at  $33 \text{Hz}$  with an area of only  $2.4 \text{cm}^2$ .The structure in  $N$  thin films allows to increase the recovered energy by a factor  $N^2$  compared to the same overall polymer thickness.

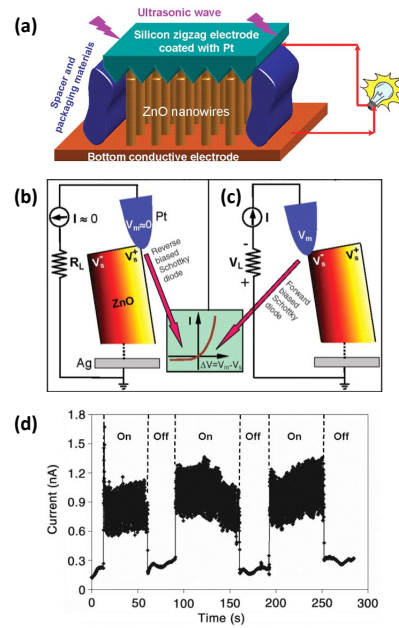


Figure 3: (a) Schematic diagram showing the design and structure of the nanogenerator. Aligned ZnO NWs grown on a solid/polymer substrate are covered by a zigzag electrode. The substrate and the electrode are directly connected to an external load. (b) Contact between the tooth covered with Platinum and the semiconductor ZnO NW showing reverse biased Schottky rectifying behavior. The process in (b) is to separate and maintain the charges as well as build up the potential. (c) Contact between the tooth covered with Platinum and the semiconductor ZnO NW showing reverse forward Schottky rectifying behavior. The process in (c) is to discharge the potential and generates electric current. Figures and captions reproduced from [54] with permission from The American Association for the Advancement of Science, copyright 2006. (d) Measurement of the output current intensity in presence and absence of ultrasound. Figures and captions reproduced from [59] with permission from The American Association for the Advancement of Science, copyright 2007.

Liao et al. [68] developed a fiber-based hybrid nanogenerator consisting of ZnO NWs/carbon fibers and Au-coated ZnO-papers, which can be used in converting mechanical energy into electricity. An output current with a peak value of 35 nA was generated. The desired electrical output is obtained by adjusting the external strain rate and the number of devices connected in parallel or in series. The electrical energy generated by the multi-fiber based NG was stored and used to light up a LED. Qin et al. [69] obtained an instantaneous (not averaged) power density of  $5.1 \text{ mW.cm}^{-2}$  from one ZnO nanogenerator under a pressure of  $0.44 \text{ kg.cm}^{-2}$  and a fixed frequency of 1000 Hertz.

Piezoelectric vibration energy harvesting has also gained significant attention due to its compatibility with Microelectromechanical Systems (MEMS) technology [70].

Park et al [71] introduce a piezoelectric microelectromechanical systems (MEMS) energy harvester that utilizes the  $d_{33}$  piezoelectric mode. To enhance the piezoelectric properties of the sol-gel spin-coated PZT (Lead Zirconate Titanate) thin film, a  $\text{PbTiO}_3$  seed layer was implemented as an interlayer between the  $\text{ZrO}_2$  layer and PZT thin films. The fabricated cantilever PZT film, featuring an interdigital-shaped electrode, exhibited a remnant polarization of  $18.5 \text{ C.cm}^{-2}$ , a coercive field below  $60 \text{ kV.cm}^{-1}$ , a relative dielectric constant of 1125.1, and a  $d_{33}$  piezoelectric constant of  $50 \text{ pC.N}^{-1}$ .

The fabricated energy-harvesting device achieved an electrical power output of 1.1 W when subjected to a vibration with an acceleration of 0.39 g at its resonant frequency of 528 Hz, under a load of  $2.2 \text{ M}\Omega$  with a 4.4 V peak-to-peak voltage. The corresponding power density was calculated as  $7.3 \text{ mW cm}^{-3} \cdot \text{g}^{-2}$  (rescaled by the acceleration 0.39g), or a  $1.1 \text{ mW cm}^{-3}$ . The experimental results were compared with numerical calculations derived from dynamic and analytical modeling equations. Additionally, a comparison was made between the fabricated device and other piezoelectric MEMS energy-harvesting devices.

In summary, this study presents the modeling, fabrication, and characterization of a piezoelectric MEMS energy harvester utilizing the  $d_{33}$  piezoelectric mode. The implementation of a  $\text{PbTiO}_3$  seed layer in the device's structure improved its piezoelectric properties. The fabricated device demonstrated significant power generation capabilities, as validated by experimental and numerical comparisons with other

similar energy-harvesting devices.

It involves using cantilever beams with one or two piezoelectric layers and an elastic layer to convert mechanical vibrations into electrical energy. The configuration with two piezoelectric layers, known as a bimorph, has the potential to generate larger electric power. However, as the size of the cantilever-type vibration-energy harvester (VEH) decreases, it becomes more challenging to lower the resonance frequency and achieve sufficient electric power for sensor node batteries.

To address this issue, Tsukamoto et al [72] display a bimorph VEH with a flexible 3D mesh structure. The purpose of this structure is to control the bending stiffness, thereby simultaneously lowering the resonance frequency and increasing the electric power output. The device consists of two PVDF (Polyvinylidene fluoride) piezoelectric layers bonded on both sides of a 3D mesh elastic layer, with a proof mass attached at the tip. The sum of the line spacing and line length in the mesh is  $100 \mu\text{m}$ .

The study confirms the effectiveness of the bimorph VEH with a 3D mesh structure as an elastic layer through various experiments. Firstly, they demonstrate that the bending stiffness of the mesh harvester can be controlled by adjusting the line spacing in the mesh. Secondly, in vibration tests, it is observed that the resonance frequency of the mesh harvester is lowered by 26% compared to a flat-plate VEH, and the tip deflection is 1.3 times larger. Finally, the total output power of the device is measured to be  $20.4 \mu\text{W}$ , which is sufficient to power low-consumption sensor nodes for Wireless Sensor Networks (WSNs).

All these figures are difficult to compare. Some powers are instantaneous and others are averaged, which is radically different because of the particular shape of the electrical signal. Moreover, they are obtained under different conditions of solicitation. These works do not present a energy conversion ratio which compares the recovered energy with the energy injected into the system. Only a few authors indicate the energy conversion rates in their work. For example, self poled PVDF- $\text{WS}_2$  composite displays a record energy conversion of 25.6% for piezoelectric nanocomposites[73]. This value is closed to the one obtained by Chang et al.[64] (25%) for thin films of PVDF fibers. It is higher than the one reported for PVDF-DNA films (2.7%) [74], for PVDF/ $\text{AlO-rGO}$  (aluminum oxides decorated reduced graphene oxide incorporated PVDF based nanocomposite) Flexible Nanocomposite (12%)[75] and PZT nanocrystals

(5%)[42].

All these features show that piezoelectric and piezotronic nanogenerators are among the most efficient nanogenerators [76]. These devices are unaffected by temperature and humidity [77] and can produce alternating current in a range from  $\mu\text{W}$  (microwatts) to  $\text{mW}$  (milliwatts)[78]. These nanogenerators require limited moving parts, zero external voltage sources and are of low cost [79]. They can generate power output with voltage levels that can be easily conditioned (i.e., converted to DC)[80] and sufficient for sensor powering demand. In the last decades, many achievements have been made[81]. We resume some significant examples in the section below.

### 2.3. Sensors powered by piezoelectricity

In the last decade, many self-powered sensors based on piezoelectric nanogenerators have been developed[82]. It is possible to separate the achievements made in three categories: devices that use the electrical signal created by vibrations to probe their environment (Simple Autonomous Sensor) [83], devices that store electrical energy and then restore it to connected objects (Sensor powered by a Nanogenerator With Storage System), and devices that directly power connected objects (Sensor powered by a nanogenerator without storage system). In the following we will discuss these three categories.

#### 2.3.1. Simple Autonomous Sensor

Deng et al. [84] designed a self-powered flexible piezoelectric sensor (PES) based on cowpea structured PVDF/ZnO nanofibers (CPZN) for remote gesture control in a human-machine interactive system. The sensor exhibits excellent bending sensitivity of  $4.4 \text{ mV deg}^{-1}$  in a range of  $44^\circ$  to  $122^\circ$  and a fast response time of 76 ms. It does not need to be powered. They incorporated this sensor in a chain of devices allowing the remote control of a robotic hand. While the human hand performs movements, these movements are detected and captured by the piezoelectric sensor. The electrical signal is then transferred, analyzed, and transformed into commands that guide the movement of the robotic palm.

In the field of smart sports and high performance sports training, Tian et al. [85] designed a self-powered, lamellar crystal-rich, baklava-structured PZT/PVDF piezoelectric sensor. This sensor has a high sensitivity ( $6.38 \text{ mV/N}$ ) along with a short response time of 21 ms. They used this composite to

fabricate a ping pong racket which integrates 36 different sensors distributed on the racket. During training, it is possible to see the force of the impact and the centering of the ball on the racket.

Piezoelectric biosensors/bioactuators [86] are developed with new materials and advanced encapsulation methods to avoid the toxicity of conventional lead-based piezoelectric materials. These materials such as poly(lactic acid) polymer (PLLA) can be used in the human body for biomedical pressure sensing applications. Curry et al. have implanted a PLLA piezosensor inside the abdominal cavity of a mouse to monitor the pressure of diaphragmatic contraction [87]. Liu et al. [88] developed a PVDF piezoelectric sensor for respiration sensing and healthcare monitoring.

#### 2.3.2. Sensors powered by a Nanogenerator With Storage System

In 2011, Hu et al. [89] presented one of the first self-powered connected objects. For this they covered a cantilever equipped with electrodes of polymer substrate and textured ZnO films. Subjected to vibrations which induce a deformation of 0.12% at a deformation rate of  $3.56 \% \text{ s}^{-1}$ , the  $1 \text{ cm}^2$  device produces a power of  $6 \mu\text{W}$  (see Figure 4). This power is not enough to power a connected object and requires a storage system consisting of a rectification circuit and a capacitor (Type 1210,  $22 \mu\text{F} \pm 10\%$ , AVX). This system powers a sensor and a radio frequency data transmitter. Thanks to this storage system, they were able to autonomously transmit wireless signals at distances of 5-10 m.

Godard [67] et al. used a stack of 10 thin layers of poly(vinylidene fluoride trifluoro-ethylene) connected to a rectifier circuit and a voltage regulator (LTC3588-1, Linear Technology) to power a microcontroller (Arduino Pro Mini) connected to a radiofrequency (RF) emitter (RN-42 Blue-tooth module from Microchip). Temperature values recorded by the microcontroller internal temperature sensor were successfully transmitted via RF signal to a mobile phone for 10 s (see Figure 4).

#### 2.3.3. Sensors powered by a Nanogenerator Without Storage System

This approach is more difficult. Despite the realization of many piezoelectric nanogenerators that can produce powers of a few  $\text{mW}$ , it is difficult to find complete devices integrating a nanogenerator and a commercial Internet of Things (IoT) sensor in the

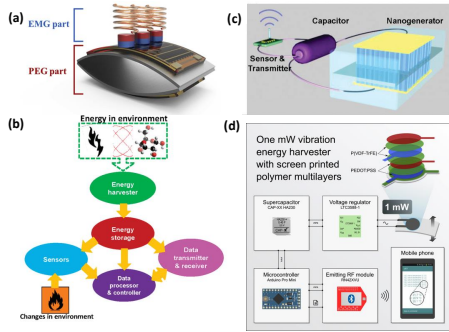


Figure 4: (a) Schematic image and pictures of the hybrid energy harvester based on PEG and EMG [90]. Figures and captions adapted from [90] with permission from Elsevier, copyright 2020. (b) Schematic diagram of the integrated self-powered system. An integrated system can be divided into five modules: energy harvester, energy storage, sensors, data processor and controller, and data transmitter and receiver. (c) The prototype of an integrated self-powered system by using a nanogenerator as the energy harvester [89]. Figures and captions adapted from [89] with permission from American Chemical Society, copyright 2011. (d) Godard et al. show that 2.4 cm<sup>2</sup> of screen-printed multilayers of a piezoelectric polymer, P(VDF-TrFE), can harvest up to 1 mW at 33 Hz. They demonstrate that this is sufficient for an autonomous sensor to communicate with a mobile phone independently of any other energy source [67]. Figures and captions adapted from [67] with permission from Elsevier, copyright 2020.

litterature. The main reason is that direct plugging requires power of at least 5 mW, which remains a complex aim to reach [90].

Jung et al. [90] succeeded in producing an average output power of 25.45 mW at 60 Hz and 0.5 G input vibration by coupling a piezoelectric nanogenerator made of macro-fiber composite (MFC) piezoelectric plates on the substrates and an electromagnetic nanogenerator. The optimization of the coupling requires an electrical impedance matching and the minimization of the mechanical damping (see Figure 4). They managed to use this device for direct power supply of a commercial IoT sensor (CC2650 Bluetooth SensorTag, Texas Instruments Corp) without the use of storage system.

Hwang et al. [91] used a new generation of single crystal  $(1-x)\text{Pb}(\text{Mg}_{1/3}\text{Nb}_{2/3})\text{O}_3 - x\text{PbTiO}_3$  (PMN-PT) to prepare a piezoelectric nanogenerator. This material exhibits an exceptional piezoelectric charge constant of  $d_{33}$  up to 2500 pC.N<sup>-1</sup>, which is almost 4 times higher than PZT, 20 times higher than BaTiO<sub>3</sub> and 90 times higher than ZnO. Using this material, they achieved a self-powered artificial pacemaker with

significantly increased electrical output current. No battery is needed to store the recovered energy.

#### 2.4. Summary and Outlooks for piezoelectric materials

The previous results show that the piezoelectric nanogenerators reported in the literature are capable of powering sensors. This allows us to be very optimistic for their deployment for IoT objects, especially in the field of building monitoring[76]. Wireless sensor networks have become an essential part of building environment monitoring, covering multiple functionalities including temperature, light usage, object movement, humidity, air velocity in a ventilation duct and etc. The real-time monitoring of these parameters enables an intelligent regulation and control of the building environment with reduced energy demand. All these sensors require an electrical power between 0.5 and 100  $\mu\text{W}$ .

It is possible to recover energy from environmental sources, such as air flows in ventilation systems or the movement of people on the floor. To provide a quantitative point of view, the reported powers range from 37.4 to 800 microWatt in ventilation systems and from 66 microwatt to 55 mW for floors [76]. Even if it remains complex to remove the energy storage system from the module, these piezoelectricity based systems could significantly extend the classical battery systems and decrease the energy cost of the IoT. Piezoelectricity based technologies have already been applied by several companies around the world, as in the case of Kinergizer and EnOcean [92].

Despite the great progress in piezoelectricity-based systems, there are still technological challenges which require extensive research works before the manufacture of matured autonomous IoT devices. The key issue consists in the output power and the need for intermediate energy storage. Future research works should dedicate more attention to the management and modelization of energy generation and storage exchange, the integration of bio-source materials and the technology cost reduction[7].

### 3. Mechanical vibration energy harvesting using electrostrictive materials for sensor powering

#### 3.1. Electrostriction

Electrostriction is a mechanism that all materials possess. When subjected to an electric field  $E$ , materials deform. Their deformation  $S$  is proportional to

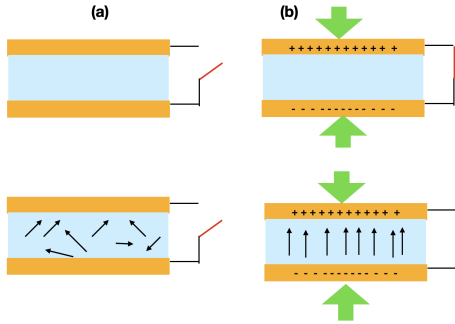


Figure 5: Electrostriction origin. (a) Maxwell stress that originates from the Coulomb interaction between oppositely charged compliant electrodes. (b) Intrinsic electrostatic effect that originates from direct coupling between the polarization and the mechanical response.

the square of the electric field  $E$  and therefore does not depend on the direction of the field.

The microscopic origin of this phenomenon comes from two phenomena (see Figure 5). First, when a material is placed in an electric field, the charges of this material move with respect to their initial position. This results in the appearance of a net charge on the surfaces of the material, the charge on the upper surface balancing the charge on the lower surface. The action of the field compresses the material. This mechanism is at the origin of the breakdown voltage of capacitors containing soft polymer dielectrics. The deformation is given by  $S = -E^2 \frac{\epsilon_0 \epsilon_r}{2Y}$  where  $Y$  is the young modulus of the material,  $\epsilon_0$  the vacuum permittivity and  $\epsilon_r$  the dielectric constant of the material.

Second, some polymers exhibit intrinsic electrostriction properties resulting from the change in their dielectric constant under the effect of the electric field. The electrical field modifies the relative position of the electric dipoles of the material. In this situation and for an uniaxial compression, the deformation  $S$  is given by  $S = \frac{a_1 + a_2(1-\nu)}{\epsilon_r} E^2$  where  $\nu$  is the Poisson coefficient,  $a_1$  and  $a_2$  parameters describing the evolution of the dielectric constant as a function of the deformation.

These two deformations add up to describe the global response of the material[93].  $S = M_{33} E^2 = \left( \frac{a_1 + a_2(1-\nu)}{\epsilon_r} - \frac{\epsilon_0 \epsilon_r}{2Y} \right) E^2$ . The coefficient  $M_{33}$  is the electrostriction coefficient under an uniaxial compression along the electrical field direction. We report here measured  $M_{33}$  values. We will see in the following paragraph that it is necessary to de-

fine a figure of merit to compare the different materials between them and that only this coefficient is not suitable to qualify the performances. Muenst et al. [94] studied electrostrictive properties of polyaniline(PANI)/polyurethane(PU) composites at low fillers concentration. The intrinsic electrostriction modulus ( $M_{33} = -6.10^{-16} \text{ m}^2 \cdot \text{V}^{-2}$ ) increases by a factor of 1.6 compared to pure PU. Yin et al.[95] investigated carbon black/P(VDF-TrFE-CFE) composites fabricated via a simple blending method. The composite displays an increase of the electrostriction modulus  $M_{33} = -2.4.10^{-16} \text{ m}^2 \cdot \text{V}^{-2}$  by a factor 2 compared to the polymer. A huge electrostriction modulus ( $M_{33} = -2.4.10^{-14} \text{ m}^2 \cdot \text{V}^{-2}$ ) was reported by Yuan et al. [96] studying reduced graphene oxide/composite.

### 3.2. Electrostrictive material

In order to recover energy from vibrations, electrostrictive materials based variable capacitors are integrated into a host oscillating structure. Unlike piezoelectric or triboelectric materials, electrostrictive materials requires excitation from external voltage sources to be activated. A capacitor consists of two electrodes separated by a dielectric material. The capacitance of the capacitor is given for a flat capacitor by  $C = \frac{Q}{U} = \frac{A}{\epsilon_0 \epsilon_r d}$  where  $Q$  is the charge stored by the capacitor and  $U$  the potential difference across the capacitor,  $d$  the distance between the two electrodes,  $\epsilon_0$  the vacuum permittivity, and  $\epsilon_r$  the dielectric constant of the material. A variable capacitor is defined as a capacitor whose capacity varies according to the mechanical vibrations. An example would be the capacitance variation caused by the distance variation between two electrodes in a capacitor.

By applying a variable capacitor, it is possible to design an energy conversion process from mechanical energy towards electrical energy. When the capacitor is polarized by a voltage  $U$ , it acquires a charge  $Q_1 = C_1 U$  and an energy  $E = \frac{U^2}{2C_1}$ . Considering the situation where the vibration initially moves the electrodes away from each other, the capacitance of the capacitor decreases and reaches a value of  $C_2$ . This induces at fixed  $U$  a displacement of electron in the electric circuit which connects the two electrodes so as to decrease the charge  $Q_1$  carried by the electrodes to  $Q_2 = C_2 U$ . When the two plates come together again, an electron displacement in the opposite direction occurs to increase the charge again and make it correspond to the value  $Q_1$ . The energy converted in a cycle in absence of losses with fixed  $U$  is equal

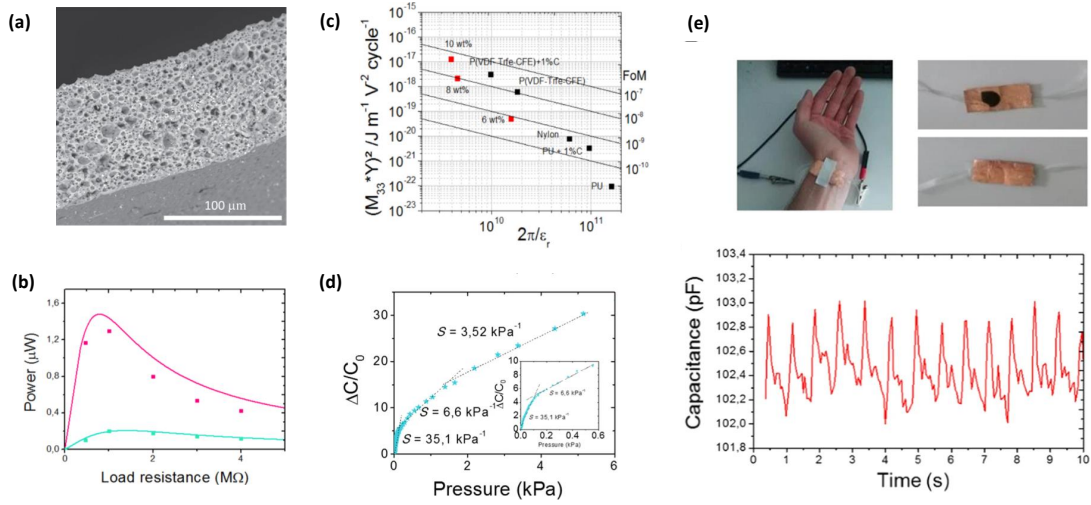


Figure 6: Illustration of two possible applications of an electrostrictive porous carbon black composite : energy harvester or capacitive sensor (a) Electron microscope picture of a cross-cut of a porous carbon black composite.(b) Energy harvester: Harvested power of the composites with 8 CB wt% (green) and 10 CB wt% (pink) with insulating layer as a function of the load resistance. Squares are experimental data and lines are theoretical predictions using equation. The strain frequency is 100 Hz and the applied voltage over the composite  $V_{dc}=32V$ .(c) Energy harvester: Comparison of the electromechanical performances at 100 Hz using the figure of merit (FoM) proposed by Guyomar et al [97, 98, 99] Thick lines have the same FoM. Black spots refer to materials from the literature [97, 98, 99]. Figures and captions reproduced from [100] with permission from Institute of Physics Publishing Ltd., copyright 2018. (d) Capacitive sensor: Sensitivity measurements  $S$  after 100 cycles for three different pressure ranges (10 wt % CB).(e) Arterial signals measured with the sensor. Figures and captions reproduced from [101, 100] with permission from Springer Nature, copyright 2019.

to  $E = \frac{1}{2}U^2(C_1 - C_2)$ . By analyzing the electrical response of an electrostrictive material subjected to vibration, Lallart et al. [99, 28] show that the maximum recoverable power is given by:

$$P_{max} = \frac{2\pi}{\epsilon} (M_{33}Y)^2 A l E_{dc}^2 f S_M^2 \quad (3)$$

where  $A$  is the surface of the material,  $l$  its thickness,  $f$  the vibration frequency,  $S_M$  the strain magnitude,  $E_{dc}$  the applied electrical field,  $\epsilon_r$  the value of the dielectric constant,  $M_{33}$  the electrostriction coefficient under an uniaxial compression along the electrical field direction,  $Y$  the young modulus of the material under compression. They define a Figure of merit (FOM)  $F$  dependent only upon the properties of the electrostrictive material equal to:  $P_{max} = F A l E_{dc}^2 f S_M^2$  with  $F = \frac{2\pi}{\epsilon} (M_{33}Y)^2$ .

Figure 6(c) displays the FOM  $F$  of materials from the literature. Polyurethane displays lower performances than Nylon. PVDF is most suited polymer for these applications. The FOM values are enhanced when polymers are loaded with conductive particles. PVDF loaded with carbon nanotubes has a higher figure of merit than pure PVDF. PDMS-carbon black particles composite [100] exhibit the highest figure of merit ( $F=7 \cdot 10^{-8}$ ,  $M_{33}= 8.46 \cdot 10^{-15} \text{ m}^2\text{V}^{-2}$ ). The excellent properties of composites are due to two reasons [100, 28]. First, composite materials exhibit a large increase of dielectric permittivity in the vicinity of the percolation threshold. Second, the structure of a network of particles close to percolation can also be used to create intrinsic electrostrictive properties. Indeed, when a material close to percolation is strained, a local variation of filler concentration can be induced. Consequently, a variation of dielectric permittivity is observed. To be effective, this concentration variation must not be too important and lead to the creation of a percolation path in the sample which would make the latter an electrical conductor.

As explained previously, electrostrictive materials are materials that must be subjected to a voltage to be active. If these materials are conductive, ohmic losses occur. The loss magnitude is characterized by a loss factor  $\frac{\sigma\omega}{\epsilon_0\epsilon_r}$  where  $\sigma$  is the net conductivity, and  $\omega$  the electric pulsation. It is to mention that the losses are not taken into consideration in the calculation of FOM. In order to limit these losses, it is possible to add a thin insulation layer to the surface of the composites. Pruvost et al. [100, 102] show that this allows to decrease the loss factor by a factor of 10 while maintaining the electrostrictive properties of the material.

### 3.3. Energy harvested by electrostrictive systems

Electrostrictive materials used in variable capacitors can target applications ranging from small to very large scales, which is not the case for piezoelectric materials. We recall that the frequency at resonance varies as  $1/(\sqrt{m})$  where  $m$  is the mass of the system. Small frequencies are therefore accessible to large devices.

In this context, applications to wave energy recovery have been proposed. Bosch Company[103] makes a demonstrator model to convert wave energy into electricity with a disruptive design. A float is positioned on the surface of the ocean and is firmly anchored at the bottom of the ocean. The two halves are connected with a thousand sheets of dielectric polymers. Every 3 to 10 seconds, these sheets are deformed by the movement of the waves and allow current to be generated. Moretti [104] et al. demonstrated the ability of a dielectric elastomer to convert the oscillating energy carried by water waves into electricity. They build a harvester prototype using a commercial polyacrylate film as electrostrictive polymer. In resonant conditions, their system demonstrates a delivery power per unit mass of  $197 \text{ W.kg}^{-1}$ .

At microscale, electrostrictive polymers can be used as an electroactive composite based on reduced graphite oxide sheets in a PDMS matrix. Applying a sinusoidal acceleration (0.5 g, 15 Hz), Nesser et al. [105] succeed in harvesting a power density of  $6 \mu\text{W.cm}^{-3}$  under a static electrical field of  $0.4 \text{ V.}\mu\text{m}^{-1}$ . Cottinet et al. [98] measured a  $280 \mu\text{W.cm}^{-3}$  power density using a P(VDF-TrFE-CFE) polymer for a transverse strain of 0.2% with a static electric field of  $10 \text{ V.}\mu\text{m}^{-1}$  at 100 Hz.

In the two previous studies, the ohmic losses are not evaluated. These are probably very low in the case of polymers but can be very important in the case of composites including conductive particles. In order to limit the electrical conduction of systems that have structures close to percolation, Pruvost et al. [100, 102] used PDMS foams. During the synthesis the conductive particles are localized in the drops of an inverse emulsion of PDMS. After drying and cross-linking of the continuous medium and for moderate water fractions, the particles are trapped in the unconnected bubbles. This structure prevents the creation of connected paths. By introducing these foams in a cantilever structure and by using a thin insulating layer, they measure a  $1 \mu\text{W.cm}^{-2}$  ( $75 \mu\text{W.cm}^{-3}$ ) under a voltage of 200 V (thickness of the layer  $125 \mu\text{m}$  i.e  $E=1.6 \text{ V.}\mu\text{m}^{-1}$ ) and an acceleration

of 7 g. For this material the losses correspond to 1 % of the harvested power.

From the data reported by Pruvost et al. [102], the conversion rate of the injected mechanical power can be calculated. In this device, the variation of the capacitance comes not only from the electrostrictive properties of the material but also from the creation of a very low capacitance when the electrodes of the capacitor are detached and separated by the vacuum. The energy supplied to the system is the kinetic energy of the upper part, and can be calculated from the mass of the upper electrode ( $m=3g$ ) the relative displacement speed of the two electrodes ( $v=e \times f=1 \times 10^{-3} \times 40=0.04 \text{ m.s}^{-1}$ ) where  $f$  is the oscillation frequency and  $e$  the size of the air gap. The kinetic power is equal to  $96 \mu W$  and the recovered power  $7.5 \mu W$  leading to a conversion factor of 8 %. This is lower than the performances reported by Lallart et al. who measured a conversion factor of 34 % for P(VDF-TrFE-CTFE) composite with bis (2-ethylhexyl) phthalate [95]. In this situation, an electrical power density of  $4.31 \text{ mW.cm}^{-3}$  was achieved for the modified terpolymer working at a DC bias electric field of  $30 \text{ MV.m}^{-1}$ .

### 3.4. Sensors powered by electrostrictive materials

As presented above, there are three ways to power sensors using the energy around us: autonomous sensors, sensors powered by a nanogenerator with storage system, sensors powered by a nanogenerator without a storage system. In the following paragraph we discuss these applications.

#### 3.4.1. Electrostrictive autonomous sensors

Electrostrictive materials have been widely used to fabricate capacitive sensors, whose working principle is mainly based on the variation of capacitance. They are usually composed of two stretchable electrodes between which is placed an elastomer dielectric film to form a well-known parallel plate capacitor. Such sensors allow in particular the local measurement of pressure or temperature and are excessively low energy consumers compared with resistive sensors.

The sensitivity to pressure  $SP$  is given by  $P = \frac{\Delta C}{\sigma C_0} = \frac{\Delta C}{\epsilon Y C_0}$  where  $C_0$  is the initial capacitance,  $\Delta C$  the variation of the capacitance,  $\sigma$  the shear stress,  $\epsilon$  the strain, and  $Y$  the young modulus. So to get a high sensitivity, low young modulus are required. Dielectric polymers with a low young modulus as PDMS are traditionally used. In this context, the capacitive sensitivity of a pyramid-structured PDMS film was

investigated by Bao [106]. A sensitivity of  $0.55 \text{ kPa}^{-1}$  was reported compared to  $0.02 \text{ kPa}^{-1}$  for an unstructured film (see Figure 7). Structured PDMS has a high permittivity variation. Indeed, the air pockets are gradually and reversibly replaced by polymer during the deformation process. This leads to a variation of the dielectric constant by a factor of 2 or 3.

To increase the sensitivity of such devices without using additional energy, Pruvost et al. [100, 101] have proposed to use PDMS foams whose bubbles are lined with conductive particles. Due to the elastic behavior of the foam pores, a sensitivity ten times higher than previously reported is measured. The sensitivity exceeds  $35 \text{ kPa}^{-1}$  for a pressure lower than  $0.2 \text{ kPa}$  (see Figure 6(d) and (e)). These materials are inexpensive, easy to prepare, and have high capacitance values that are easy to measure using inexpensive electronic devices. These materials are part of the development of electronic skin systems [107]. Liu et al. [108] used an electrostrictive polymer to detect compressive force. This sensor consists of a series of elements made of DE membrane with out-of-plane deformation. Each element experiences highly inhomogeneous large deformation to obtain high sensitivity. The sensitivities of the sensor element are about  $105 \text{ pF.N}^{-1}$ . Capacitive sensors [109] are designed to monitor the pressure exerted on a chair by a person, the pressure distribution on a shoe, and the pressure exerted by a knee prosthesis on an amputee who could be seriously affected by an arising decubitus [110, 111].

These sensors can also be used for human machine interfaces. It is possible to synchronize the current intensity with the pressure intensity received in the sensor, so as to modulate the LED lighting [112]. This kind of device can be integrated into a car steering wheel for the purpose of illumination or temperature control [112]. (see Figure 7). Unlike conventional robots [113], soft robots can operate freely in our environment because they cause less damage in case of impact. Dielectric soft sensors are the sensors of choice that can be integrated into soft robots. They can measure pressure but also deformation and shear. The challenge is to use many sensors in parallel.

### 3.5. Sensors powered by a nanogenerator without storage system

Hyper Drive Corp has created a small electric power generator utilizing an electrostrictive polymer, which has a mass of around 1 g and a diameter of 8 cm. When the device central part is pushed by

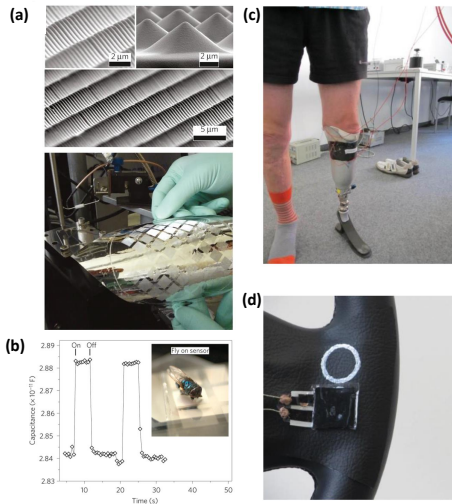


Figure 7: (a) SEM images of the microstructured PDMS films. The pressure-sensitive structured PDMS films can be moulded at full-wafer scale (100 mm) with high uniformity and fidelity on a variety of flexible, plastic substrates. (b) The microstructured PDMS films are able to sense the application of very small pressures. Shown is the capacitance change on placing and removing a bluebottle fly (20 mg) on an area of 64 mm<sup>2</sup>, corresponding to a pressure of only 3 Pa [106]. Figures and caption from [106] with permission from Springer Nature, copyright 2010. (c) Electrostrictive pressure sensor attached on the liner of a knee prosthesis for an experimental evaluation [111]. (d) Control interface with electrostrictive pressure sensors integrated into an automotive steering wheel [112]. Figures and caption from [111, 112] with permission from Society of Photo-Optical Instrumentation Engineers (SPIE), copyright 2016 and copyright 2017.

4-5 mm once every second, it generates roughly 0.12 W of power [114]. This amount of energy can power various LEDs, and through coupling with a wireless system, it can turn remote devices on and off. The generator only supplies electricity to the devices when it receives mechanical energy, making it an effective switching system. Its uncomplicated design makes it simple to integrate into a wireless network. Electrostrictive generators [115] attached to the soles of shoes can produce electric power through deformation caused by walking. Adult men, in experimental settings, were able to generate 0.8-1 watt of power by walking at a pace of one step per second.

### 3.6. Summary and Outlooks for electrostrictive materials

As shown in the previous paragraph, electrostrictive materials, particularly polymeric materials, have very important applications as autonomous sensors. Unlike piezoelectric ceramics, electrostrictive polymer materials are cheap and soft. They are therefore perfectly suited for developing commercial sensor applications. The company StretchSense established in 2015 developed a custom-made electrostrictive-material-based pressure sensors and shear sensors [27]. In the case of medium size devices the results obtained are better than the results of piezoelectric materials. It seems to us that there are prospects in this axis, especially in the recovery of energy from human movements. The powers generated by these electrostatic devices are of one or two orders of magnitude higher than the one obtained with piezoelectric materials. 0.8 W are reported for a shoe equipped with an electrostrictive polymer generator [115] where as 5 mW are reported for a shoe equipped with a piezoelectric ceramic generator [65].

## 4. Mechanical vibration energy harvesting using electrets for sensor powering

### 4.1. Electrets

Electrets are dielectrics able to keep an electric field for years thanks to charge trapping [116, 117]. They are equivalent in electrostatics to magnets in magnetostatics. Trapped "electric charge" can take many forms. It may be excess charge on the surface or in the bulk of the material, but it may also be polarizations in the bulk (fixed aligned dipoles for polar dielectrics, or space charges for polar and non-polar dielectrics), or a composition of both [118]. Electrets are obtained by implanting electric charges

into dielectrics. Theoretically, dielectrics do not conduct electricity; therefore, the implanted charges stay trapped inside. Electret research began in earnest when Mototaro Eguchi [119] prepared one of the first electrets by cooling down a molten mixture of Carnauba wax and resin with a little beeswax, while applying an electric field of around 10 kV/cm to the mixture. Currently, many techniques exist to manufacture electrets [120]: thermal charging by heating up and cooling down in a constant electric field [119], tribo-charging by contact or friction on metallic or dielectric objects, corona-charging, electron or ion injections, liquid contact charging, photo-charging and radiation charging. Triboelectric contact is not covered in this section. In view of the literature generated in recent years on this subject and the advances made in this field, a special section is devoted to triboelectric nanogenerators (TENG) and follows this section. [119].

Corona-charging is the most used technique. It consists of a point-grid-plane structure whose point is subjected to a strong electric field: this leads to the creation of a plasma, made of ions. These ions are projected onto the surface of the sample to charge, and transfer their charges to its surface. The key to all these steps is to find materials that will keep the load they carry over time. Dielectrics are not perfect insulators and implanted charges can move inside the material or can be compensated by other charges or environmental conditions, and finally disappear. A focal area of research on electrets concerns their stability [121, 122, 123]. Nowadays, many materials are known as good electrets, able to keep their charges for years: for example, PTFE (which is one of the best insulating polymers with low conductivity of  $10^{-22} \Omega^{-1} \text{cm}^{-1}$ ) and silicon dioxide ( $\text{SiO}_2$ ) whose stability is estimated at more than 100 years [124, 125]. As an electret, Teflon can contain charge densities of  $5 \cdot 10^{-4} \text{ C/m}^2$  [126].

The key issue in studying electret materials is to know how the charge distribution in an electret influence the electric field around it. The drop of electrical potential  $V_e$  across the electret is linked to the volume charge distribution  $\rho_e(x)$  by  $V_e = \frac{1}{\epsilon_0 \epsilon_e} \int_0^{e_e} \rho_e(x) dx$  where  $e_e$  is the thickness of the electret,  $\epsilon_0$  the vacuum permittivity,  $\epsilon_e$  the relative permittivity of the electret. To make a generator from an electret, it must be placed between two electrodes. By compensation, charges will appear on the electrodes. Gauss's theorem implies that the charge carried by the electret is equal and of opposite sign to the sum of those carried

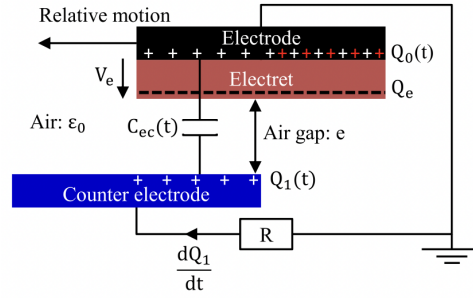


Figure 8: Electret-based converter with a simple load R. Figure reproduced from [127] with permission from IOP Publishing, Ltd, copyright 2016.

by the electrodes ( $Q_o(t) + Q_1(t) + Q_e = 0$  on figure8). The relative movement between the electret and the electrodes will induce a permanent reorganization of the charges between the two electrodes. An electric current will flow through the charge resistance R connecting them (see Figure 8). Its intensity is given by the Kirchoff's law and writes :  $I(t) + \frac{Q_1(t)}{RC_{ec}(t)} = -\frac{V_e}{R}$  where  $I(t) = \frac{dQ_1(t)}{dt}$  and  $C_{ec}(t)$  is the capacitance between the two electrodes. The average power  $P_r$  harvested by the resistor R (during a period of time T) is given by  $P_r = \frac{1}{T} \int_0^T R \left( \frac{dQ_1}{dt} \right)^2 dt$ . The output power is exactly proportional to the frequency f of the periodic displacement and to the electret's surface voltage squared ( $V_e^2$ ) [127, 128].

#### 4.2. Electrets Nanogenerators

There are two typical devices for generating electricity from electrets: rotating devices and conventional variable-capacity devices. From a historical point of view, rotating devices were first introduced.

Jefimenko et al [129] have developed a rotating electret generator consisting of two electrets of different charge placed between two pairs of conductive half-discs. Two electrodes are created by connecting each half-disc of one pair to a half-disc of the other pair. In this generator, charge transfer is due to the variation in charge displacement induced on the two pairs of electrodes during rotation of the two oppositely charged electret discs. Walker's initial generator is a large one. Its diameter is 152.4 mm. It produces a power of 0.025 W at a rotation speed of 6000 rpm and a load resistance of 10 M $\Omega$ . This generator has a high internal impedance, which facilitates energy storage and provides an important potential difference. An electret generator with a radius of 45

mm was developed by Tada [130]. Maximum reported power output from an electret generator was 1.02mW. Tai et al miniaturized this set up [131]. Their prototype generates 25  $\mu\text{W}$  with an electret of radius 4 mm, thickness of 9  $\mu\text{m}$ , effective charge density of  $-2.8 \cdot 10^4 \text{ C.m}^{-2}$  and rotational speed of 4170 rpm.

Currently, the most common and simple structure used is those of a variable capacitor. In some devices, the electrodes are fixed and the electret is moved between them. In other devices, the electret can be attached to one electrode and move vertically or horizontally in relation to another. By laterally moving an electret attached to one electrode relative to another, Arakawa and al [132] obtain a power of 6  $\mu\text{W}$  for an oscillation of 1 mm amplitude at 10 Hz. The surface of the electret is 9  $\text{cm}^2$ , the thickness of the electret is 20  $\mu\text{m}$ . The electret was made by using a fluorocarbon polymer CYTOP.

By using a different type of sliding geometry (the two electrodes are placed on the stator and the electret moves laterally in relation to it), Lo and al [133] obtain a power of 17.98  $\mu\text{W}$  at 50 Hz with an external load of 80  $\text{M}\Omega$ . For low frequencies, the generator can harvest 7.7  $\mu\text{W}$  at 10 Hz and 8.23  $\mu\text{W}$  at 20 Hz. The electret was made with a charged parylene HTR thin-film polymer. The surface charge of the film after corona charge implantation is as high as 3.69  $\text{C.m}^{-2}$ . The size of the device was 9  $\text{cm}^2$ .

An electret energy harvester was developed by J. Nakano, K. Komori, Y. Hattori, and Y. Suzuki [134] to capture the kinetic energy generated by human motion. The electret layer in this device is composed of a fluorinated polymer known as CYTOP EGG. The rotor of the energy harvester features fan-shaped electret and guard electrodes, while the stator has interdigital electrodes to collect the induced charges. The rotor and stator are connected through a miniature ball bearing, allowing free rotation around the center. The assumed parameters for the device include a rotational speed of 1 Hz, an outer radius of the rotor measuring 20 mm, an innermost diameter of the electrodes measuring 9 mm, an air gap of 100  $\mu\text{m}$  between the top and bottom substrates, and a surface charge density of 1  $\text{mC.m}^{-2}$ . The early prototype achieved a power output of up to 3.6  $\mu\text{W}$  at a rotation rate of 1 revolution per second (rps).

Mahanty et al developed [135] a flexible sponge-like nanogenerator based on ZnO nanoparticles and etched porous electret poly (vinylidene fluoride-hexafluoropropylene) (P(VDF-HFP)) film .

This electret possesses improved dielectric and ferroelectric properties than neat P(VDF-HFP) film. The system has a significant remnant polarization  $P_r = 1.9 \mu\text{C.cm}^{-2}$  (i.e., aligned dipoles). It does not require pooling or Corona charging. The authors harvest a power density of 1.21  $\text{mW.cm}^{-2}$  and energy conversion efficiency of 0.3%.

The power densities recovered are of the order of 1  $\text{mW.cm}^{-2}$  i.e. 10  $\text{W.m}^{-2}$ . As we shall see later, they are slightly higher than that recovered by triboelectric materials.

Microelectromechanical systems (MEMS) is the most suitable technology to realize IoT-sensing nodes because it enables integrated fabrication of sensors-actuators, electronic circuits for information processing and radio frequency communication, antennas, and energy harvesters on a single chip or in a package [70].

Honma et al. [136] developed an electrostatic induction-type MEMS energy harvesters. For this purpose they use silicon micromachined comb-electrode oscillators. The fixed electrodes are covered by an electret. Their surface is coated with a negatively charged silicon oxide. The charges are bound with the positive charge at the silicon oxide/silicon interface at the rest position. When the movable electrode (which has not been covered by a silicon oxide coating and which does not bear negative charges) is inserted into the fixed ones, the electrical flux between the negative and positive charges are rearranged in part, and the released electrons flow out, thereby converting the mechanical work into the electrical energy (Figure 9 (a) and (b)). A total of 900 pairs of comb electrodes are integrated into a 30 mm X 20 mm chip (Figure 9 (c)). The resonant frequency of the device was specifically designed at 125 Hz to capture environmental vibrations, which were identified as the desired energy source through experimental characterization. When the electret film was polarized to -200 V, the maximal achievable for power for improved geometries was measured to be only 70  $\mu\text{W}$  at an acceleration of 0.05 g.

A new type of in-plane MEMS electret energy harvester has been developed by Qianyan Fu and Yuji Suzuki [138]. This harvester utilizes combined electrodes of overlapping-area-change and gap-closing types to achieve significant power output under both low and high vibration accelerations. The researchers have successfully fabricated an initial prototype using the single layer silicon-on-insulator process. To ensure uniform surface potential, soft-X-ray charging

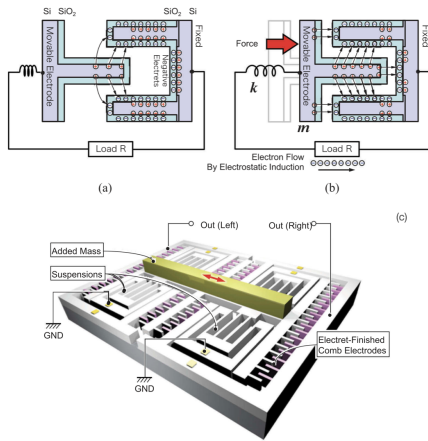


Figure 9: (a) Detailed view of the electrostatic induction. The surface of the fixed electrode is coated with a negatively charged silicon oxide. The charges are bound with the positive charge at the silicon oxide/silicon interface at the rest position. (b) When the movable electrode is inserted into the fixed ones, the electrical flux between the negative and positive charges are rearranged in part, and the released electrons flow out, thereby converting the mechanical work into the electrical energy. (c) Schematic illustration of electrostatic induction type VDRG. High-density comb electrodes are used to increase the areal mechano-electric coupling. A mass is attached on the movable electrode to increase the mechanical quality factor. Figure and Captions reproduced from [137] with permission from National Institute for Materials science in partnership with Taylor & Francis Group, copyright 2019.

is utilized to establish approximately 60 V on vertical electrets located on the sidewall of the comb fingers. The harvester has demonstrated an output power of up to  $1.19 \mu\text{W}$  at a frequency of 552 Hz and an acceleration of 2.15 g, resulting in an impressive effectiveness of 27.2%.

Lu et al [139] present the first instance of a fully flexible electret-based e-KEH. The proposed electret utilizes PVDF-PTFD nanofibrous material, covered with a layer of Parylene C. This arrangement offers several advantages, including faster stabilization of surface potential compared to a flat Parylene C thin film, as well as enhanced charge storage stability. During a pressing operation with a maximum force of 0.5 N and a 3-layers electret configuration, the device's capacitance increases significantly from 25 to 100 pF.

When operated with an optimal resistive load of  $16 \text{ M}\Omega$  and manually pressed, the device demonstrates impressive performance metrics. It achieves a peak instantaneous power output of up to  $45.6 \mu\text{W}$  and an average energy output of  $54 \text{ nJ}$  per stroke. These values translate to a peak instantaneous power density of  $7.3 \mu\text{W cm}^{-2}$  and an average energy density of  $8.6 \text{ nJ cm}^{-2}$  per stroke.

Over the span of 450 manual strokes, the prototype effectively charges a  $10 \text{ nF}$  capacitor to 8.5 V using a full-wave diode bridge. In a separate experiment involving a  $1 \mu\text{F}$  capacitor, a pressing movement frequency of 10 Hz driven by a vibrator with a maximum force of 0.5 N results in an energy delivery rate of  $9.9 \text{ nJ}$  per stroke.

#### 4.3. Sensors powered by Electrets

Stand-alone sensors were produced using electrets [140]. Zhu and colleagues [141] have presented their findings on a flexible comb-electrode triboelectric-electret coupling nanogenerator. This nanogenerator incorporates a separated friction microfiber object, enabling self-powered tracking of position, motion direction, and acceleration, as well as energy harvesting capabilities. The power generation occurs through the coupling of electrostatic and triboelectric effects among the separated triboelectric object, a polytetrafluoroethylene (PTFE) film, and interdigital electrodes. Under an acceleration of  $1 \text{ m}\cdot\text{s}^{-2}$ , the PTFE film charged with corona exhibited three times higher short-circuit current ( $I_{sc}$ ) and six times higher open-circuit voltage ( $V_{oc}$ ) compared to the uncharged PTFE film. This indicates a significant increase in power generation. The device demonstrates promising potential as a self-powered acceleration tracking

sensor, thanks to the stable voltage output during the friction process between the separated components and the numerical relationship between  $I_{sc}$  and increased accelerations.

Chen et al.[142] have developed a pressure sensor capable of achieving both high sensitivity and a wide pressure range presented in Figure 10. To enhance sensing performance, they designed a hierarchical elastomer microstructure (HEM) consisting of two-stage conical polydimethylsiloxane (PDMS) structures with heights of approximately  $900\ \mu\text{m}$  and  $450\ \mu\text{m}$ . These structures serve as supporting elements to create a highly compressible and adjustable gap. This is crucial because the natural air gap in flexible conformal sensors, without supporting structures, is often small and challenging to control. Such limitations can restrict the sensor's pressure sensing range and sensitivity. The PDMS structures in the HEM are covered with two ultrathin films. The first film is a fluorinated ethylene propylene (FEP)/Ag film with a thickness of around  $12.5\ \mu\text{m}$ , and the second film is an Ag/polyethylene terephthalate (PET) film measuring approximately  $8\ \mu\text{m}$ . Before assembling the device, the polymer side of the FEP/Ag film is treated with negative corona charging to transform it into an electret. The charge stability of the FEP electret initially decays rapidly within the first ten days but then stabilizes at approximately  $-1.1\ \text{mC}\cdot\text{m}^{-2}$ . The Highly Sensitive Pressure Sensor operates similarly to traditional self-powered pressure sensors based on electrostatic nanogenerators. When external pressure is applied, the deformation of the PDMS elastomer causes electrons to flow from the bottom electrode to the top electrode in a short-circuit state. Upon pressure release, the PDMS elastomer rebounds, causing reverse charge flow. This cyclic compression and release generate a potential difference between the electrodes, driving charges to flow in an external circuit. The resulting hierarchical self-powered pressure sensor (HSPS) exhibits impressive characteristics. It achieves a high sensitivity of  $7.989\ \text{V}\cdot\text{kPa}^{-1}$ , a wide working pressure range of  $0.1\text{--}60\ \text{kPa}$ , a fast response time of  $40\ \text{ms}$ , and a high signal-to-noise ratio of  $38\ \text{dB}$ . Additionally, the HSPS demonstrates excellent stability, making it suitable for various applications, including pulse, artery, heart condition, and blood pressure monitoring.

Electrets have gained significant attention in numerous biomedical applications, including bone regeneration, wound healing, nerve regeneration, drug delivery, and wearable electronics, due to their ex-

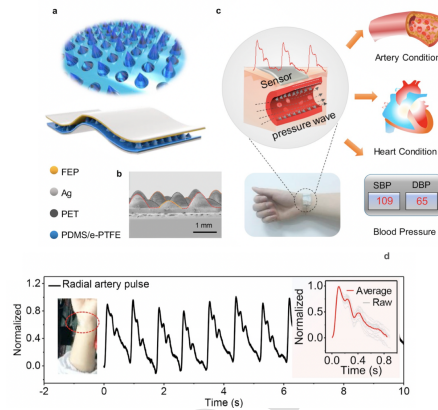


Figure 10: (a) Schematic structure of pressure sensor and the illustration of the pressure sensor for real-time continuous cardiovascular monitoring. (b) SEM image of the hierarchical structure. (c) The pressure sensor is capable of multifunctional cardiovascular monitoring (d) Radial arterial pulse waves of a 30 years old healthy female. Inset is the enlarged view of each cycle. Figure and Captions reproduced from [142] with permission from Elsevier, copyright 2020.

cellent performance, strong resilience, reliability, extended charging lifespan, and capacity to deliver internal electrical stimulation. Yu et al [143] developed a novel electret-based bio-nanogenerator specifically for electrically stimulated osteogenesis. The fabrication process involved utilizing a two-component-dispersed coaxial electrospinning technique to create porous aligning nanofibers. These nanofibers functioned as a surface charge self-recovery electret mat, enabling energy conversion. Upon implantation, the electret mat interacted with interstitial fluid and the host's stimulated objects, forming a host-coupling bio-nanogenerator (HCBG). During movement of muscle groups, the HCBG effectively harvested biomechanical energy and established an electrical stimulation environment to trigger osteogenesis. The performance of the HCBG was comprehensively evaluated both theoretically and experimentally under various conditions. Remarkable enhancements in osteogenic differentiation *in vitro* and successful bone repair *in vivo* were observed. Furthermore, the study delved into the mechanism of calcium ion-induced osteogenesis under electrical stimulation. This research introduces the concept of host coupling for implantable self-powered energy conversion systems and represents an exploratory step towards the field of tissue regeneration therapy.

#### 4.4. Conclusions and Outlooks for Electrets

Electrets have been extensively studied and proven to possess several advantages, including permanent polarization, low cost, stable performance, and good biocompatibility. Moreover, they have the ability to generate endogenous electrical stimulation when exposed to an external electric field. However, there are key issues that need to be addressed to further advance the development of electrets. Charging electrets is an issue. Various charging methods, such as corona charging, soft X-ray irradiation, thermal charging, contact charging, and electron beam injection, have been developed. It is first required to simplify the charging method that hinder industrial-scale production. Charge density is a crucial parameter for assessing the charge storage capacity of electrets. Currently, most electret charges are stored on the surface of dielectric materials and often lack sufficient charge density to meet practical application requirements. To enhance charge density, future development could focus on promoting charge generation inside the dielectric material. This could be achieved through the fabrication of solid porous electrets or hydrogel electrets with a network structure. Last but not the least, long-term stability is a crucial factor for the practical application of electrets. The charge stored in electret materials tends to decay over time, leading to a decrease in performance. Therefore, it is important to develop strategies to improve the long-term stability of electrets, such as exploring new dielectric materials with enhanced charge retention properties or incorporating stabilizing additives.

It is essential to address these challenges in order to drive the further progress of electrets, unlocking their full potential in various applications.

### 5. Mechanical vibration energy harvesting using triboelectric materials for sensor powering

#### 5.1. Triboelectricity

Due to external mechanical energy, two different materials may become electrically charged after being into contacts. This phenomenon, called tribo-electrification, may be used to produce electricity. During a contact-separation phase, two materials, if connected by electrodes and an electric circuit, will produce electric currents. This process relies on two mechanisms: contact electrification and electrostatic induction.

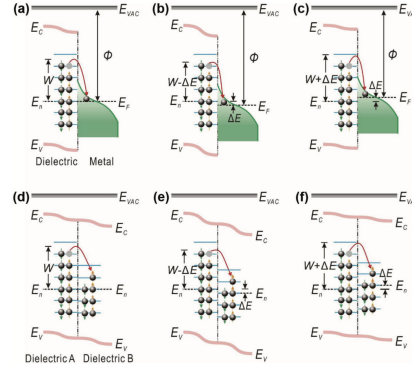


Figure 11: Surface state models for explaining the regulation of the potential barrier height of materials during CE, depending on the work function or contact potential difference of the contacted materials. Charge transfer between a dielectric (with initial negative charges) and a metal when  $E_n$  of the former is a) as high as, b) higher than, and c) lower than  $E_f$  of the latter. Charge transfer between dielectric A (with initial negative charges) and dielectric B when  $E_n$  of the former is d) as high as, e) higher than, and f) lower than that of the latter. EVAC, vacuum level;  $E_C$ , conduction band;  $E_V$ , valence band;  $E_n$ , neutral level of surface states;  $W$ , potential barrier;  $\Phi$ , work function; and  $E_F$ , Fermi level. Figure and Captions reproduced from [147] with permission from John Wiley and Sons, copyright 2019.

#### 5.1.1. Contact electrification

Although known since antiquity, the microscopic origin of tribo-electrification is still under debate. The charge transfer might originate from three different processes: electron transfer, ion transfer[144, 145], and material abrasion and deposition of charged debris[146] on both sides of the material. As we will see in the following, the main picture that is currently emerging links these phenomena mainly to electron transport [148]. In the case of metal-metal contact, electrons are transferred [149]. Before contact, the levels of the vacuum are aligned, while after the contact, the Fermi levels are aligned. To reach this equilibrium, electrons of the metal which has the highest Fermi level (noted as A) will go to the metal which has the lowest Fermi level (noted as B). Therefore, the interface on the side (A) is positively charged, while the interface on the (B) side is negatively charged. At the equilibrium, since the Fermi level are equal, a contact potential is established as:  $V_C = \phi_B - \phi_A$  where  $\phi_B = E_{vac} - E_{F,B}$  and  $\phi_A = E_{vac} - E_{F,A}$  with  $E_{vac}$  the vacuum energy,  $E_{F,A}$  and  $E_{F,B}$  the Fermi energy of metal A and B, respectively. After contact, a charge remains trapped on the metals. This charge is equal to  $Q = C_0 V_C$  where  $C_0$  is the capacitance of the

contact at separation  $x_t$  where tunneling effect disappears. As  $x_t$  is small, the potential at  $x_t$  is roughly equal to the contact potential  $V_C$ . At first sight,  $Q$  might depend on the rate at which the metals are separated. This dependence is very low and not significant for practical purposes. The time scale involved in the decay of the charge is equal to  $\tau = RC$  where  $R$  is the resistance of the contact and  $C$  its capacitance at distance  $x$ . For distances  $x$  below  $x_t$ , the characteristic time is very short as  $R$  is low and  $C$  varies slowly as a function of the separation. The system goes very fast to equilibrium and charges go back to metal A. For distances  $x$  higher than  $x_t$ , the tunneling resistance is infinite whereas  $C$  still varies slowly. The characteristic time involved in the metal separation becomes shorter than  $\tau$ : charges are trapped and remains fixed beyond this point. This picture has been validated experimentally. The trapped charge varies linearly with the contact potential both measured by the traditional Kelvin technique [149].

Concerning metal-ceramic tribo-electrification, experimental evidences of electron transfers have been reported. The analysis of the decay of the charge trapped in the materials after contact electrification, [147] evidences electron thermionic emission on ceramic materials such as  $\text{SiO}_2$  or  $\text{Al}_2\text{O}_3$  [147] (see Figure11).

It is possible to account for the electrification of a ceramic-metal contact by using an energy band diagram. The energy levels of a metal are characterized by a Fermi energy. The energy levels of a dielectric are characterized by its conduction band and its valence band. To understand electronic transfer, it is necessary to consider specific surface states that have an energy in the band gap. At the contact with the metal, the valence and conduction bands of the dielectric are deformed. If the edge of the valence band is below the Fermi level, electrons of the metal will be able to populate surface states of the dielectric, they leave the metal and make appear a positive charge on it. This phenomenon is accompanied as before by the appearance of a contact potential between the dielectric and the metal which is responsible for the capture of charges. The energy band model explains the electrification of metal-metal and metal-dielectric contacts, but fails to describe the contact between two polymers, as there are no quantified energy in polymers. To explain the case of polymer-polymer contact, we suppose that an atom is a potential well in which the outer-shell electrons are loosely bounded [150] (see Figure 12).

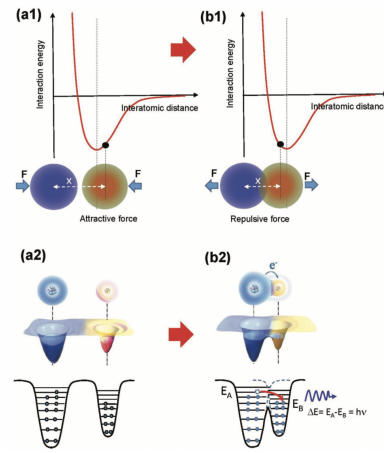


Figure 12: The overlapped electron-cloud model proposed for explaining CE and charge transfer between two atoms for a general case. (a1,b1) Interatomic interaction potential between two atoms when the force between the two is attractive and repulsive, respectively, by applying an external compressive force. Experiments found that electron transfer occurs only when the two atoms are in the repulsive interaction, for example, in the case when the two atoms have strong electron-cloud overlap. (a2,b2) Schematic of the electron cloud and potential energy well model of two atoms belonging to two materials A and B when they are separated and in close contact, respectively. Electron transition from A atom to B atom is possible due to the lowered potential barrier by the external force, resulting in the occurrence of CE. This is simply referred to as Wang transition for CE. Figure and Captions reproduced from [150] with permission from John Wiley and Sons, copyright 2020.

Before the contact, the electron clouds have different energies  $E_A$  and  $E_B$ . However, electrons cannot be transferred from one material to the other because of the potential wells and the value of the extraction energy. However while in contact, the electron clouds overlap. The extraction energies disappear, and the electrons transfer from the material where the energy is the highest to the one where the energy is the lowest. This transfer is strengthened by the mechanical energy that presses the contact. After separation, the charges remains as static charge on the material surface.

Although electrons are or can be clearly involved in the electrification of metal-metal, metal-dielectric and that the previous model can be generalized to polymer-polymer contacts [151], some electrification between two polymer surface clearly seems to rely on the transfer of ions or matter. Using Kelvin force microscopy, Baytekin and al.[146] showed that after electrification between two polymers, each surface bears nanoscale areas of different charges that they dubbed charge mosaics. They argued that contact charging could involve heterolytic bond breaking and that the creation of the charge mosaics comes from the transfer of patches of charged material between contacting surfaces. Everyday life surfaces do not exist in a world without humidity. It is thus necessary to take into account the role of atmospheric humidity and the presence of layers of water adsorbed on surfaces to understand the mechanisms at play. In studies of polymers containing covalently bonded and mobile ions, Diaz and coworkers[144, 145] showed that the maximum trapped charge was obtained at 30 percent relative humidity. At high humidity, the presence of a large water layer increases the surface conductivity and thus the departure of accumulated charges to the bulk. In the absence of humidity, the lack of electrification of the contact suggests that the charges transported are ions. The presence of a water bridge and the high dielectric constant of water indicate that during contact, the mobile ions are distributed evenly in the water bridge. The charge separation takes place when the water bridge breaks into two thin films. The counter-ions released by the polymer with the most mobile counter-ions near the second surface are trapped by the separation. Both surfaces achieve a charge. This mechanism allows to understand what happens for neutral polymers without mobile counter ions. Anions in general and the hydroxide ion in particular tend to adsorb at the water/solid or water/air interfaces. This leads to the ap-

pearance of a negative surface potential more or less large depending on the absorption. When two different polymers are brought into contact, a rapid equilibrium of the hydroxide ions takes place, the polymer with the stronger affinity for the hydroxide ions covering itself with a greater quantity ion. The rupture of the liquid film leads, as in the previous case, to a surface separation. This mechanism is corroborated by the correlation between surface charge during electrification and zeta potential of the polymer [152].

To conclude, there is no single picture of contact electrification. At least four mechanisms may be involved: the transfer of electrons between metal-metal and metal-dielectric, the transfer of counter-ions from ionic layers, the transfer of hydroxide ion and the breakage of covalent bonds. However, electron transfer seems to be the predominant mechanism [153].

### 5.1.2. Electrostatic induction

The production of electricity in triboelectric materials originates in an electrostatic induction phenomenon. In order to take into account the charges created by the contact, Wang introduced in 2017[148] an additional polarization term  $P_s$  in the definition of the displacement vector  $D$ .

$$D = \epsilon_o E + P + P_s \quad (4)$$

The first term  $P$  is due to the existence of an external field and the second  $P_s$  to the existence of the charges that are independent of the external electrical field and come from the contact electrification. In this framework, the displacement current density  $J$  writes  $J = \frac{\partial D}{\partial t} = \epsilon_o \epsilon_r \frac{\partial D}{\partial t} + \frac{\partial P_s}{\partial t}$ . By integrating  $J$  on the surface the displacement current  $I_d = \frac{dQ}{dt}$  can be found.

It writes [154, 155, 19]:  $I_d = A \sigma_T \frac{dH}{dt} \frac{\frac{d_1 \epsilon_0 + d_2 \epsilon_0}{\epsilon_1 + \frac{d_2 \epsilon_0}{\epsilon_2}}}{(\frac{d_1 \epsilon_0}{\epsilon_1} + \frac{d_2 \epsilon_0}{\epsilon_2} + z)^2}$  where  $A$  is the contact surface,  $\frac{dH}{dt}$  the variation of the contact/separation between the two material ( $\frac{dH}{dt}$  depends upon the nature of the mechanical solicitation i.e. sliding or compressing),  $d_1$  (respectively  $d_2$ ) the thickness of the material 1 (respectively 2),  $\epsilon_1$  (respectively  $\epsilon_2$ ) the dielectric constant of material 1 (respectively 2),  $\epsilon_0$  the permittivity the vacuum,  $z$  the distance between the two triboelectric materials. The dielectric constants  $\epsilon_1$  and  $\epsilon_2$  are intrinsic properties of the materials,  $\sigma_T$  depends upon many factors and notably of the surface chemistry and structure.

### 5.2. Triboelectric materials

The triboelectric properties of materials are represented by their triboelectric surface charge density

(TEDC after undergoing a triboelectrification process (contact/separation or sliding) with a reference material (mercury and contact/separation in [156]). A triboelectric table is set up which classifies materials according to their TEDC versus mercury.

Chemical-Resistant Viton Fluoroelastomer, Rubber Acetal, Flame-retardant garolite, Garolite G-10 Clear cellulose display the highest negative TEDC close to  $-150 \mu C.m^{-2}$ . Delrin® Acetal Resin, Wood (marine-grade plywood) Wear-resistant slippery garolite, Super-stretchable and abrasion-resistant natural rubber, Oil-resistant buna-N rubber and Food-grade oil-resistant buna-N/vinyl rubber display the lowest negative or even positive value comprised between  $-10 \mu C.m^{-2}$  and  $+10 \mu C.m^{-2}$ . This table cannot quantitatively predict the charge that will be recovered in a contact between two different materials. However, if the contact mode is the same as the one used to establish the table, two materials displaying highly different charges with mercury will give rise to a high contact charge. On the contrary, two materials with close TEDC values result in a low charge. Moreover, the amplitude of the charge is qualitatively related to the relative positions of the materials in the table [156]. Note that the term  $\left(\frac{d_1\epsilon_0}{\epsilon_1} + \frac{d_2\epsilon_0}{\epsilon_2}\right) / \left(\frac{d_1\epsilon_0}{\epsilon_1} + \frac{d_2\epsilon_0}{\epsilon_2} + z\right)^2$  which represents electrostatic induction is roughly the same for all the classical materials. Finally, apart from the material, the performance of a triboelectric device depends on the  $\frac{dH}{dt}$  term, which is dominated by the mechanical structure of the device and by the loss from the frictional force. [157]. Working in non-contact mode or transforming linear motion into rotational motion (due to lack of space) is one way to improve the process. Many studies focused on modifying and increasing the surface charge. A solution for surface charge increase is to enlarge the effective surface during contact. Kim et al. [159] obtained a contact charge of  $788 \mu C.m^{-2}$  by using a gold electrode covered with gold nanodots for effective surface increase. While increasing effective surface by roughness, the second material must also be soft and flexible (elastic materials or liquid metal) in order to cover the created roughness.

Cheng et al. coupled a triboelectric nanogenerator (TENG) in contact mode with a variable capacitor [160]. They used the TENG and a rectifier circuit to charge the capacitor. The latter subjected to vibrations transmits an electric current. This technique allows to work with important electric charges. Indeed, as there is no contact between the two surfaces

of the capacitor, it is more difficult to create an electric field that leads to the ionization of the air. They obtained a maximum effective charge density of  $490 \mu C.m^{-2}$ .

Liu et al. [161] coupled a TENG in contact mode with a generator and a fixed value capacitor. They achieve charge excitation through applying voltage to the main TENG, and an alternating current is produced by using a fixed value ceramic capacitor to store charges. Charges as high as  $1.25 mC.m^{-2}$  can be achieved. Other strategy concerns surface chemical modifications and insertion of charge trap layer (mixture of carbon nanotube and polymer for example in the material bulk [162]).

An important strategy concerns the use of an intermediate storage layer. Chun et al. reported [158] a TENG device composed of three layers : a top layer made Aluminium/polydimethylsiloxane, a bottom layer made of Aluminium and an inserted electric double layer made of Aluminium coated by gold nanoparticles. They obtained a power density of  $480 W.m^{-2}$  for a load resistance of  $10 M\Omega$ . The device of centimeter size ( $2 cm \times 2 cm$ ) was operated in contact/separation mode at a frequency of  $3 Hz$  under a force of  $60 N$  and an amplitude of displacement of  $1.5 cm$ . The conversion rate of the injected energy into recovered energy is equal to  $0.224$ . The principle of the process is given in Figure 13 and Figure 14. When a force is applied to the nanogenerator, the porous film and the intermediate layer are brought into contact. Positive charges appear on the surface of the intermediate layer and negative charges on the porous film. When the force is continued to be applied, the two layers come into contact with the ground and then with the bottom layer. When the force is withdrawn, the three layers separate simultaneously. The positive charges of the intermediate layer induce the flow of electrons from the ground to the intermediate layer and the negative charges of the porous film induce a movement of electrons from the upper electrode to the lower electrode. After the first cycle, the upper electrode is positively charged and the porous film is negatively charged, while the lower electrode is negatively charged and the intermediate layer is neutral (see Figure 13). When an external force is again applied to the nanogenerator, the displacement of the negatively charged porous film electrostatically induces positive charges on the middle layer surface, while negative charges are induced on the opposite layer surface. When the force is further applied, the negative charges on the mid-

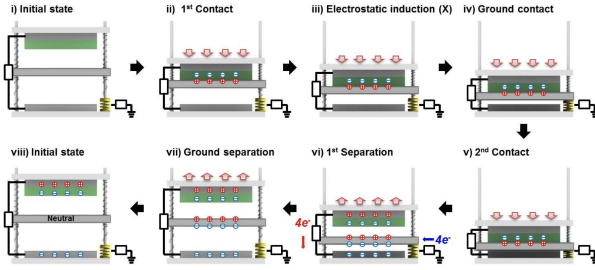


Figure 13: Working mechanism for the generation of output voltage and current in the TENG under external force. First cycle. Figure reproduced from [158] with permission from Springer Nature, copyright 2016.

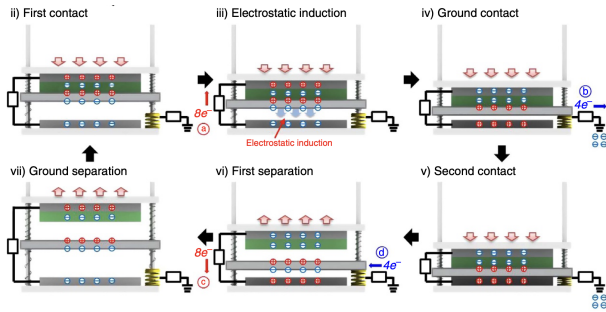


Figure 14: Working mechanism for the generation of output voltage and current in the TENG under external force after the first cycle. Figure reproduced from [158] with permission from Springer Nature, copyright 2016.

dle layer induce positive charges on the bottom layer, resulting in a flow of electrons through the external circuit. Then, the middle layer contacts the ground point and the electrons flow to ground, resulting in a current in the circuit connected to ground. When the force is removed, the three layers separate simultaneously. The electrons go from the ground to the central layer (see the 4 electrons drawn in blue in Figure 14 below the red line). An important flow of electrons is set up from the top electrode to the bottom one (see the 8 electrons drawn in red on the Figure 14 below the red line). Such working principle is different from the charge generation mechanism of a conventional TENG. And it accounts for a considerably higher electrical potential, ideally twice higher, compared to a conventional TENG (see Figure 14). Using this same approach with a silver particle layer, a polystyrene layer and a fluoropolymer layer, Kim et al. [163] produced a power equal to  $818 \text{ mW}\cdot\text{m}^{-2}$ .

Xu et al. [164] used a structure with three layers to get high density energy. A charge pump is devised to pump charges into the floating layer. A charge pump is devised to pump charges into the floating

layer simultaneously. This device can achieve ultra-high effective surface charge density of  $1.02 \text{ mC}\cdot\text{m}^{-2}$ .

### 5.3. Triboelectric Nanogenerators (TENG)

The triboelectricity mechanism is successfully used to produce electricity through Triboelectricity Nano-Generators (TENG).

#### 5.3.1. TENG working principle and modes

There exists 4 basic working modes of TENGs (see Figure 15): contact-separation (CS) mode, single electrode (SE) mode, sliding (S) mode and freestanding triboelectric-layer (FT) mode.

The CS mode uses a displacement perpendicular to the two materials. When the two materials come into contact they become charged. The CS mode involves a closed circuit. In a closed circuit (i.e. if the two materials are connected by an electrical circuit), the negative charges present in material A induce a displacement of electrons from the electrode connected to A to the electrode connected to material B. This flow of electrons stops when the electrode connected

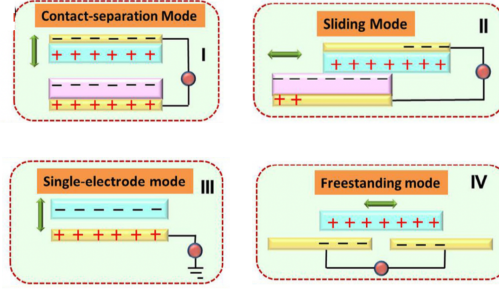


Figure 15: Four basic working modes of TENGs from [22] with permission from John Wiley and Sons, copyright 2020.

to B acquires a charge equal in absolute value and opposite to the charge carried by the material B.

The single electrode (SE) mode is comparable to the (CS) mode but operates in an open system. The two materials are not electrically connected. When they separate, the material that is not connected to the ground carries charges. The material that is connected to the ground has charges and an electron flow is established between the ground and the material. When the two materials come closer together, a reverse flow is established. The sliding mode (S) involves a movement parallel to the surface of the materials. The materials are in contact and the electrodes covering them are electrically connected. When the contact surface between the two materials decreases, unbalanced electrical charges appear within the two materials. To compensate for these charges, a movement of electrons takes place from one electrode to the other. A reverse movement takes place when the contact surface between the two materials increases. The free standing mode (FT) is a mode comparable to the (S) mode. It involves two materials in contact and a displacement along the plane of the materials. However, as in the SE mode, the two materials are not electrically connected. Instead, the bottom material is cut in two and the electron current flows through the electrodes covering the two identical materials at the bottom. Most applications are not limited to a single mode but use these modes in a coordinated way.

### 5.3.2. TENG performances

It is difficult to compare the performances reported in the different works in the literature, since the excitation conditions are often very different, especially in terms of applied force and frequency. A figure of merit was calculated and developed by Zi

et al. [165]. The figure of merit  $FOM_p$  allows to compare the performances of TENGs taking into account their environment. In sliding mode, it is defined by  $FOM_p = \frac{2\epsilon_0 E_m}{Ax_{max}}$ , where  $A$  is the triboelectrification area,  $x_{max}$  the maximum displacement.  $E_m$  is given by  $E_m = \frac{1}{2}Q_{max}(V_{OCV,max} + V'_{max})$  where  $Q_{max}$  is the maximum short circuit transferred charge,  $V_{OCV,max}$  is the maximum absolute achievable voltage at  $Q = 0$  and  $V'_{max}$  is the maximum absolute achievable voltage at  $Q_{max}$ . This figure of merit is unfortunately little used. To compare different results presented below, we must therefore keep in mind that the experimental conditions, especially the excitation conditions, are different.

By integrating a mechanical spring-based system in a TENG made with a copper plate and a PTFE film as triboelectric layers, Wang et al. [167] succeeded in obtaining an average power density of  $2 \text{ mW}\cdot\text{m}^{-2}$  under the experimental conditions of a frequency of 3.5 Hz, under a force of 0.6 N, a displacement amplitude of 2 cm, for a load resistance of  $10 \text{ M}\Omega$ . The conversion rate of the injected energy into recovered energy is equal to 0.18.

Pruvost et al. [102] obtained an average power density of  $2.25 \text{ mW}\cdot\text{m}^{-2}$  for a frequency of 40 Hz under a force of 0.012 N, an amplitude of displacement of 0.5 mm for a load resistance of  $10 \text{ M}\Omega$ . The conversion rate of the injected energy into recovered energy is equal to 0.10. The experimental results reported in the above-mentioned works do not take into account the electrical conversion. therefore, they do not discuss the problem of impedance matching.

As notice before, Chun et al. [158] obtained a power density of  $480 \text{ W}\cdot\text{m}^{-2}$  for a load resistance of  $10 \text{ M}\Omega$  using a TENG device composed of three layers Using this same approach with a silver particle layer, a polystyrene layer and a fluoropolymer layer, Kim et

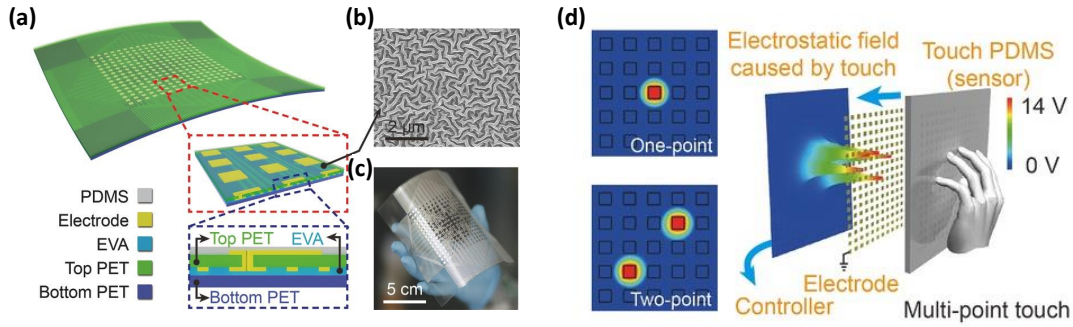


Figure 16: (a) Schematic of a 16 X 16 TESM. Insets: Partially enlarged tilted view and cross-sectional view of the structural design of the top and bottom, respectively. (b) Scanning electron microscopy (SEM) image of the etched PDMS surface microstructure. (c) Photograph of a fabricated 16 X 16 TESM with good flexibility (d) Schematic of the pressure mapping process. Figures and Captions adapted from [166] with permission from John Wiley and Sons, copyright 2016.

al. [163] produced a power equal to  $818 \text{ mW} \cdot \text{m}^{-2}$ .

Zhang et al.[171] obtained a power density of  $307 \text{ W m}^{-2}$  ie  $30 \text{ mW} \cdot \text{cm}^{-2}$  for a load resistance of  $5 \text{ M}\Omega$  using a all-green device made of cellulose-based material and commercial cellophane as tribological layers and graphite sheets as electrodes. To get these performances, the device of centimeter size ( $5 \text{ cm} \times 5 \text{ cm}$ ) was operated in contact/separation mode at a frequency of  $5 \text{ Hz}$ . A  $98 \text{ W} \cdot \text{m}^{-2}$  power density was obtained on a  $3 \text{ cm} \times 3 \text{ cm}$  on a TENG connected to a linear motor at a contact speed of  $1 \text{ m} \cdot \text{s}^{-1}$ . The device shows similar performances than fluoropolymer based TENGs [172] (power density  $6 \text{ W m}^{-2}$  for a load resistance of  $1 \text{ M}\Omega$  with an output current of  $1.5 \text{ mA}$  under  $6 \text{ N}$  of pushing force at  $5 \text{ Hz}$ ). This device is not sensitive to humidity.

An important problem is hindered in the reported powers above. It is complex to recover these powers in output circuits. The capacitance of a TENG is of the order of  $100 \text{ pF}$ . Such characteristics result in a low energy transfer efficiency, both for battery charging and electronic device powering. It is to notice that electronic devices generally have a much lower impedance ( $100$  of  $\mu\text{F}$ ). To recover energy, a simple rectifier circuit with diodes is not enough. In order to transfer a maximum amount of energy, it is important to insert an electronic stage between the battery or the supercapacitors that allows to adapt the impedance. This can be achieved by using  $N$  capacitors in series on charge and in parallel on discharge (basic switched capacitor convertor) or a fractal design based switched-capacitor-convertor

(FSCC)[173]. In the last situation, a energy transfer of  $94\%$  with an impedance reduction of  $750$  has been demonstrated. The use of an original system with two stages has also been proposed by Wang et al. [174]. In the first stage the energy is transferred to a low capacitance capacitor with a conversion ratio of  $0.75\%$  through a rectifier circuit. Then, the low capacity capacitor is connected, thanks to two automatic electronic switches, to a coupled inductance circuit that allows impedance matching [175].

#### 5.4. Sensors powered by triboelectricity

TENG technology can be used for both power supply and sensing in IoT applications[176]. There are already many insightful reviews with numerous examples [177, 178, 179, 47, 180]. Our goal here is not to be exhaustive but to show some examples of applications. It is to be noted that the literature on this activity is much more important than on the piezoelectric or electrostrictive themes.

##### 5.4.1. TENG as sensor in IoT applications

Various autonomous physical signal sensors have been designed using the principle of triboelectricity [22]. As explained in the previous paragraphs, pressure measuring presents wide applications in medical monitoring, building monitoring, hand held control of connected objects, and sensory robotics. In this context, many triboelectricity based pressure sensors have been developed.

Wang et al.[166] reported a self-powered touch pad with  $36 \times 20$  pixels using a triboelectric generator

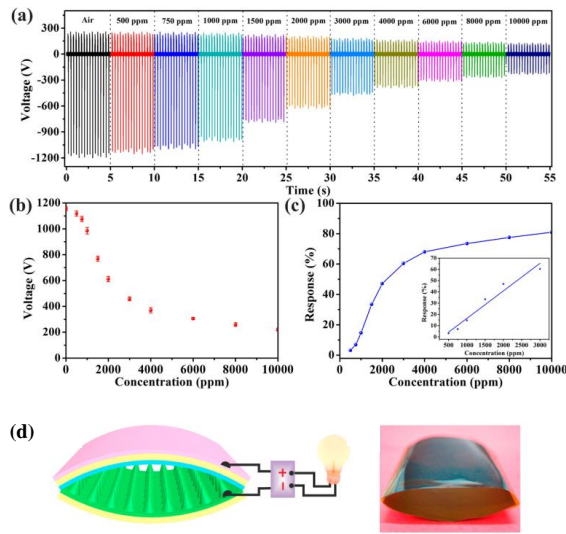


Figure 17: (a) (b) The output voltage of C PANI TENG based nanosensor at room temperature in air and NH<sub>3</sub> with various concentrations (from 500 ppm to 10,000 ppm), (c) The relationship between the response of the C PANI TENG ((V<sub>air-Vgas</sub>)/V<sub>air</sub>) and the concentration of NH<sub>3</sub>. Inset is the response curve with NH<sub>3</sub> concentration ranging from 500 ppm to 10,000 ppm. (d) Schematic illustrate and photograph of the designed PANI based TENG with an arch-shaped structure. Figures and captions adapted from [168] with permission from Elsevier, copyright 2018.

(see Figure 16). A PDMS film serves as an electrofication layer that generates a triboelectric effect upon contact with the silver nanoprinted electrodes. The system is durable and presents excellent performance with a pressure sensitivity exceeding  $0.06 \text{ kPa}^{-1}$ . The response time is less than a few milli seconds. A stylus writing on the touch pad with a velocity of the order of  $50 \text{ mm}\cdot\text{s}^{-1}$  can be easily detected. Cui et al. [168] reported a self-powered NH<sub>3</sub> nanosensor based on TENG (see Figure 17). PANI nanofibers are a common NH<sub>3</sub> sensing material. The adsorption of NH<sub>3</sub> can transform C-PANI nanofibers into N-Nani nanofibers. The triboelectric properties of the two fibers are very different due to dissimilar electrical conductivity properties. The authors constructed a conventional device by inserting a PANI fiber film and a PVDF film into two electrodes. These signals are obtained at a frequency of 3vHz under the action of a linear motor that simulates the environment. The TENG is solicited in contact mode. The C-PANI-TENG has a much higher output performance than the N-PANI-TENG. The peak short-circuit current value and output voltage of C-PANI-TENG reach  $45.70 \mu\text{A}$  and  $1186 \text{ V}$ , respectively, which are one hundred times higher than those of N-PANI-TENG

( $0.26 \mu\text{A}$  and  $6.70 \text{ V}$ ). Tracking these measurements after calibration provides a measure of gas concentration. The system is durable and shows no variation after 15,000 cycles. In the presence of NH<sub>3</sub>, the output voltage of the TENG decreases rapidly to a relatively stable value within 40 seconds (response time). If pure air is injected again, the voltage rises again within 250 s. The longer recovery time is due to a lower desorption rate of NH<sub>3</sub> molecules on the PANI compared with its absorption rate. The sensor works for NH<sub>3</sub> concentrations between 500 ppm and 10000 ppm. TENGs present also wide applications as biomedical sensors. Numerous research works have been performed in this direction in the last decades. It is based on the energy harvesting of vital signals (heart sounds, blood pressure, breathing) to analyze patient's health state or to its reactions to an aggressive environment. These devices are designed to be worn directly on the skin or integrated into textiles. In the same spirit CO<sub>2</sub> sensors have been developed [153, 181]. Cardiology is one of the most popular applications for TENG biomedical sensor which can measure heart pulse or monitor arterial pressure. In 2015, Yang et al.[182] developed a sensor made by a TENG, encompassing a polytetrafluoroethylene

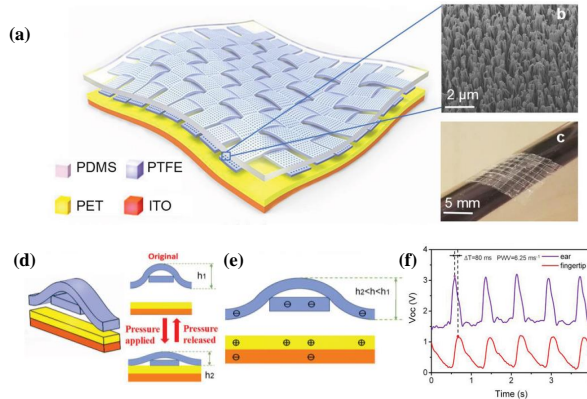


Figure 18: A weaving constructed self-powered pressure sensor (WCSPS) for self-powered measurement of human Pulse Wave Velocity and Blood Pressure. a) Schematic illustration of the flexible weaving constructed self-powered pressure sensor. b) A SEM image of plasma-etched PTFE nanowires. The scale bar is  $2 \mu\text{m}$ . c) A photograph showing an as-fabricated WCSPS, which is flexible, lightweight, and can be easily wrapped onto a curved surface. The scale bar is 5 mm. d) Schematic diagram of the cross-sectional view of a single unit of the WCSPS. The right side illustrates the two conditions that when the device is in its original state ( $h_1$ ) and when the external pressure was applied ( $h_2$ ). e) An illustration showing the electrical signal generation process of the WCSPS [169] (f) The real-time health monitoring of middle-aged and aged people. Figures and captions adapted from [169] with permission from John Wiley and Sons, copyright 2018.

(PTFE) membrane layer and a nylon layer as the triboelectric pairs. The nylon layer was covered by an indium tin oxide (ITO) electrode. Yang et al. utilized this sensor to monitor human arterial pulse waves in real-time at the carotid, wrist, and chest. The device has a low detection limit of 2.5 Pa and a high sensitivity  $51 \text{ mV.Pa}^{-1}$ . Bai et al. [183] placed a fluorinated ethylene propylene membrane and a latex membrane where between two copper electrodes to build a TENG. This very simple device was used to monitor respirations and heart beat for security surveillance.

Others TENGs have been developed to monitor the shape of the heart wave and not simply the rate of the heart wave. It is not a easy task to measure blood pressures, which remains one of the most important vital signals for disease evolution monitoring and patient condition tracking. To achieve this goal, Meng et al. [169] designed a pressure sensor based on a TENG realized in simple contact mode (see Figure 18). Plasma etched polytetrafluoroethylene (PTFE), polyethylene terephthalate (PET) and indiumtin oxide (ITO) electrode serve as triboelectric materials. At the constant frequency of 2 Hz, the pressure sensitivity of  $45.7 \text{ mV.Pa}^{-1}$  is achieved in the lower-pressure ( $< 0.71 \text{ kPa}$ ) region. The authors measured the shape of the arterial signal on two points of the body. They deduced from the temporal

shift of the signals an important parameter the pulse wave velocity (PWV) which depends linearly on the arterial pressure. This calibration requires the use of studies on patient cohorts. In a simpler way, it allows to track the condition evolution of a given patient.

Yi et al. [184] produced a stretchable rubber based TENG made of a layer of elastic rubber and a layer of Aluminium. The respiration movements cause the stretching of the elastic rubber and provide a change of triboelectric charge distribution and density on the rubber surface relative to the Al surface. This leads to a change of triboelectric charge distribution and a detectable alternating charge flow.

#### 5.4.2. Sensors powered by a TENG with a storage system

Liu et al. [170] developed a triboelectric system based on contact between seawater and a triboelectric material. The authors constructed a triboelectric device (coined D-TENG) from a thin PTFE foil and an aluminum electrode placed between two Kapton and PVC insulators. On top of the device an aluminum U-shaped electrode is connected to the aluminum plate. This device is coined U-TENG. In a conventional device without aluminum on top (D-TENG), the sea water arrives on the PET film which has a negative charge acquired during the first contacts with the sea water. This charge is balanced

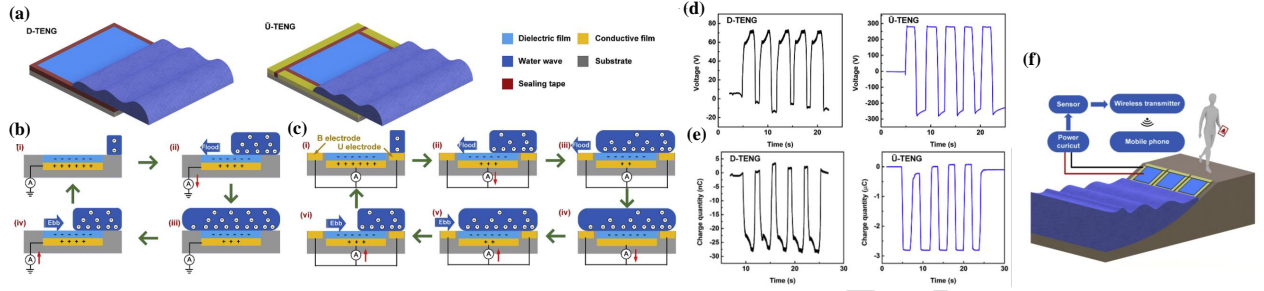


Figure 19: (a)The structure of the D-TENG and the U-TENG. (b) Work mechanism of the D-TENG. (c) Work mechanism of the U-TENG. (d) Open-circuit voltage comparison of the D-TENG and the U-TENG. (e) Transfer charge quantity comparison of the D-TENG and the U-TENG (f)Flow chart diagram of applications of U-TENG as blue energy harvester. Figure reproduced from [170] with permission from Elsevier, copyright 2019.

by positive charges on the aluminum. The seawater partly screens the negative charges of the PET. Electrons come from the earth to compensate. At equilibrium, there are more charges on the aluminum that are compensated by less persistent charges not balanced by seawater. When the seawater withdraws, the reverse process starts. If an aluminum electrode is placed above the device, the electrons no longer come from the earth but from this electrode. They maintain a strong negative charge on the high part of the device and thus fill completely the positive charge on the aluminium part. This device thus makes it possible to exacerbate the operation of TENG (see Figure 19). Open-circuit voltage increases from 73.1 V to 283.1 V, transfer charge quantity increases from 28.4 nC to 2.8  $\mu\text{C}$  and short-circuit current increases from 0.4  $\mu\text{A}$  to 10.8  $\mu\text{A}$  using this strategy. Based on this system, the authors present a WIFI data transmission system that is powered by the energy stored in the capacitors. This wireless signal transmission system is important for further seashore IoT applications, inspectors can obtain information from distributed signal transmitting station when they take an inspection tour of seashore area.

#### 5.4.3. Sensors powered by a TENG without a storage system

Wang[174] first applied TENGs to human signal energy harvesting. He developed a multilayer contact-mode TENG made of aluminum and fluorinated ethylene propylene films. Integrated into the soles of shoes, the walking of a human being can drive this TENG to generate a charge of about 2.2 mC and an output voltage of about 700 V. By using an impedance matching system, they manage to charge a battery. The performances obtained are remarkable.

(see Figure 20). With a light palm tap at 1.6 hertz as the only power source, this device delivers 1.044 mW of direct current ( $7.34 \text{ W m}^{-3}$ ). There is neither battery in the system, nor storage system. The device can be used as a standard infinite life power source to continuously power many conventional electronic devices, such as thermometers, electrocardiographs, pedometers, wearable watches, scientific calculators, and wireless radio frequency communication systems. TENGs are particularly suited for IoT applications.

Kim et al. [163] reported a TENG for a self-powered security IoT system. The device includes a silver nanowire layer, a polystyrene layer, and a fluoropolymer contact layer. The presence of the transparent polystyrene layer acts as an intermediate charge storage layer and increases the power density of the ST-TENG to  $818 \text{ mW.m}^{-2}$ . The  $11 \text{ cm} \times 11 \text{ cm}$  size system is included in a floor. The passage of a passer-by allows to generate an electric signal strong enough to send messages to a data acquisition board. Then, the data acquisition board reads and converts the transmitted analog electric signal to a digital signal by ADC conversion, and the board wirelessly sent the signal of the invader to the smartphone. All this connection is done through a simple AC-DC conversion bridge and capacitors without the use of batteries. The power generated by this device is important enough to avoid the use of complex energy transfer systems.

#### 5.5. Conclusions and Outlooks for TENG

The development of triboelectric nanogenerators has reached an exponential increase since the beginning of the century. All currents generated by a TENG type nanogenerator show alternating characteristics, which require a rectification process before

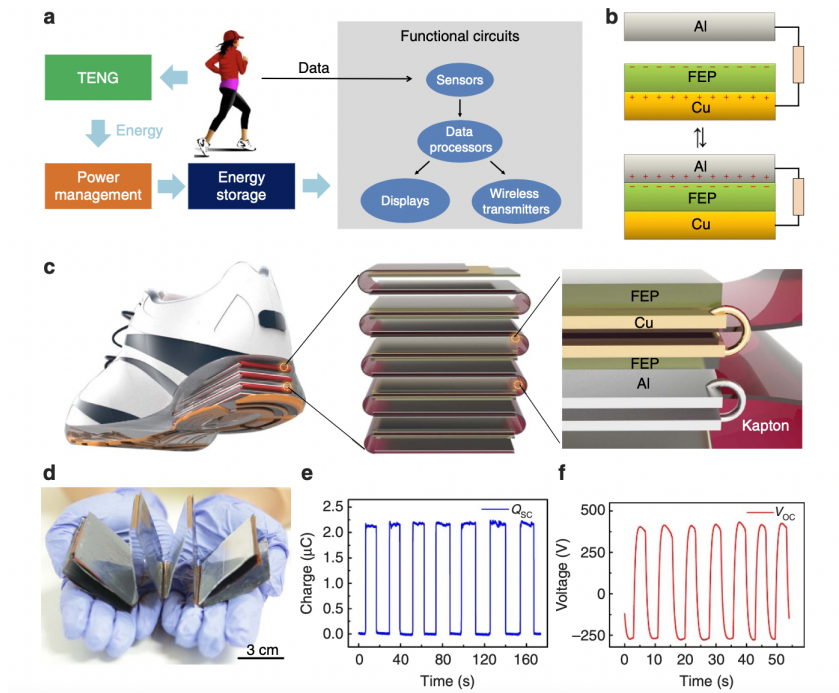


Figure 20: (a) System diagram of a TENG-based self-powered system. (b) Working mechanism of an attached-electrode contact-mode TENG. (c) Structure of the designed multilayer TENG. (d) Photo of an as-fabricated TENG. (e) Short-circuit current output and (f) open-circuit voltage output of the as-fabricated TENG. Figure reproduced from [174] with permission from Springer Nature, copyright 2015.

use. The power densities obtained by the TENG reach an order of  $0.1\text{-}1\text{ mW}\cdot\text{cm}^2$  under moderate forces. Such performance is lower than that reported for piezoelectric materials, which is around  $1\text{-}10\text{ mW}\cdot\text{cm}^2$  under the same solicitations. However, triboelectric devices have many advantages. There are almost unlimited candidates of materials due to the nature of triboelectric effect [22]. It is possible to integrate materials of low cost and of biosources. TENG devices are mechanically reliable. They endure over thousands to millions of cyclic impacts without significant failures of the structures or decay of the output performance [22]. The challenges concerning TENG devices are the control of humidity and the reduction in size of the devices. Existing devices are of medium size due to limited power density.

## 6. Osmotic energy harvesting systems

There is an energy in nature whose resources are practically equal to those of mechanical energy: the energy of mixing or the osmotic energy. The osmotic energy (also named as Blue energy) [185, 186] is an underestimated energy source which presents major advantages both in its large energy potential and in its wide availability in all scales. Osmotic energy harvesting harnesses the energy released during the mixing procedure of solutions of different salinity [187] or of different solute concentrations. The potential of blue energy can be estimated by the theoretical calculations of Gibbs free energy  $\Delta G_{mix}$ . According to research works, a global power of  $2.4\text{-}2.6$  Terawatts is estimated for blue energy potential, considering all the rivers and effluents running to the sea [188]. This feature takes into account only the mixing of solutions of different salinity.

As illustrated in Figure 21, three major osmotic energy harvesting technologies, including pressure retarded osmosis (PRO), reverse electrodialysis (RED)

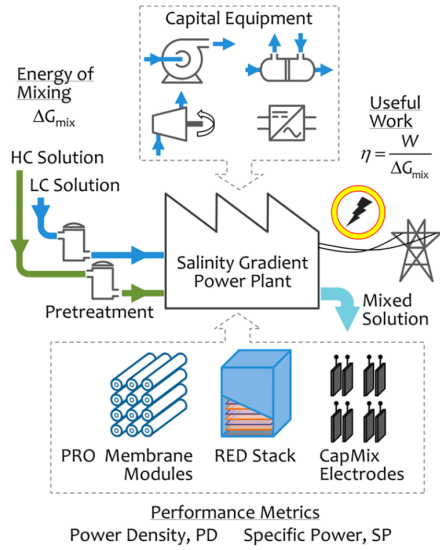


Figure 21: Schematic representation of a salinity gradient power generation facility. Figure reproduced from [189] with permission from American Chemical Society, copyright 2016.

and Capmixing, can be used to harvest osmotic energy. Briefly speaking, PRO is a semi-permeable membrane based technology where water flux driven by osmotic effect results in the volume increase of the pressurized concentrated solution chamber. The mechanical energy is then used to propel the turbine systems for electricity generation[190, 191]. Similarly, RED is also a membrane-based technology. Ion-exchange membranes (IEMs) are used to create an ionic flux under osmotic effect, which is then converted into electric current by redox reactions at electrodes[192, 193]. Capmixing systems designs a precise and engineered cycle to use double layer expansion on capacitive electrodes for osmotic energy harvesting[194]. Apart from large volume mixing of river and sea water at natural estuaries, which is limited by the salt solubility in the water (about 350 g/L), it is also possible to exploit systems with pH gradient. As reported by Kim et al., the mineralizing of  $\text{CO}_2$  gas in industrial alkaline wastes ( $\text{NaHCO}_3$  solutions) could effectively modify the pH in solution[195]. It is thus possible to establish a pH ratio across two compartments of  $\text{CO}_2$  and air-parged alkaline solutions separated by a non-selective membrane. The use of  $\text{MnO}_2$  electrodes in the system could efficiently develop a pH-gradient dependent potential difference. This is realized due to a reversible

redox reaction through intercalation/deintercalation or adsorption/desorption of protons. It is reported that a power density of  $0.82 \text{ W}\cdot\text{m}^{-2}$  is achieved in such system [195].

Osmotic energy exists widely in other forms at much smaller scale range. An example could be the biological salinity gradients of physiological fluids established across cell membranes or organs. Accordingly, we can also imagine miniaturized osmotic energy harvesting systems in small-scale applications including analytical sensor devices[196], ionic circuits[197] and biomedical applications[198, 199]. In this review, we mainly focus on miniaturized blue energy harvesting systems. Considering the complex accessory equipment (pump and turbine systems for PRO systems and hydraulic circuits for flow sweeping in Capmixing systems), RED systems remain the easiest method for miniaturized system powering. Thus we will restrict our discussions on RED systems. In the following sections, we will firstly begin with a detailed description of RED working principle and its current performances. This will be followed by a summary of miniaturized RED applications, along with the developing trend in the field.

### 6.1. How to generate electric power from osmosis

Blue energy recovery devices use selective membranes. We will first recall the operating principles of these membranes.

#### 6.1.1. Membrane potential and selectivity

Ion exchange membranes (IEMs) possess fixed charges and are generally classified into 3 categories: cation exchange membranes (CEMs), anion exchange membranes (AEMs) and bipolar membranes[200]. Negatively charged chemical groups of strong or weak acids, including sulphonate ( $\text{SO}_3^-$ ), phosphate ( $\text{PO}_3^-$ ), carboxyl groups ( $\text{COO}^-$ ), are used in CEMs. AEMs, on the contrary, possess positively charged groups, such as ammonium ( $-\text{NR}_3^+$ ), primary amine ( $-\text{NH}_2$ ), and etc. In addition to CEMs and AEMs, bipolar membranes possess both positive and negative chemical groups and are widely applied in water splitting procedures[201].

When an IEM is placed in middle of two solutions chambers of different concentrations ( $c_{\text{bulk},L}$  and  $c_{\text{bulk},R}$ ) as illustrated in Figure 22, an electrical potential difference  $\phi_m$  for a chemical species  $i$  is established. In order to explain ion transportation, here we define the electrochemical potential  $\tilde{\mu}_i$  (J/mol)

as the combination of chemical potential term  $\mu_i$  (J/mol) and electrical potential term  $\phi$  (V).

$$\tilde{\mu}_i = \mu_i + z_i F \phi = \mu_i^0 + RT \ln(\gamma_i c_i) + z_i F \phi \quad (5)$$

where  $z_i$  is the ion valence,  $F$  the Faraday constant,  $R$  the gas constant,  $T$  temperature,  $\gamma_i$  activity coefficient of species  $i$ , and  $c_i$  the ion concentration. According to Donnan equilibrium, the electrochemical potential at the solution-membrane interface is identical[202]. Thus it is possible to establish the equation below:

$$\mu_i^0 + RT \ln(\gamma_{i,s} c_{i,s}) + z_i F \phi_s = \mu_i^0 + RT \ln(\gamma_{i,m} c_{i,m}) + z_i F \phi \quad (6)$$

where suffix  $s$  and  $m$  represents the physical parameters in solution and in membrane, respectively. This leads to,

$$\Delta\phi_D = \phi_s - \phi_m = \frac{RT}{z_i F} \ln\left(\frac{\gamma_{i,m} c_{i,m}}{\gamma_{i,s} c_{i,s}}\right) \quad (7)$$

This potential difference  $\Delta\phi_D$  is known as Donnan potential. According to Equation 7, we have:

$$c_{i,m} \propto c_{i,s} \exp\left(\frac{z_i F}{RT} \Delta\phi_D\right) \quad (8)$$

According to the definition of Donnan potential established above, we can deduce  $\Delta\phi_D > 0$  for CEMs and  $\Delta\phi_D < 0$  for AEMs. As co-ions and counterions have opposite charge valences, the exponential part is correspondingly greater than 1 for counterions and less than 1 for co-ions[203]. This simple calculation explains the important concentration difference of co-ions and counter-ions in IEMs under Donnan exclusion effect. When IEM is placed between two chambers (1 and 2) of different salinities, two Donnan potentials appear separately at the both solution-membrane interfaces. The concentration difference established across the IEM could also result in a diffusion potential  $\phi_{diff}$ . This occurs due to the differences in ionic mobility in the IEM, which leads to a charge separation phenomenon[204, 205]. Similarly, stagnant diffusion layers (SDL) could establish on either side of the membrane, which leads to diffusion electrical potentials[206, 207]. Such phenomenon (concentration polarization effect) derives from the limitations of ion transportation at solution-membrane interfaces, and leads to an important effective potential drop[208, 209, 210, 211]. Combining these above-mentioned terms will lead to the membrane potential difference  $\phi_m$ , as illustrated in Figure 22.

$$\phi_m = \Delta\phi_{D,1} - \Delta\phi_{D,2} + \phi_{diff,m} + \phi_{diff,1} + \phi_{diff,2} \quad (9)$$

In the case of a rigorously selective membrane, zero co-ion flows present in membrane phase. Due to the electroneutrality condition, the diffusion potentials vanishes. Thus, the membrane potential is simplified as:

$$\phi_m = \frac{RT}{z_i F} \ln\left(\frac{\gamma_{i,2} c_{i,2}}{\gamma_{i,1} c_{i,1}}\right) \quad (10)$$

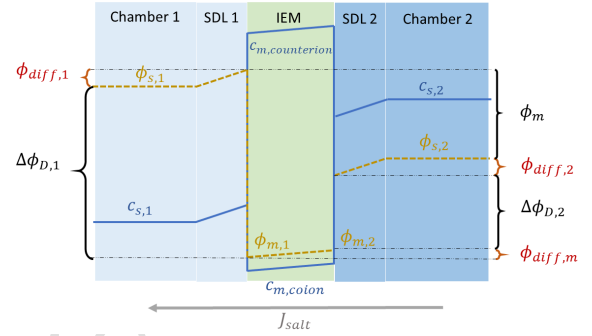


Figure 22: Schematic representation of concentration  $c$ , and potential  $\phi$ , profile in the bulk solutions, the stagnant diffusion layers (SDLs), and in an ion exchange membrane (IEM) in open-circuit conditions.

However, in real applications, membranes are never perfect. Dlugolecki et al. suggested a simple method for apparent selectivity measurement[212]. The experimental setup consists of a membrane placed in the middle of a saltwater chamber and a freshwater chamber with fixed concentration. The overall electrical potential established across the membrane  $E_{exp}$  can thus be measured at steady state. Then the perm-selectivity of the counter-ion is defined as

$$\alpha = \frac{E_{exp}}{\phi_m} \quad (11)$$

It is to notice that an ideal selectivity is obtained when  $\alpha$  is of unit value. In the case where selectivity is zero, the membrane is completely non-selective. The selectivity of membranes come from their morphology. The morphology of IEM membranes is quite complex. For example, the structure of Nafion membranes encompasses a connected network of hydrophilic clusters in a hydrophobic and semi-crystalline perfluorocarbon phase [213]. The structural nature of the ionic domains, such as the size, shape, and spatial distributions of the clusters is still under debate. The size of the channels in the connected network is assumed to be less than 0.5 nm. These channels are covered with surface charges coming from

the sulphate group  $\text{SO}_3^-$  in the Nafion situation. Due to the charge neutrality, counterions are attracted by the surface charges, leading to the formation of Electric Double Layer (EDL) composed of Stern layer and Gouy-Chapman layer[214, 215]. The thickness of EDL is characterized by the Debye length, which indicates the spatial range of unscreened ionic charges under electrostatic effect[216]. Typically for water at room temperature, the Debye length is estimated at 0.3 nm for a salt concentration of a 1 M[217]. Considering that the pore size in IEMs is comparable to Debye length, the surface charge thus governs the transportation of ions in this case. In fact, the permselectivity could be intuitively explained from an electrostatic point of view : counter-ions are attracted by the fixed charges in membranes while co-ions are electrically repulsed. The selectivity decrease is generally related to the existence of co-ion flux and water flux across the membrane[218]. A highly selective membrane is therefore a membrane with very small pore holes. The use of membranes in osmotic energy recovery devices requires the use of membranes that allow a large number of ions to pass through them, thus very permeable membranes. There is therefore a trade off to be found between permeability and selectivity.

This problem seemed to be solved for a while by the introduction of highly charged large hole membranes. Studies on single nanopores of a few tens of microns seemed to imply that gigantic powers could be obtained by using this type of membrane[219]. It is reported that a power density of 4 kW/m<sup>2</sup> is achieved with such nanofluidic system[219]. Gao et al. [220] showed that this way was a dead end. Collective effects prevent the scaling up of this process. When cations (or anions) are brought in excessively from one side of the membrane, there is a diffusion movement of the anions to cancel the electric charge. This creates a heterogeneous concentration distribution in the system called polarization concentration. This has the effect of decreasing the concentration difference on both sides of the membrane and therefore of strongly decreasing the membrane potential. When a single nanotube is considered the ions can diffuse from an infinite 3D space. When several nanotubes are close to each other, the polarization zones interact and the phenomenon is very important. This explains the failure of the scaling.

#### 6.1.2. Working principle of RED

RED devices take advantage of the potential difference that appears on an ion exchange membrane

when it separates two saline solutions of different concentrations. A series of pairs of cationic and anionic exchange membranes are placed in salt gradients. Under the effect of the saline gradient and the apparition of the potential difference, the ions migrate from the most concentrated solutions to the most diluted solutions. With the membranes being selective, an ionic flux is established. This is converted into an electronic flux at the electrodes by Faradaic reactions. The maximal gross power density produced under Faradaic conversion (i.e., the power density neglecting the viscous losses due to pumping and the process efficiency) is given by  $P_{max} = \frac{E_{ocv}^2}{4SR_{cell}}$ , where  $E_{ocv}$  is the open-circuit voltage,  $R_{cell}$  is the inner resistance of the cell and S is the surface of the membrane.  $E_{ocv}$  is the sum of the membranes potentials and of the electrodes drop potentials. The larger the membrane surface there is in a device, the higher power is generated.  $R_{cell}$  refers to the resistance of the cell and can be divided into two primary components. The first component, known as the ohmic component, pertains to the conductivity of the cell's components (such as the membrane, solutions, spacers, etc.). The second component, known as the non-ohmic component, is influenced by changes in concentration inside the cell. This non-ohmic component is caused by the polarization effect that occurs near membranes and by variations in salt concentration along the water channel [15].

#### 6.1.3. Power produced using RED

Pattle et al. [221] used over 45 membranes in their RED system, but only achieved a mild power density of 0.2 W.m<sup>-2</sup> due to the low efficiency of their stack. As a result, numerous studies have been conducted to increase the output power density of RED systems. Długolecki et al. [212] investigated the performance of various membranes commonly used in RED and predicted that a power density of 6 W.m<sup>-2</sup> could be achieved using commercial IEMs. Turek et al. [222] achieved a power density of 0.84 W per square meter of membrane with a high salinity gradient (approximately 200), while Veerman et al. obtained a power density of 0.9 W.m<sup>-2</sup> with a salinity difference of 30 g.L<sup>-1</sup> and 1 g.L<sup>-1</sup> of NaCl for the concentrated and diluted solutions, respectively. However, the high cell resistance of RED systems hinders their electrical performance [223]. Vermaas et al. [224] reported that decreasing the spacer thickness from 485  $\mu\text{m}$  to 100  $\mu\text{m}$  can reduce the ohmic resistance of the system by 4, and with this improvement, they achieved

a gross power density of  $1.8 \text{ W.m}^{-2}$  using only 5 pairs of IEMs. Nonetheless, thinner spacers were found to lead to a higher pressure loss. In this study, they achieved a net power density of  $1.2 \text{ W.m}^{-2}$ , which remains the highest documented experimental net power density to date.

Increasing the salt concentration and the temperature increases these performances. Using a single membrane and capacitive electrodes, Brahmi et al. [225] reports a net power density output of  $2 \text{ W.m}^{-2}$  was reported, with a concentration ratio of 300 (0.017 M and 5.13 M). For a concentration ratio of 500 (salted water 5 M, fresh water 0.01 M), Daniilidis et al. [226] measure a gross power of  $4 \text{ W.m}^{-2}$  at  $25^\circ\text{C}$  and  $7 \text{ W.m}^{-2}$  at  $60^\circ\text{C}$ . The powers that we have just reported are powers of the order of  $1 \text{ W.m}^{-2}$  ie  $100 \mu\text{W.cm}^{-2}$ ). They are therefore compatible with IoT type applications. We will see in the next frame applications along this line. Unlike the previous principles, the RED does not draw its energy from a mechanical signal. The current produced does not therefore allow the analysis of a pressure signal or the analysis of a vibration or a shock. It is therefore not possible to build pressure sensors or deformation sensors from reverse electrodyalisis devices. The only possible approach is to build energy producing devices that will allow to power sensors. The plan of the review will therefore differ from the previous paragraphs. We will simply focus on small-scale power generating systems and their application to sensors.

## 6.2. Harvesting devices

### 6.2.1. Miniaturized RED systems

One of the major advantages of RED technologies is its potential in both scaling up and miniaturization. Emerging researches focus on the development of mini-RED stacks in order to power future wearable devices, implantable sensors, bio-compatible and clinical implant systems, etc. To realize mini-RED devices, researchers can always find an exquisite and highly efficient example from nature: the electric organ of eels[227]. The electric organ is composed of long and thin cells separated by ion gradients[228]. The adjustment of  $\text{K}^+$  channels and  $\text{Na}^+$  channels could efficiently switch between rest stage (where zero voltage is generated) and firing stage (where a voltage of 150 mV appears across one single cell)[229], as illustrated in Figure 23(a) and (b).

Inspired by electrocyte in an electric eel which can generate potentials of 600 V, Xu and Lavan proposed in 2008 the artificial cell conception for biological ion concentration gradient harvesting[230].

Based on the model established for natural electrogenic cell, they proposed methods for constructing artificial cells which have higher power density output and energy conversion efficiency according to their theoretical calculation. Also inspired by electric eel organs, Schroeder et al. realized an excellent design of scalable stacking of miniature polyacrylamide hydrogel compartments coupled with series of alternative cation- and anion- selective hydrogel membranes[229]. Such design consists of a mini-RED repeating module composed of concentrated salinity hydrogel, cation-selective gel membrane, diluted salinity hydrogel and anion-selective gel membrane (Figure 23(c) and (d)). While stacking these modules in series up to 2449 units, an open-circuit potential of 110 V, along with a power density of  $27 \text{ mW.m}^{-2}$  per tetrameric gel cell is reported. The afore-mentioned work was followed by a similar ionic hydrogel battery in a microfluidic version realized by He et al.[231] They designed typical well arrays and microfluidic channels to enable fast hydrogel assembly within several minutes. This microfluidic design avoids the time-consuming step for hydrogel assembling and provides a further insight for the wide application of power supply for soft and wearable devices.

To fulfill the power supply demand of small scale devices, miniaturized batteries are being extensively studied. In the work of Banan Sadeghian et al., miniaturized RED systems with a diameter of 5 mm are developed for energy generation[232]. Such system is coupled with a microfiltration AEM and copper electrodes. To avoid the use of pumping systems, the solution in the reservoir is not refreshed. This miniaturized system is reported to obtain a maximum energy density of  $0.4 \text{ mJ.cm}^{-3}$  with an operation time of 3 h when connected with a 2 k $\Omega$  resistor. Considering the low energy efficiency estimated at 0.44%, system optimization is required to open up its application field. Tsai et al. reported a circular microchamber system containing a home-made Nafion microchannel with a typical surface of  $23 \times 500 \mu\text{m}^2$  and a channel length of 1-3 mm[233]. Ag/AgCl electrodes and KCl solutions of a concentration ratio of 2000:1 are used in the experiment, resulting in a maximum power density of  $755 \text{ mW.m}^{-2}$ . Chang et al. reported a pump-less paper-based RED system for power supply[234]. The unique design avoids the use of traditional pumping systems. In fact, both concentrated solution and diluted solution are driven into the paper-based system under capillary effect.

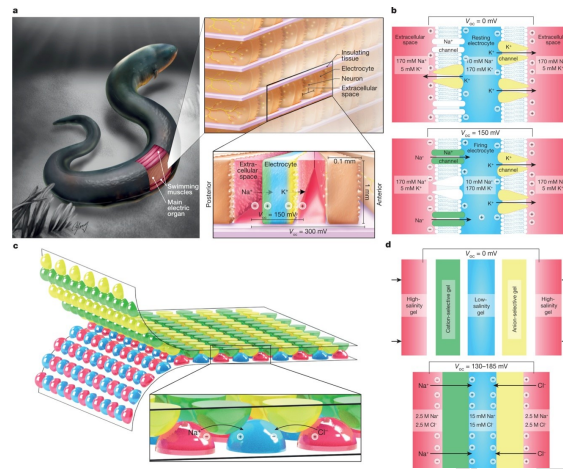


Figure 23: Morphology and mechanism of action of the eel's electric organ and the artificial electric organ. (a), *Electrophorus electricus*. The top inset shows the arrangement of electrocytes within the electric organs of *Electrophorus electricus*. The bottom inset shows ion fluxes in the firing state. (b), Mechanism of voltage generation in electrocytes. (c), Artificial electric organ in its printed implementation. (d), Mechanism of voltage generation in the artificial electric organ. Figures and captions reproduced from [229] with permission from Springer Nature, copyright 2017.

Based on a specific channel design, the injection flow rates are maintained at a constant level. This unique design reduces the system cost and enables a practical integrated power supply device. Despite the low power density ( $275 \text{ nW.cm}^{-2}$ ) reported in the work, such system presents a rather high operating time (1h), which presents potentials in powering disposable and cost-less analytical devices.

Lin et al. developed a hydrogel-based RED system, comprising two agarose hydrogel chambers with different potassium chloride concentrations and a cation-selective gellan gum membrane[237]. The RED system is fully designed with bio-compatible materials and presents an open-circuit voltage of 177 mV. In this work, the first TENG-RED combined system is reported. An auxiliary TENG system based on Chitosan/glycerol and PTFE materials as tribolayers is developed. The TENG system serves as the charging component while connected with a full-wave rectifier. A maximum charging voltage of RED system is reported at 350 mV.

Informative signals are delivered by electrons in a traditional electronic circuit. However, in biologic systems, information transmission is realized by ions and molecules. The concept of iontronics is positioned between these two systems, where only ions are used for signal transmission in polyelectrolyte gels or electrolytes in aqueous solutions[238]. Currently, various ionic components are extensively studied to

complete the iontronic toolbox[239, 197, 240]. The development of iontronics aims to realize biocompatible information processors to open up the possibility of biological communications directly with living organs[240]. Hopefully, based on this neuron-like and biocommunicable system, an aqueous computer could be developed in the future.

One of the essential obstacles is to design stable and bio compatible power supply systems. The integration of conventional electronic power generators requires the use of electrodes, where faradaic reactions and interfacial resistances could hinder its practical use. In this case, miniaturized electrodeless RED systems become an excellent candidate to power ionic circuits. Han et al. firstly reported a RED-driven complete iontronic circuit as a polyelectrolyte diode[235]. As illustrated in Figure 24(a), a 25-IEM-packed RED system serves as the power supply of an ionic diode composed of a pair of positively charged poly(diallyldimethylammonium chloride) (pDADMAC) and negatively charged poly(2-acrylamido-2-methyl-1-propanesulfonic acid) (pAMPSA) prepared on a microfluidic chip. A flexible and ion-conducting tube is used for the connection between RED and chip. Experimental results demonstrate the forward bias state and reverse bias state of the ionic diode powered by miniaturized RED system. The combination of 2 ionic diodes enables the creation of a logic OR gate, which is also experimen-

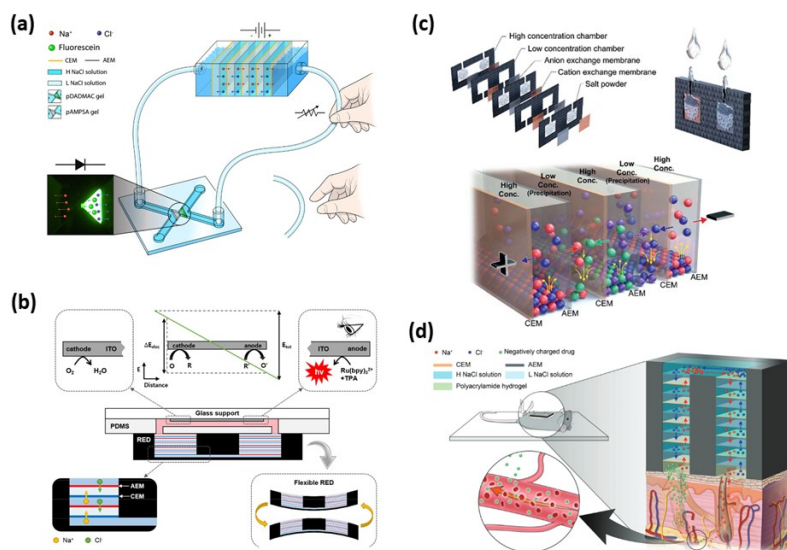


Figure 24: Miniaturized RED-integrated ionic devices, analytical sensors and biomedical applications. (a), Illustrative schematic of ionic circuit powered by RED. Voltage generated from RED is applied to microfluidic polyelectrolyte diode directly via tubes filled with electrolyte. Figure and captions reproduced from [235] with permission from Springer Nature, copyright 2017. (b), Schematic Design of the RED-Powered Biosensing System. Figure and captions reproduced from [196] with permission from American Chemical Society, copyright 2018. (c), Schematic diagram of ssRED composition, its working principle and the activation process. Entry of water through inlets and dissolution of solid salts in high concentration chambers activate the ssRED. Figure and captions reproduced from [236] with permission from Royal Society of Chemistry, copyright 2018. (d), Schematic representation of the electrodeless RED patch attached on the mouse skin. Figure and captions reproduced from [198] with permission from John Wiley and Sons, copyright 2018.

tally demonstrated in the work.

Miniaturized RED systems could become an excellent candidate for power supply of disposable biosensors and microfluidic analytical devices. They possess the advantages of direct ionic flow creation, along with an instant electrical potential difference establishment and IEM stack based scaling up potential, which could be directly integrated into analytical devices to provide electrical energy.

The electrochemiluminescence (ECL)-based bioanalysis platform is a powerful analytical tool while combining with bipolar electrodes (BPE). While faradaic reactions appear on bipolar electrodes under external voltage, the ECL signals could provide information concerning the quantitative analytes on BPE surface. As demonstrated in Figure 24(b), Baek et al. introduced the use of patch-type mini RED systems to power such platform in an electrode-less and environment-friendly way[196]. The direct ionic flow creation by RED system could avoid the voltage drop and faradaic reaction problems in conventional battery power supply. An integrated analyti-

cal system for glucose detection, coupled with RED stack powering system, was demonstrated in their work. The work of Yeon et al., has further promoted the development of disposable solid salt RED (ssRED) power source[236]. They designed a one-shot water-activated RED source where two kinds of salts ( $\text{Ag}_2\text{SO}_4/\text{BaCl}_2$ ) are used alternatively in high concentration chambers (Figure 24(c)). The activation step requires simply the addition of water into the chambers. As CEMs and AEMs are used alternatively, ions in high concentration chambers penetrated into diluted chambers become insoluble precipitations ( $\text{AgCl}$  or  $\text{BaSO}_4$ ) through metathesis reactions. This ensures a stable concentration ratio, thus a longer operation time of the system. The integration of such system with above-explained BPE system and Ionic diodes are well demonstrated in their work.

Miniaturized RED systems are also widely used in skin-wearable biomedical devices. As presented in the work of Kwon et al., patch-type RED stacks are designed to power active transdermal drug delivery platforms[198]. The electrodeless design of RED

patches present excellent advantages in biocompatibility and cost reduction. By adjusting the inserted number of membrane stacks, a controllable voltage is applied on the drug delivery platform to pump ionic drugs to penetrate the skin, as described in Figure 24(d). Experimental results proved the feasibility of such systems for in vitro drug delivery of 3 representative drugs. Such design could be generalized and integrated for other portable biomedical devices. Pakkaner et al. reported a miniaturized RED driven biopower cell designed for auto-powered implantable medical devices[199]. The power supply is designed to harness the concentration gradient in physiological fluids in renal artery and vein for example. This fluidic device is designed with alternative CEMs and AEMs with a concentration ratio of 7.2 g/L and 9.0 g/L and is kept at 37 °C in order to imitate in vivo conditions. The same group reported an effective way for performance amelioration of the biopower cell: an additional salt-cartridge for concentration ratio boost[241]. Polysulfone (PSf) hollow fiber membranes saturated with NaCl solutions are prepared as salt cartridge. A diluted stream is divided into diluted sub-stream, which is pumped directly into freshwater chambers, and a feed acceptor stream, which passes through the salt cartridge for salinity increase and serves as saltwater chamber reservoirs. A 3-fold increase of OCV of the cell is reported for the salt-cartridge boosted biopower system. It is to mention that although these two works present excellent potentials for miniaturized systems for biomedical applications, the feasibility of practical RED-driven implantable devices is yet to be verified by in vivo experiments.

### 6.2.2. Perspectives for RED

Considering the high energy density and the commercial viability of conventional batteries, it is possible to imagine miniaturized batteries to power small-scaled devices[242]. The tiny batteries widely used at the moment include zinc-air, zinc-silver oxide or lithium-manganese dioxide cells[243]. However, they present major disadvantages due to the necessary battery components of electrodes, electrical connectors and electrolyte. They are difficult to miniaturize due to the limitations of caustic KOH or lithium in batteries and the hazardous chemical products which presents safety problems during integration.

On the contrary, RED systems present major advantages in their small size, their electrode-related cost and redox reaction elimination, and their improved biocompatibility. This enables the integra-

tion of RED systems in sensors, wearable analytical devices and biomedical implants. Different from TENG systems where capacitive currents are generated, RED systems provide a direct ionic flow, along with an open-circuit voltage established across the membrane stack. The RED-driven ionic flow could be used to power iontronic circuits which remain an emerging hot topic today targeting the final goal of bio-communication and processing. In addition, miniaturized pump-free RED systems could also serve as energy storage systems due to the reversible procedures of electro dialysis, where desalination occurs under electricity application, and reverse electro dialysis where salt mixing is harnessed for electricity generation. In this point of view, the combination of RED and TENG system could be imagined as in the work of Lin et al[237].

In fact, as it is always possible to adapt the number of IEM stacks to reach the power output demand, what hinders the application of mini-RED systems would be the operation lifespan. In the work of Yeon et al., a loss of 10% of current efficiency is reported over several hours[236]. And in the case of a biosensor powered by a RED system, the operation time is estimated to be 15 s[196]. It is thus important to develop functional mini-RED with an elongated working time so that the device could be integrated in implantable systems.

For miniaturized RED stacks, the cost mainly comes from the CEM/AEM membrane stacks in the system. In order to power sensors and ionic circuits, a typical mini-RED of 5-20 membrane stacks is used in the literature, which corresponds to a membrane area of 10-40 cm<sup>2</sup>. The commercial membrane price is estimated to be around 1000 €·m<sup>-2</sup> for the widely used commercial brand Nafion. This indicates that the cost of a mini-RED would be around 1-4 €, which corresponds to the typical price of a disposable 1.5 V lithium battery. Considering a price reduction in the membrane research field, the price of a mini-RED could possibly be reduced to less than 1€. In this case, we can imagine economically viable and disposable mini-RED powered systems.

## 7. Summary and Comparison between the different energy harvesting modes

In this work we have reviewed five modes of energy production to power IoT sensors based on mechanical energy sources and osmotic energy sources. These systems have their advantages and disadvantages (see table 1). The four presented systems for

collecting energy from vibrations have similarities. In the three cases (piezoelectric materials, electrostrictive materials, electrets and triboelectric materials), it is possible to use these materials as simple sensors or as materials that produce electric current. It should be noted that unlike piezoelectric materials, electrets and triboelectric materials, electrostrictive materials require a voltage source to polarize them. Although this source does not consume any energy, it is an obstacle to the development of electrostrictive materials.

In all three cases, an alternating electric current is produced. This current must be rectified so that it can be used to charge a battery. Electrostrictive materials need large deformation to perform well, this is not the case for electrets, piezoelectric and triboelectric materials which are adapted to smaller deformations [29]. Note that piezoelectric materials may require high forces. Another important disadvantage of electrostrictive materials is the need to work in the presence of a high voltage. They must be placed in a capacitor with a high potential difference to function, which significantly limits their applications in the IoT field. The techniques based on electrostrictive materials are thus behind the three other types of materials.

The piezoelectric systems are systems that put forward an higher power density compared to electrets and triboelectric systems, they are therefore suitable for miniaturized systems. Totally autonomous systems have been realized [90]. However, piezoelectric materials have their own important disadvantages. Ceramics piezoelectric materials usually contain toxic products (such as lead) and are brittle. Plus, they require high forces. However recent results obtained on polymers[67] are intriguing because of the high power they managed to produce: this could open new routes for energy-harvester design. However, these polymers are mainly perfluorinated products of restricted use in Europe. These products are classified as eternal pollutants due to their non-biodegradable character.

Triboelectric systems have the advantage of being less expensive and mechanically reliable. These points compensate for the lower power carried over compared to piezoelectric systems. The mechanisms of triboelectricity are being better understood, thanks to the work of Professor Wang's team[148, 153]. These devices are particularly well adapted for medium size energy recovery systems. It must also be noted that the materials used are not very expensive and can be biosourced. Fully autonomous

systems have been developed in many fields. Among them, major research efforts are devoted to harvesting energy from human movements (such as breathing and walking) without disturbing the movement or bothering the user. Triboelectric nanogenerators offer a broad selection of materials and structural designs, thanks to their various operational modes. Implantable and absorbable triboelectric nanogenerators can be designed using natural materials, while wearable and conformal triboelectric nanogenerators can be made using elastic electrode materials [246]. Moreover, TENGs with distinct structures can be custom-designed to match specific regions of the human body that require suitable binding sites [247].

In the last part, we present more preliminary works concerning the recovery of osmotic energy. These works have not yet reached the maturity of the studies on the recovery of mechanical energy but remain promising. Unlike previous systems, reverse electro-dialysis devices produce a direct current that does not need to be rectified. After maturation, osmotic energy would become an important energy source because of all its possibilities and particularities. Small-scale applications already begin to spread over biology and chemistry applications. Compared to other types of sensors and nanogenerators that already existed, it offers a new type of solution for energy harvesting. Several research examples are mentioned above for directly using the ionic current or the potential to enhance a designed behaviour. Some researchers are even thinking about using ionic current and diode-like effect [248] of semi-permeable membranes to create logic circuit. It could lead in the coming years to a new type of information and calculation support and even to the ionic computer.

A simple price evaluation of mini-RED devices estimates a cost around 1 €. This considers the current membrane price and RED performances. The later is very low mostly due to concentration polarization phenomena. As explained, researchers start to study this effect with simulations and electrical measurements. This open problem is maybe a greater challenge to work on. Between single-pore devices and commercial porous membrane, a power density of the order of  $10^6 \text{ W.m}^{-2}$  is reduced by 6 orders of magnitude. If a way of suppressing or at least reducing the concentration polarization is found, the mini-RED device price could be reduced by the same 6 order of magnitude. That would make the osmotic energy an incomparably dense and easy way to generate ionic or electric current.

Technology	Piezoelectricity	Electrostriction	Electrets	Triboelectricity	Osmotic energy
Energy source	Mechanical	Mechanical	Mechanical	Mechanical	Osmotic
Advantages	Mature Technology, easy to scale down by using nanomaterials	Low cost, low weight, compatible with micro-fabrication	Low cost, stable performance, permanent polarization and good biocompatibility	Low cost, implantable device, bio-compatible systems	Direct current, bio-compatible systems
Limitations	Rectification of the current required, pooling, toxic compound (Lead, Perfluorated polymers), ceramics are brittle, need relatively large forces to deform piezoelectric materials	Rectification of the current required, need pre-charge or biasing voltage, large strain required	Rectification of the current required, material have finite lifetime due to slow loss of charges	Rectification of the current required, humidity, low output impedance, energy difficult to store	Technology currently under development, currently high cost

Table 1: Comparison of the different nanotechnologies for energy harvesting.

Most of the nanogenerators presented here collect energy efficiently. It should be noted that all these systems are a long way from commercialization. Comparing these different techniques remains difficult. Different parameters are needed to judge the efficiency of a device. At the application level, power density per volume or per surface is the parameter of choice.

Table 2 compiles recovered power values. An initial analysis can focus on the performances measured, even if they are under very different conditions. The best performance in the literature concerns piezoelectric crystals [41], and generally speaking, the best performances are achieved with the different piezoelectric materials. Electrets have capacities very close to those of triboelectric materials. However, this classification is strongly influenced by the framework of the experiments carried out. Even the indicated volume or surface is not the same for the various work : some authors refer to the whole device, while others refer only to the volume or surface of these active material. As an example, while the devices of ref [225] and [245] work under continuous flow, the device of [232] works with finite volumes of solutions without flow.

To be able to compare systems with each other, you need standardized examples of use. There is an

example of an emblematic device that allows the comparison of the recovered powers: the sole of a shoe. In this context, the results obtained with electrostrictive polymers are two orders of magnitude higher than the other systems [29]. 0.8 W are generated with an electrostrictive sole[115] while 5 mW are generated with a piezoelectric sole [65] and between 1 mW [174] and 5 mW [244] with a triboelectric sole. When the devices are at smaller scales and the solicitations are less important, the performances regrouping the piezoelectric and the triboelectric materials can for example exceed the results of performing electrostrictive materials [102]. Here we make an important point. The size of the device that can recover energy is an important parameter for choosing the material. In the case of large devices undergoing strong deformation, electrostrictive materials are preferable. Conversely, for smaller objects (cm<sup>2</sup> size), piezoelectricity, triboelectricity or even osmotic energy are recommended.

## 8. Perspectives

The analysis we have just carried out enables us to outline the prospects for energy recovery for the IOT. We think that the 3 following axis are key points: Performance characterization, Performance enhancement , Industrial manufacturing processes. In the

Technology	Reference	Power or Energy density by unit surface or volume	Volume (V) or Area (A) of the device	Frequency of the vibrations
Piezoelectricity	[62]	$70 \mu\text{W.cm}^{-3}$	$V = 1 \text{ cm}^3$	100 Hz
Piezoelectricity	[63]	$800 \mu\text{W.cm}^{-3}$	$V = 2 \text{ cm}^3$	1-10 Hz
Piezoelectricity	[41]	$55\ 000 \mu\text{W.cm}^{-3}$	$V = 1 \text{ cm}^3$	900 Hz
Piezoelectricity	[65]	$77 \mu\text{W.cm}^{-2}$	$A = 65 \text{ cm}^2$	1 Hz (sole, PZT)
Piezoelectricity	[65]	$9 \mu\text{W.cm}^{-2}$	$A = 65 \text{ cm}^2$	1 Hz (sole, PVDF)
Electrostrictive materials	[105]	$6 \mu\text{W.cm}^{-3}$	$V = 1 \text{ cm}^3$	10 Hz
Electrostrictive materials	[97]	$0.002 \mu\text{W.cm}^{-3}$	$V = 4 \text{ cm}^3$	20 Hz
Electrostrictive materials	[102]	$1 \mu\text{W.cm}^{-2}$	$A = 7.5 \text{ cm}^2$	40 Hz
Electrostrictive materials	[115]	$16\ 600 \mu\text{W.cm}^{-2}$	$A = 60 \text{ cm}^2$	1 Hz (sole)
Electrets	[135]	$1\ 210 \mu\text{W.cm}^{-2}$	$A = 3.6 \text{ cm}^2$	5 Hz
Electrets	[136]	$62.5 \mu\text{W.cm}^{-3}$	$V = 1.1 \text{ cm}^3$	125 Hz
Electrets	[138]	$1.2 \mu\text{W.cm}^{-2}$	$A = 1 \text{ cm}^2$	552 Hz
Triboelectricity	[167]	$0.2 \mu\text{W.cm}^{-2}$	$A = 10 \text{ cm}^2$	2-5 Hz
Triboelectricity	[102]	$0.3 \mu\text{W.cm}^{-2}$	$A = 7.5 \text{ cm}^2$	40-60 Hz
Triboelectricity	[158]	$48\ 000 \mu\text{W.cm}^{-2}$	$A = 4 \text{ cm}^2$	3 Hz
Triboelectricity	[159]	$81.8 \mu\text{W.cm}^{-2}$	$A = 25 \text{ cm}^2$	1 Hz
Triboelectricity	[171]	$30\ 700 \mu\text{W.cm}^{-2}$	$A = 25 \text{ cm}^2$	1-10 Hz
Triboelectricity	[174]	$3.3 \mu\text{W.cm}^{-2}$	$A = 300 \text{ cm}^2$	1 Hz (sole)
Triboelectricity	[244]	$16.6 \mu\text{W.cm}^{-2}$	$A = 300 \text{ cm}^2$	1 Hz (sole)
Osmotic energy	[225]	$220 \mu\text{W.cm}^{-2}$	$A = 3 \text{ cm}^2$	-
Osmotic energy	[232]	$0.004 \mu\text{W.cm}^{-3}$	$A = 0.2 \text{ cm}^2$	-
Osmotic energy	[245]	$2\ 750 \mu\text{W.cm}^{-2}$	$A = 0.1 \text{ cm}^2$	-

Table 2: Comparison of the harvested power for different technologies. The large variety of harvested powers is difficult to interpret since there is no standard conditions or protocol (frequency, amplitude) which would enable a rigorous analysis.

following we will detail these points.

### 8.1. Performance characterization

To take this approach further, a common standard is needed to quantify, compare and evaluate the performance of nanogenerators. As presented in the text, three merit factors have been presented in the literature [99, 165, 249]. The definition of these respective factors of merit highlights the important parameters of both mechanisms (triboelectric charge for TENG, dielectric constant for electrostriction, piezoelectric coefficients). They provide guidelines for comparing and qualifying materials within the same framework, but are not sufficient to compare techniques between them. It is difficult to define standard experiments, as the different modes of loading (sliding contact, frontal contact for triboelectrics, rotation for electrets) can have a significant influence on the value of the harvested power. However, a few standard experiments where the force applied to the system is well controlled seem necessary. This could involve, for example, experiments with a cantilever whose size and frequency of displacement could be controlled and varied. This type of experiment is suitable for electrets, piezoelectric, triboelectric and electrostrictive materials. Beyond these standard tests, we believe that the best way is to define and use an efficiency parameter  $\eta$  defined as the ratio of the output energy  $E_{out}$  by the input energy  $E_{int}$ ,  $\eta = \frac{E_{out}}{E_{int}}$ . Some data are displayed in the literature or in this article [165], but this approach has to become the rule. This parameter must be calculated in the presence and absence of energy storage.

### 8.2. Performance enhancement

One of the most important criteria is the increase in power. At the present stage of research, it seems that variations in materials will only allow incremental increases in power. It seems to us that the breakthrough must come from the coupled use of different energy recovery mechanisms. By hybridizing these different technologies [250] significant progress can be made. Lagomarsini et al. have developed an electrostrictive device [251] that does not require an external polarization voltage. Instead, they utilize the charge generated by the piezoelectric material when subjected to external mechanical excitation as the polarization source for the Dielectric Elastomer Generator (DEG). They have created two distinct prototypes: one employing a piezoelectric ceramic as the polarization element of an acrylic-based DEG,

and the other using a piezoelectric polymer. To ensure perfect mechanical and electrical synchronization, a smart frame is incorporated. These prototypes demonstrate a noteworthy level of scavenged energy density, reaching up to  $1 \mu\text{J.g}^{-1}$  and  $0.39 \mu\text{J.g}^{-1}$ , respectively. Moreover, compared to existing solutions in the literature, these devices are compact and eliminate the need for external polarization voltage. The use of devices drawing on different energy sources can make it possible to take better advantage of the environment. To overcome the weather-dependent limitations of solar cells, it is possible to integrate a solar cell with a TENG (triboelectric nanogenerator). This will permit to continually harness energy from the environment. The TENG in the device developed by Zhang et al [252], made of a transparent and flexible polymer material, serves both as a component of the triboelectric nanogenerator and as a protective coating for the solar cells.

### 8.3. Industrial manufacturing processes

Most of the energy recovery systems presented in this review are unique systems developed in laboratories. If we are to make progress in this field, we need to move on to the industrialization of these systems. This requires the implementation of large-scale production protocols (roll-to-roll techniques for manufacturing materials), the search for inexpensive, non-toxic materials available in large quantities, and the implementation of material and quality control protocols. In this context, the MEMS approach is surely the most advanced, since it can benefit from electronics standards. Accelerated system ageing tests need to be introduced. Conditions of resistance to humidity, heat and cold must be clearly identified. This approach must also define marketing standards and norms, and enable buyers to understand how much power they will be able to recover according to the demands made on them. Without this, the market will remain a niche market.

### Acknowledgment

NW acknowledges funding from China Scholarship Council (CSC). TD acknowledges funding from the Institut Pierre-Gilles de Gennes (laboratoire d'excellence PSL).

### Credit Author Statement

Nan Wu, Timothée Derkenne, Corentin Trégouët, Anne Colin wrote, reviewed and edited the

manuscript. Annie Colin supervised the redaction of the manuscript.

### Conflicts of interest

There are no conflicts to declare.

### References

- [1] K. Rose, S. Eldridge, L. Chapin, The internet of things: An overview, *The internet society (ISOC)* 80 (2015) 1–50.
- [2] H. Kopetz, W. Steiner, Internet of things, in: *Real-time systems: design principles for distributed embedded applications*, Springer, 2022, pp. 325–341.
- [3] J. Gubbi, R. Buyya, S. Marusic, M. Palaniswami, Internet of things (iot): A vision, architectural elements, and future directions, *Future generation computer systems* 29 (7) (2013) 1645–1660.
- [4] Iot market by component (hardware, software solutions and services), organization size, focus area (smart manufacturing), smart energy and utilities and smart retail) and region- global forecasts to 2026, Tech. Rep. TC 2895, *Marketsandmarkets* (feb 2022).
- [5] V. M. Rohokale, N. R. Prasad, R. Prasad, A cooperative internet of things (iot) for rural healthcare monitoring and control, in: *2011 2nd international conference on wireless communication, vehicular technology, information theory and aerospace & electronic systems technology (Wireless VITAE)*, IEEE, 2011, pp. 1–6.
- [6] A. Faure, M. Harfi, A. Naboulet, É. Tranier, C. Kirchner, *Le monde de l’Internet des objets : Des dynamiques à maîtriser*, Tech. rep., France Stratégie (Feb. 2022).
- [7] T. Sanislav, G. D. Mois, S. Zeadally, S. C. Folea, Energy harvesting techniques for internet of things (iot), *IEEE Access* 9 (2021) 39530–39549.
- [8] M. Seok, S. Hanson, Y.-S. Lin, Z. Foo, D. Kim, Y. Lee, N. Liu, D. Sylvester, D. Blaauw, The phoenix processor: A 30pw platform for sensor applications, in: *2008 IEEE Symposium on VLSI Circuits*, IEEE, 2008, pp. 188–189.
- [9] Y.-S. Lin, D. Sylvester, D. Blaauw, An ultra low power 1v, 220nw temperature sensor for passive wireless applications, in: *2008 IEEE custom integrated circuits conference*, IEEE, 2008, pp. 507–510.
- [10] S. Boisseau, G. Despesse, B. A. Seddik, Electrostatic conversion for vibration energy harvesting, in: M. Lallart (Ed.), *Small-Scale Energy Harvesting*, IntechOpen, Rijeka, 2012, Ch. 5. doi:10.5772/51360. URL <https://doi.org/10.5772/51360>
- [11] K. Yoshikawa, H. Kawasaki, W. Yoshida, T. Irie, K. Konishi, K. Nakano, T. Uto, D. Adachi, M. Kanematsu, H. Uzu, et al., Silicon heterojunction solar cell with interdigitated back contacts for a photoconversion efficiency over 26%, *Nature energy* 2 (5) (2017) 1–8.
- [12] C. Williams, R. B. Yates, Analysis of a micro-electric generator for microsystems, sensors and actuators A: *Physical* 52 (1-3) (1996) 8–11.
- [13] S. D. Moss, O. R. Payne, G. A. Hart, C. Ung, Scaling and power density metrics of electromagnetic vibration energy harvesting devices, *Smart Materials and Structures* 24 (2) (2015). doi:10.1088/0964-1726/24/2/023001.
- [14] N. Y. Yip, D. Brogioli, H. V. Hamelers, K. Nijmeijer, Salinity gradients for sustainable energy: primer, progress, and prospects, *Environmental science & technology* 50 (22) (2016) 12072–12094.
- [15] N. Wu, Y. Brahmi, A. Colin, Fluidics for energy harvesting: from nano to milli scales, *Lab on a Chip* 23 (7) (2023) 1034–1065.
- [16] M. Lallart, *Small-scale energy harvesting, BoD–Books on Demand*, 2012.
- [17] S. P. Beeby, T. O’Donnell, *Electromagnetic energy harvesting, Energy Harvesting Technologies* (2009) 129–161.
- [18] M. Geisler, S. Boisseau, M. Perez, I. Ait-Ali, S. Perraud, Scaling effects in a non-linear electromagnetic energy harvester for wearable sensors, in: *Journal of Physics: Conference Series*, Vol. 773, IOP Publishing, 2016, p. 012044.

- [19] D. Liu, Y. Gao, L. Zhou, J. Wang, Z. L. Wang, Recent advances in high-performance triboelectric nanogenerators, *Nano Research* (2023) 1–20.
- [20] W. Akram, Q. Chen, G. Xia, J. Fang, A review of single electrode triboelectric nanogenerators, *Nano Energy* (2022) 108043.
- [21] S. A. Lone, K. C. Lim, K. Kaswan, S. Chatterjee, K.-P. Fan, D. Choi, S. Lee, H. Zhang, J. Cheng, Z.-H. Lin, Recent advancements for improving the performance of triboelectric nanogenerator devices, *Nano Energy* 99 (2022) 107318.
- [22] J. Zhu, M. Zhu, Q. Shi, F. Wen, L. Liu, B. Dong, A. Haroun, Y. Yang, P. Vachon, X. Guo, et al., Progress in teng technology—a journey from energy harvesting to nanoenergy and nanosystem, *EcoMat* 2 (4) (2020) e12058.
- [23] N. Sezer, M. Koç, A comprehensive review on the state-of-the-art of piezoelectric energy harvesting, *Nano energy* 80 (2021) 105567.
- [24] C. Covaci, A. Gontean, Piezoelectric energy harvesting solutions: A review, *Sensors* 20 (12) (2020) 3512.
- [25] M. Safaei, H. A. Sodano, S. R. Anton, A review of energy harvesting using piezoelectric materials: state-of-the-art a decade later (2008–2018), *Smart materials and structures* 28 (11) (2019) 113001.
- [26] K. Uchino, The development of piezoelectric materials and the new perspective, in: *Advanced Piezoelectric Materials*, Elsevier, 2017, pp. 1–92.
- [27] Y. Zhao, L.-J. Yin, S.-L. Zhong, J.-W. Zha, Z.-M. Dang, Review of dielectric elastomers for actuators, generators and sensors, *Iet Nanoelectrics* 3 (4) (2020) 99–106.
- [28] M. Lallart, P.-J. Cottinet, D. Guyomar, L. Lebrun, Electrostrictive polymers for mechanical energy harvesting, *Journal of Polymer Science Part B: Polymer Physics* 50 (8) (2012) 523–535.
- [29] X. Yuan, S. Changgeng, G. Yan, Z. Zhenghong, Application review of dielectric electroactive polymers (deaps) and piezoelectric materials for vibration energy harvesting, in: *Journal of Physics: Conference Series*, Vol. 744, IOP Publishing, 2016, p. 012077.
- [30] Z. Zhang, L. Wen, L. Jiang, Nanofluidics for osmotic energy conversion, *Nature Reviews Materials* 6 (7) (2021) 622–639.
- [31] G. Laucirica, M. E. Toimil-Molares, C. Trautmann, W. Marmisollé, O. Azzaroni, Nanofluidic osmotic power generators—advanced nanoporous membranes and nanochannels for blue energy harvesting, *Chemical Science* 12 (39) (2021) 12874–12910.
- [32] J. Curie, P. Curie, Développement par compression de l'électricité polaire dans les cristaux hémiedres à faces inclinées, *Bulletin de minéralogie* 3 (4) (1880) 90–93.
- [33] J. Yang, et al., An introduction to the theory of piezoelectricity, Vol. 9, 2005.
- [34] R. M. Martin, Piezoelectricity, *Physical Review B* 5 (4) (1972) 1607.
- [35] W. G. Cady, Piezoelectricity: Volume Two: An Introduction to the Theory and Applications of Electromechanical Phenomena in Crystals, Courier Dover Publications, 2018.
- [36] J. I. Roscow, H. Pearce, H. Khanbareh, S. Kar-Narayan, C. R. Bowen, Modified energy harvesting figures of merit for stress-and strain-driven piezoelectric systems, *The European Physical Journal Special Topics* 228 (2019) 1537–1554.
- [37] T.-B. Xu, E. J. Siochi, J. H. Kang, L. Zuo, W. Zhou, X. Tang, X. Jiang, Energy harvesting using a pzt ceramic multilayer stack, *Smart Materials and Structures* 22 (6) (2013) 065015.
- [38] P. Muralt, M. Marzencki, B. Belgacem, F. Calame, S. Basrour, Vibration energy harvesting with pzt micro device, *Procedia Chemistry* 1 (1) (2009) 1191–1194.
- [39] Y. Liu, Y. Chang, E. Sun, F. Li, S. Zhang, B. Yang, Y. Sun, J. Wu, W. Cao, Significantly enhanced energy-harvesting performance and superior fatigue-resistant behavior in [001] c-textured batio<sub>3</sub>-based lead-free piezoceramics, *ACS applied materials & interfaces* 10 (37) (2018) 31488–31497.

- [40] Z. Vakulov, A. Geldash, D. Khakhulin, M. V. Il'ina, O. I. Il'in, V. S. Klimin, V. N. Dzhuplin, B. G. Konoplev, Z. He, O. A. Ageev, Piezoelectric energy harvester based on linbo3 thin films, *Materials* 13 (18) (2020) 3984.
- [41] A. Badel, A. Benayad, E. Lefeuvre, L. Lebrun, C. Richard, D. Guyomar, Single crystals and nonlinear process for outstanding vibration-powered electrical generators, *IEEE transactions on ultrasonics, ferroelectrics, and frequency control* 53 (4) (2006) 673–684.
- [42] Z. Yang, J. Zu, Comparison of pzn-pt, pmn-pt single crystals and pzt ceramic for vibration energy harvesting, *Energy Conversion and Management* 122 (2016) 321–329.
- [43] L. Lu, W. Ding, J. Liu, B. Yang, Flexible pvdf based piezoelectric nanogenerators, *Nano Energy* 78 (2020) 105251.
- [44] S. Sukumaran, S. Chatbouri, D. Rouxel, E. Tisserand, F. Thiebaud, T. Ben Zineb, Recent advances in flexible pvdf based piezoelectric polymer devices for energy harvesting applications, *Journal of Intelligent Material Systems and Structures* 32 (7) (2021) 746–780.
- [45] M. Koç, L. Paralı, O. Şan, Fabrication and vibrational energy harvesting characterization of flexible piezoelectric nanogenerator (pen) based on pvdf/pzt, *Polymer Testing* 90 (2020) 106695.
- [46] K. T. Arul, M. Ramanjaneyulu, M. R. Rao, Energy harvesting of pzt/pmma composite flexible films, *Current Applied Physics* 19 (4) (2019) 375–380.
- [47] P. Zhang, W. Zhang, L. Deng, H. Zhang, A triboelectric nanogenerator based on temperature-stable high dielectric batio3-based ceramic powder for energy harvesting, *Nano Energy* 87 (2021) 106176.
- [48] T. Wu, Y. Song, Z. Shi, D. Liu, S. Chen, C. Xiong, Q. Yang, High-performance nanogenerators based on flexible cellulose nanofibril/mos2 nanosheet composite piezoelectric films for energy harvesting, *Nano Energy* 80 (2021) 105541.
- [49] R. Rai, I. Coondoo, R. Lopes, I. Bdikin, R. Ayouchi, S. Bhattacharaya, R. Schwarz, A. Kholkin, Development of lead-free materials for piezoelectric energy harvesting, *MRS Online Proceedings Library (OPL) 1325* (2011) mrss11–1325–e06–03.
- [50] H. Li, C. Tian, Z. D. Deng, Energy harvesting from low frequency applications using piezoelectric materials, *Applied physics reviews* 1 (4) (2014) 041301.
- [51] W. A. Smith, New opportunities in ultrasonic transducers emerging from innovations in piezoelectric materials, in: *New Developments in Ultrasonic Transducers and Transducer Systems*, Vol. 1733, SPIE, 1992, pp. 3–26.
- [52] S. N. Cha, J.-S. Seo, S. M. Kim, H. J. Kim, Y. J. Park, S.-W. Kim, J. M. Kim, Sound-driven piezoelectric nanowire-based nanogenerators, *Advanced materials* 22 (42) (2010) 4726–4730.
- [53] A. Erturk, D. J. Inman, *Piezoelectric energy harvesting*, John Wiley & Sons, 2011.
- [54] Z. L. Wang, J. Song, Piezoelectric nanogenerators based on zinc oxide nanowire arrays, *Science* 312 (5771) (2006) 242–246.
- [55] Z. L. Wang, Piezotronic and piezophototronic effects, *The Journal of Physical Chemistry Letters* 1 (9) (2010) 1388–1393.
- [56] H. Yuan, T. Lei, Y. Qin, R. Yang, Flexible electronic skins based on piezoelectric nanogenerators and piezotronics, *Nano Energy* 59 (2019) 84–90.
- [57] H.-K. Park, K. Y. Lee, J.-S. Seo, J.-A. Jeong, H.-K. Kim, D. Choi, S.-W. Kim, Charge-generating mode control in high-performance transparent flexible piezoelectric nanogenerators, *Advanced Functional Materials* 21 (6) (2011) 1187–1193.
- [58] B. Kumar, S.-W. Kim, Energy harvesting based on semiconducting piezoelectric zno nanostructures, *Nano Energy* 1 (3) (2012) 342–355.
- [59] X. Wang, J. Song, J. Liu, Z. L. Wang, Direct-current nanogenerator driven by ultrasonic waves, *Science* 316 (5821) (2007) 102–105.
- [60] N. E. Dutoit, B. L. Wardle, S.-G. Kim, Design considerations for mems-scale piezoelectric mechanical vibration energy harvesters, *Integrated ferroelectrics* 71 (1) (2005) 121–160.

- [61] D. Lin, M. Guo, K. H. Lam, K. W. Kwok, H. Chan, Lead-free piezoelectric ceramic ( $\text{K}_0.5\text{Na}_0.5\text{NbO}_3$ ) with  $\text{MnO}_2$  and  $\text{K}_0.4\text{Cu}_1.3\text{Ta}_{1.0}\text{O}_{29}$  doping for piezoelectric transformer application, *Smart materials and structures* 17 (3) (2008) 035002.
- [62] S. Roundy, P. K. Wright, J. Rabaey, A study of low level vibrations as a power source for wireless sensor nodes, *Computer communications* 26 (11) (2003) 1131–1144.
- [63] S. R. Platt, S. Farritor, K. Garvin, H. Haider, The use of piezoelectric ceramics for electric power generation within orthopedic implants, *IEEE/ASME transactions on mechatronics* 10 (4) (2005) 455–461.
- [64] A. Chang, C. Uy, X. Xiao, X. Xiao, J. Chen, Self-powered environmental monitoring via a triboelectric nanogenerator, *Nano Energy* 98 (2022) 107282. doi:<https://doi.org/10.1016/j.nanoen.2022.107282>. URL <https://www.sciencedirect.com/science/article/pii/S2211285522003615>
- [65] C. J. Kendall, Parasitic power collection in shoe mounted devices, Ph.D. thesis, Citeseer (1998).
- [66] S. Li, J. Yuan, H. Lipson, Ambient wind energy harvesting using cross-flow fluttering (2011).
- [67] N. Godard, L. Alliol, A. Latour, S. Glinsek, M. Gérard, J. Polesel, F. D. Dos Santos, E. Defay, 1-mw vibration energy harvester based on a cantilever with printed polymer multilayers, *Cell Reports Physical Science* 1 (6) (2020) 100068.
- [68] Q. Liao, Z. Zhang, X. Zhang, M. Mohr, Y. Zhang, H.-J. Fecht, Flexible piezoelectric nanogenerators based on a fiber/zno nanowires/paper hybrid structure for energy harvesting, *Nano Research* 7 (2014) 917–928.
- [69] W. Qin, T. Li, Y. Li, J. Qiu, X. Ma, X. Chen, X. Hu, W. Zhang, A high power zno thin film piezoelectric generator, *Applied Surface Science* 364 (2016) 670–675.
- [70] H. Toshiyoshi, S. Ju, H. Honma, C.-H. Ji, H. Fujita, Mems vibrational energy harvesters, *Science and technology of advanced materials* 20 (1) (2019) 124–143.
- [71] J. C. Park, J. Y. Park, Y.-P. Lee, Modeling and characterization of piezoelectric  $d_{33}$ -mode mems energy harvester, *Journal of Microelectromechanical Systems* 19 (5) (2010) 1215–1222.
- [72] T. Tsukamoto, Y. Umino, S. Shiomi, K. Yamada, T. Suzuki, Bimorph piezoelectric vibration energy harvester with flexible 3d meshed-core structure for low frequency vibration, *Science and technology of advanced materials* 19 (1) (2018) 660–668.
- [73] D. Bhattacharya, S. Bayan, R. K. Mitra, S. K. Ray, 2d ws 2 embedded pvdf nanocomposites for photosensitive piezoelectric nanogenerators with a colossal energy conversion efficiency of 25.6%, *Nanoscale* 13 (37) (2021) 15819–15829.
- [74] A. Tamang, S. K. Ghosh, S. Garain, M. M. Alam, J. Haerberle, K. Henkel, D. Schmeisser, D. Mandal, Dna-assisted  $\beta$ -phase nucleation and alignment of molecular dipoles in pvdf film: a realization of self-poled bioinspired flexible polymer nanogenerator for portable electronic devices, *ACS applied materials & interfaces* 7 (30) (2015) 16143–16147.
- [75] S. K. Karan, R. Bera, S. Paria, A. K. Das, S. Maiti, A. Maitra, B. B. Khatua, An approach to design highly durable piezoelectric nanogenerator based on self-poled pvdf/alo-rgo flexible nanocomposite with high power density and energy conversion efficiency, *Advanced Energy Materials* 6 (20) (2016) 1601016.
- [76] R. Hidalgo-Leon, J. Urquizo, C. E. Silva, J. Silva-Leon, J. Wu, P. Singh, G. Soriano, Powering nodes of wireless sensor networks with energy harvesters for intelligent buildings: A review, *Energy Reports* 8 (2022) 3809–3826.
- [77] N. R. Alluri, B. Saravanakumar, S.-J. Kim, Flexible, hybrid piezoelectric film ( $\text{BaTi}_{1-x}\text{Zr}_x\text{O}_3$ )/pvdf nanogenerator as a self-powered fluid velocity sensor, *ACS applied materials & interfaces* 7 (18) (2015) 9831–9840.
- [78] M. Shim, J. Kim, J. Jeong, S. Park, C. Kim, Self-powered 30  $\mu\text{W}$  to 10 mW piezoelectric energy harvesting system with 9.09 ms/v maximum power point tracking time, *IEEE Journal of Solid-State Circuits* 50 (10) (2015) 2367–2379.

- [79] J. Tao, N. Viet, A. Carpinteri, Q. Wang, Energy harvesting from wind by a piezoelectric harvester, *Engineering Structures* 133 (2017) 74–80.
- [80] A. Nechibvute, A. Chawanda, P. Luhanga, Piezoelectric energy harvesting devices: An alternative energy source for wireless sensors, *Smart Materials Research* 2012 (2012) 853481. doi:10.1155/2012/853481.
- [81] Y. Hu, Z. L. Wang, Recent progress in piezoelectric nanogenerators as a sustainable power source in self-powered systems and active sensors, *Nano Energy* 14 (2015) 3–14.
- [82] D. Zhang, D. Wang, Z. Xu, X. Zhang, Y. Yang, J. Guo, B. Zhang, W. Zhao, Diversiform sensors and sensing systems driven by triboelectric and piezoelectric nanogenerators, *Coordination Chemistry Reviews* 427 (2021) 213597.
- [83] J. Zhong, Y. Ma, Y. Song, Q. Zhong, Y. Chu, I. Karakurt, D. B. Bogy, L. Lin, A flexible piezoelectret actuator/sensor patch for mechanical human–machine interfaces, *ACS nano* 13 (6) (2019) 7107–7116.
- [84] W. Deng, T. Yang, L. Jin, C. Yan, H. Huang, X. Chu, Z. Wang, D. Xiong, G. Tian, Y. Gao, et al., Cowpea-structured pvdF/zno nanofibers based flexible self-powered piezoelectric bending motion sensor towards remote control of gestures, *Nano Energy* 55 (2019) 516–525.
- [85] G. Tian, W. Deng, Y. Gao, D. Xiong, C. Yan, X. He, T. Yang, L. Jin, X. Chu, H. Zhang, et al., Rich lamellar crystal baklava-structured pzt/pvdF piezoelectric sensor toward individual table tennis training, *Nano Energy* 59 (2019) 574–581.
- [86] M. T. Chorsi, E. J. Curry, H. T. Chorsi, R. Das, J. Baroody, P. K. Purohit, H. Ilies, T. D. Nguyen, Piezoelectric biomaterials for sensors and actuators, *Advanced Materials* 31 (1) (2019) 1802084.
- [87] E. J. Curry, K. Ke, M. T. Chorsi, K. S. Wrobel, A. N. Miller III, A. Patel, I. Kim, J. Feng, L. Yue, Q. Wu, et al., Biodegradable piezoelectric force sensor, *Proceedings of the National Academy of Sciences* 115 (5) (2018) 909–914.
- [88] Z. Liu, S. Zhang, Y. Jin, H. Ouyang, Y. Zou, X. Wang, L. Xie, Z. Li, Flexible piezoelectric nanogenerator in wearable self-powered active sensor for respiration and healthcare monitoring, *Semiconductor Science and Technology* 32 (6) (2017) 064004.
- [89] Y. Hu, Y. Zhang, C. Xu, L. Lin, R. L. Snyder, Z. L. Wang, Self-powered system with wireless data transmission, *Nano letters* 11 (6) (2011) 2572–2577.
- [90] I. Jung, J. Choi, H.-J. Park, T.-G. Lee, S. Nahm, H.-C. Song, S. Kim, C.-Y. Kang, Design principles for coupled piezoelectric and electromagnetic hybrid energy harvesters for autonomous sensor systems, *Nano Energy* 75 (2020) 104921.
- [91] G.-T. Hwang, H. Park, J.-H. Lee, S. Oh, K.-I. Park, M. Byun, H. Park, G. Ahn, C. K. Jeong, K. No, et al., Self-powered cardiac pacemaker enabled by flexible single crystalline pmn-pt piezoelectric energy harvester, *Advanced materials* 26 (28) (2014) 4880–4887.
- [92] W. Y. Lionel, O. Chunlian, G. Yuandong, Inexhaustible battery: An energy harvester based battery for iot applications, in: 2018 IEEE 13th Annual International Conference on Nano/Micro Engineered and Molecular Systems (NEMS), IEEE, 2018, pp. 495–498.
- [93] H. Y. Lee, Y. Peng, Y. M. Shkel, Strain-dielectric response of dielectrics as foundation for electrostriction stresses, *Journal of Applied Physics* 98 (7) (2005) 074104.
- [94] D. Jaaoh, C. Putson, N. Muensit, Enhanced strain response and energy harvesting capabilities of electrostrictive polyurethane composites filled with conducting polyaniline, *Composites Science and Technology* 122 (2016) 97–103.
- [95] X. Yin, M. Lallart, P.-J. Cottinet, D. Guyomar, J.-F. Capsal, Mechanical energy harvesting via a plasticizer-modified electrostrictive polymer, *Applied Physics Letters* 108 (4) (2016) 042901.
- [96] J. Yuan, A. Luna, W. Neri, C. Zakri, T. Schilling, A. Colin, P. Poulin, Graphene liquid crystal retarded percolation for new high-k materials, *Nature communications* 6 (1) (2015) 1–8.

- [97] P.-J. Cottinet, D. Guyomar, B. Guiffard, C. Putson, L. Lebrun, Modeling and experimentation on an electrostrictive polymer composite for energy harvesting, *IEEE Transactions on ultrasonics, ferroelectrics, and frequency control* 57 (4) (2010) 774–784.
- [98] P.-J. Cottinet, M. Lallart, D. Guyomar, B. Guiffard, L. Lebrun, G. Sebald, C. Putsin, Analysis of ac-dc conversion for energy harvesting using an electrostrictive polymer p (vdf-trfe-cfe), *IEEE transactions on ultrasonics, ferroelectrics, and frequency control* 58 (1) (2011) 30–42.
- [99] M. Lallart, P.-J. Cottinet, L. Lebrun, B. Guiffard, D. Guyomar, Evaluation of energy harvesting performance of electrostrictive polymer and carbon-filled terpolymer composites, *Journal of applied physics* 108 (3) (2010) 034901.
- [100] M. Pruvost, W. J. Smit, C. Monteux, P. Poulin, A. Colin, Microporous electrostrictive materials for vibrational energy harvesting, *Multifunctional Materials* 1 (1) (2018) 015004.
- [101] M. Pruvost, W. J. Smit, C. Monteux, P. Poulin, A. Colin, Polymeric foams for flexible and highly sensitive low-pressure capacitive sensors, *npj Flexible Electronics* 3 (1) (2019) 7.
- [102] M. Pruvost, W. J. Smit, C. Monteux, P. Del Corro, I. Dufour, C. Ayela, P. Poulin, A. Colin, Integration of a soft dielectric composite into a cantilever beam for mechanical energy harvesting, comparison between capacitive and triboelectric transducers, *Scientific reports* 10 (1) (2020) 1–14.
- [103] Internet of things, <https://www.bosch-presse.de/pressportal/de/de/tagpage/hashtag-topic-55554.html>.
- [104] G. Moretti, G. P. R. Papini, M. Righi, D. Forehand, D. Ingram, R. Vertechy, M. Fontana, Resonant wave energy harvester based on dielectric elastomer generator, *Smart Materials and Structures* 27 (3) (2018) 035015.
- [105] H. Nesser, H. Debeda, J. Yuan, A. Colin, P. Poulin, I. Dufour, C. Ayela, All-organic microelectromechanical systems integrating electrostrictive nanocomposite for mechanical energy harvesting, *Nano Energy* 44 (2018) 1–6.
- [106] S. C. Mannsfeld, B. C. Tee, R. M. Stoltenberg, C. V. H. Chen, S. Barman, B. V. Muir, A. N. Sokolov, C. Reese, Z. Bao, Highly sensitive flexible pressure sensors with microstructured rubber dielectric layers, *Nature materials* 9 (10) (2010) 859–864.
- [107] G. Schwartz, B. C.-K. Tee, J. Mei, A. L. Appleton, D. H. Kim, H. Wang, Z. Bao, Flexible polymer transistors with high pressure sensitivity for application in electronic skin and health monitoring, *Nature communications* 4 (1) (2013) 1859.
- [108] J. Liu, G. Mao, X. Huang, Z. Zou, S. Qu, Enhanced compressive sensing of dielectric elastomer sensor using a novel structure, *Journal of Applied Mechanics* 82 (10) (2015) 101004.
- [109] H. Böse, J. Ehrlich, Dielectric elastomer sensors with advanced designs and their applications, in: *Actuators*, Vol. 12, MDPI, 2023, p. 115.
- [110] H. Böse, J. Ehrlich, T. Gerlach, T. Shinkar, D. Uhl, Dielectric elastomer strain sensors with enhanced measuring sensitivity, in: *Electroactive Polymer Actuators and Devices (EAPAD) XXIV*, Vol. 12042, SPIE, 2022, pp. 181–193.
- [111] H. Böse, D. Ocak, J. Ehrlich, Applications of pressure-sensitive dielectric elastomer sensors, in: *Electroactive Polymer Actuators and Devices (EAPAD) 2016*, Vol. 9798, SPIE, 2016, pp. 451–463.
- [112] H. Böse, D. Müller, J. Ehrlich, Operation tools with dielectric elastomer pressure sensors, in: *Electroactive Polymer Actuators and Devices (EAPAD) 2017*, Vol. 10163, SPIE, 2017, pp. 32–42.
- [113] B. Shih, D. Shah, J. Li, T. G. Thuruthel, Y.-L. Park, F. Iida, Z. Bao, R. Kramer-Bottiglio, M. T. Tolley, Electronic skins and machine learning for intelligent soft robots, *Science Robotics* 5 (41) (2020) eaaz9239.
- [114] S. Chiba, M. Waki, R. Kornbluh, R. Pelrine, Extending applications of dielectric elastomer artificial muscle, in: *Electroactive Polymer Actuators and Devices (EAPAD) 2007*, Vol. 6524, SPIE, 2007, pp. 621–625.
- [115] R. D. Kornbluh, R. Pelrine, H. Prahlad, A. Wong-Foy, B. McCoy, S. Kim, J. Eckerle,

- T. Low, From boots to buoys: promises and challenges of dielectric elastomer energy harvesting, *Electroactivity in polymeric materials* (2012) 67–93.
- [116] G. Sessler, *Electrets*, chapter 2 (1987).
- [117] H. Unz, Oliver heaviside (1850-1925), *IEEE Transactions on education* 6 (1) (1963) 30–33.
- [118] K. C. Kao, *Dielectric phenomena in solids*, Elsevier, 2004.
- [119] E. Mototarô, On dielectric polarisation, *Tokyo Sugaku-Buturigakkwai Kizi Dai 2 Ki 1* (10-11) (1919) 326–331.
- [120] M. Borisova, S. Koikov, Electret effect in dielectrics, *Soviet Physics Journal* 22 (1979) 58–69.
- [121] P. Kotrappa, Long term stability of electrets used in electret ion chambers, *Journal of electrostatics* 66 (7-8) (2008) 407–409.
- [122] P. Kotrappa, J. Dempsey, J. Hickey, L. Stieff, An electret passive environmental 222rn monitor based on ionization measurement, *Health Physics* 54 (1) (1988) 47–56.
- [123] H. Zhang, N. Liu, Q. Zeng, J. Liu, X. Zhang, M. Ge, W. Zhang, S. Li, Y. Fu, Y. Zhang, Design of polypropylene electret melt blown non-wovens with superior filtration efficiency stability through thermally stimulated charging, *Polymers* 12 (10) (2020) 2341.
- [124] Z. Xia, A. Wedel, R. Danz, Charge storage and its dynamics in porous polytetrafluoroethylene (ptfe) film electrets, *IEEE transactions on dielectrics and electrical insulation* 10 (1) (2003) 102–108.
- [125] T. Sugiyama, M. Aoyama, Y. Shibata, M. Suzuki, T. Konno, M. Ataka, H. Fujita, G. Hashiguchi, Sio<sub>2</sub> electret generated by potassium ions on a comb-drive actuator, *Applied Physics Express* 4 (11) (2011) 114103.
- [126] J. Malecki, Linear decay of charge in electrets, *Physical Review B* 59 (15) (1999) 9954.
- [127] M. Perez, S. Boisseau, P. Gasnier, J. Willemin, M. Geisler, J. Reboud, A cm scale electret-based electrostatic wind turbine for low-speed energy harvesting applications, *Smart materials and structures* 25 (4) (2016) 045015.
- [128] R. Hinchet, A. Ghaffarinejad, Y. Lu, J. Y. Hasani, S.-W. Kim, P. Basset, Understanding and modeling of triboelectric-electret nanogenerator, *Nano energy* 47 (2018) 401–409.
- [129] O. D. Jefimenko, D. K. Walker, Electrostatic current generator having a disk electret as an active element, *IEEE Transactions on Industry Applications* (6) (1978) 537–540.
- [130] Y. T. Y. Tada, Experimental characteristics of electret generator, using polymer film electrets, *Japanese journal of applied physics* 31 (3R) (1992) 846.
- [131] J. Boland, Y.-H. Chao, Y. Suzuki, Y. Tai, Micro electret power generator, in: *The Sixteenth Annual International Conference on Micro Electro Mechanical Systems, 2003. MEMS-03 Kyoto. IEEE, IEEE, 2003*, pp. 538–541.
- [132] Y. Arakawa, Y. Suzuki, N. Kasagi, Micro seismic power generator using electret polymer film, *Proc. PowerMEMS* 187 (190) (2004) 17.
- [133] H.-w. Lo, Y.-C. Tai, Parylene-based electret power generators, *Journal of Micromechanics and Microengineering* 18 (10) (2008) 104006.
- [134] J. Nakano, K. Komori, Y. Hattori, Y. Suzuki, Mems rotational electret energy harvester for human motion, in: *Journal of Physics: Conference Series, Vol. 660, IOP Publishing, 2015*, p. 012052.
- [135] B. Mahanty, S. K. Ghosh, S. Garain, D. Mandal, An effective flexible wireless energy harvester/sensor based on porous electret piezoelectric polymer, *Materials Chemistry and Physics* 186 (2017) 327–332.
- [136] H. Honma, H. Mitsuya, G. Hashiguchi, H. Fujita, H. Toshiyoshi, Improvement of energy conversion effectiveness and maximum output power of electrostatic induction-type mems energy harvesters by using symmetric comb-electrode structures, *Journal of Micromechanics and Microengineering* 28 (6) (2018) 064005.
- [137] H. Toshiyoshi, S. Ju, H. Honma, C.-H. Ji, H. Fujita, Mems vibrational energy harvesters, *Science and Technology of Advanced Materials* (Feb. 2019).

- [138] Q. Fu, Y. Suzuki, Large-dynamic-range mems electret energy harvester with combined gap-closing/overlapping-area-change electrodes, in: *Journal of Physics: Conference Series*, Vol. 476, IOP Publishing, 2013, p. 012112.
- [139] Y. Lu, M. Capocchici, Y. Leprince-Wang, P. Basset, A flexible electrostatic kinetic energy harvester based on electret films of electrospun nanofibers, *Smart Materials and Structures* 27 (1) (2017) 014001. doi:10.1088/1361-665X/aa87da. URL <https://dx.doi.org/10.1088/1361-665X/aa87da>
- [140] J. Zhu, Y. Yang, H. Zhang, Z. Zhao, T. Hu, L. Liu, More than energy harvesting in electret electronics—moving toward next-generation functional system, *Advanced Functional Materials* 33 (17) (2023) 2214859.
- [141] J. Zhu, C. Chen, X. Guo, Suspended polytetrafluoroethylene nanostructure electret film in dual variable cavities for self-powered micro-shock sensing, *Materials Research Express* 5 (4) (2018) 046305.
- [142] S. Chen, N. Wu, S. Lin, J. Duan, Z. Xu, Y. Pan, H. Zhang, Z. Xu, L. Huang, B. Hu, et al., Hierarchical elastomer tuned self-powered pressure sensor for wearable multifunctional cardiovascular electronics, *Nano Energy* 70 (2020) 104460.
- [143] B. Yu, Z. Qiao, J. Cui, M. Lian, Y. Han, X. Zhang, W. Wang, X. Yu, H. Yu, X. Wang, et al., A host-coupling bio-nanogenerator for electrically stimulated osteogenesis, *Biomaterials* 276 (2021) 120997.
- [144] A. Diaz, D. Wollmann, D. Dreblow, Contact electrification: ion transfer to metals and polymers, *Chemistry of Materials* 3 (6) (1991) 997–999.
- [145] A. Diaz, Contact electrification of materials: the chemistry of ions on polymer surfaces, *The Journal of Adhesion* 67 (1-4) (1998) 111–122.
- [146] H. Baytekin, A. Patashinski, M. Branicki, B. Baytekin, S. Soh, B. A. Grzybowski, The mosaic of surface charge in contact electrification, *Science* 333 (6040) (2011) 308–312.
- [147] C. Xu, B. Zhang, A. C. Wang, W. Cai, Y. Zi, P. Feng, Z. L. Wang, Effects of metal work function and contact potential difference on electron thermionic emission in contact electrification, *Advanced Functional Materials* 29 (29) (2019) 1903142.
- [148] Z. L. Wang, T. Jiang, L. Xu, Toward the blue energy dream by triboelectric nanogenerator networks, *Nano Energy* 39 (2017) 9–23.
- [149] J. Lowell, Contact electrification of metals, *Journal of Physics D: Applied Physics* 8 (1) (1975) 53.
- [150] Z. L. Wang, Triboelectric nanogenerator (teng)—sparking an energy and sensor revolution, *Advanced Energy Materials* 10 (17) (2020) 2000137.
- [151] W.-G. Kim, D.-W. Kim, I.-W. Tcho, J.-K. Kim, M.-S. Kim, Y.-K. Choi, Triboelectric nanogenerator: Structure, mechanism, and applications, *ACS Nano* 15 (1) (2021) 258–287.
- [152] L. S. McCarty, G. M. Whitesides, Electrostatic charging due to separation of ions at interfaces: contact electrification of ionic electrets, *Angewandte Chemie International Edition* 47 (12) (2008) 2188–2207.
- [153] Z. Wang, Y. Wang, Q. Gao, G. Bao, T. Cheng, Z. L. Wang, Triboelectric fluid sensors: Principles, development, and perspectives, *Advanced Materials Technologies* 8 (5) (2023) 2201029.
- [154] R. Zhang, H. Olin, Material choices for triboelectric nanogenerators: a critical review, *Eco-Mat* 2 (4) (2020) e12062.
- [155] Z. L. Wang, On the first principle theory of nanogenerators from Maxwell's equations, *Nano Energy* 68 (2020) 104272.
- [156] H. Zou, Y. Zhang, L. Guo, P. Wang, X. He, G. Dai, H. Zheng, C. Chen, A. C. Wang, C. Xu, et al., Quantifying the triboelectric series, *Nature Communications* 10 (1) (2019) 1–9.
- [157] J. Chen, H. Guo, C. Hu, Z. L. Wang, Robust triboelectric nanogenerator achieved by centrifugal force induced automatic working mode transition, *Advanced Energy Materials* 10 (23) (2020) 2000886.

- [158] J. Chun, B. U. Ye, J. W. Lee, D. Choi, C.-Y. Kang, S.-W. Kim, Z. L. Wang, J. M. Baik, Boosted output performance of triboelectric nanogenerator via electric double layer effect, *Nature communications* 7 (1) (2016) 1–9.
- [159] D. Kim, S.-B. Jeon, J. Y. Kim, M.-L. Seol, S. O. Kim, Y.-K. Choi, High-performance nanopatterned triboelectric generator by block copolymer lithography, *Nano Energy* 12 (2015) 331–338.
- [160] L. Cheng, Q. Xu, Y. Zheng, X. Jia, Y. Qin, A self-improving triboelectric nanogenerator with improved charge density and increased charge accumulation speed, *Nature communications* 9 (1) (2018) 3773.
- [161] W. Liu, Z. Wang, G. Wang, G. Liu, J. Chen, X. Pu, Y. Xi, X. Wang, H. Guo, C. Hu, et al., Integrated charge excitation triboelectric nanogenerator, *Nature communications* 10 (1) (2019) 1–9.
- [162] N. Cui, L. Gu, Y. Lei, J. Liu, Y. Qin, X. Ma, Y. Hao, Z. L. Wang, Dynamic behavior of the triboelectric charges and structural optimization of the friction layer for a triboelectric nanogenerator, *ACS nano* 10 (6) (2016) 6131–6138.
- [163] B. Kim, J. Y. Song, M.-c. Kim, Z.-H. Lin, D. Choi, S. M. Park, et al., All-aerosol-sprayed high-performance transparent triboelectric nanogenerator with embedded charge-storage layer for self-powered invisible security iot system and raindrop-solar hybrid energy harvester, *Nano Energy* 104 (2022) 107878.
- [164] L. Xu, T. Z. Bu, X. D. Yang, C. Zhang, Z. L. Wang, Ultrahigh charge density realized by charge pumping at ambient conditions for triboelectric nanogenerators, *Nano Energy* 49 (2018) 625–633.
- [165] Y. Zi, S. Niu, J. Wang, Z. Wen, W. Tang, Z. L. Wang, Standards and figure-of-merits for quantifying the performance of triboelectric nanogenerators, *Nature communications* 6 (1) (2015) 8376.
- [166] X. Wang, H. Zhang, L. Dong, X. Han, W. Du, J. Zhai, C. Pan, Z. L. Wang, Self-powered high-resolution and pressure-sensitive triboelectric sensor matrix for real-time tactile mapping, *Advanced materials* 28 (15) (2016) 2896–2903.
- [167] C. Wu, R. Liu, J. Wang, Y. Zi, L. Lin, Z. L. Wang, A spring-based resonance coupling for hugely enhancing the performance of triboelectric nanogenerators for harvesting low-frequency vibration energy, *Nano Energy* 32 (2017) 287–293.
- [168] S. Cui, Y. Zheng, T. Zhang, D. Wang, F. Zhou, W. Liu, Self-powered ammonia nanosensor based on the integration of the gas sensor and triboelectric nanogenerator, *Nano Energy* 49 (2018) 31–39.
- [169] K. Meng, J. Chen, X. Li, Y. Wu, W. Fan, Z. Zhou, Q. He, X. Wang, X. Fan, Y. Zhang, et al., Flexible weaving constructed self-powered pressure sensor enabling continuous diagnosis of cardiovascular disease and measurement of cuffless blood pressure, *Advanced Functional Materials* 29 (5) (2019) 1806388.
- [170] L. Liu, Q. Shi, J. S. Ho, C. Lee, Study of thin film blue energy harvester based on triboelectric nanogenerator and seashore iot applications, *Nano Energy* 66 (2019) 104167.
- [171] R. Zhang, C. Dahlström, H. Zou, J. Jonzon, M. Hummelgård, J. Örtengren, N. Blomquist, Y. Yang, H. Andersson, M. Olsen, et al., Cellulose-based fully green triboelectric nanogenerators with output power density of 300  $\text{W m}^{-2}$ , *Advanced Materials* 32 (38) (2020) 2002824.
- [172] W. Seung, H.-J. Yoon, T. Y. Kim, H. Ryu, J. Kim, J.-H. Lee, J. H. Lee, S. Kim, Y. K. Park, Y. J. Park, et al., Boosting power-generating performance of triboelectric nanogenerators via artificial control of ferroelectric polarization and dielectric properties, *Advanced Energy Materials* 7 (2) (2017) 1600988.
- [173] W. Liu, Z. Wang, G. Wang, Q. Zeng, W. He, L. Liu, X. Wang, Y. Xi, H. Guo, C. Hu, et al., Switched-capacitor-convertors based on fractal design for output power management of triboelectric nanogenerator, *Nature communications* 11 (1) (2020) 1–10.
- [174] S. Niu, X. Wang, F. Yi, Y. S. Zhou, Z. L. Wang, A universal self-charging system driven by random biomechanical energy for sustainable operation of mobile electronics, *Nature communications* 6 (1) (2015) 8975.

- [175] S. Boisseau, G. Despesse, S. Monfray, O. Puscasu, T. Skotnicki, Semi-flexible bimetal-based thermal energy harvesters, *Smart materials and structures* 22 (2) (2013) 025021.
- [176] T. Tat, A. Libanori, C. Au, A. Yau, J. Chen, Advances in triboelectric nanogenerators for biomedical sensing, *Biosensors and Bioelectronics* 171 (2021) 112714.
- [177] A. Ahmed, I. Hassan, M. F. El-Kady, A. Radhi, C. K. Jeong, P. R. Selvaganapathy, J. Zu, S. Ren, Q. Wang, R. B. Kaner, Integrated triboelectric nanogenerators in the era of the internet of things, *Advanced Science* 6 (24) (2019) 1802230.
- [178] J. Li, C. Wu, I. Dharmasena, X. Ni, Z. Wang, H. Shen, S.-L. Huang, W. Ding, Triboelectric nanogenerators enabled internet of things: A survey, *Intelligent and Converged Networks* 1 (2) (2020) 115–141.
- [179] Y. Yang, X. Guo, M. Zhu, Z. Sun, Z. Zhang, T. He, C. Lee, Triboelectric nanogenerator enabled wearable sensors and electronics for sustainable internet of things integrated green earth, *Advanced Energy Materials* 13 (1) (2023) 2203040.
- [180] Y. Zhou, M. Shen, X. Cui, Y. Shao, L. Li, Y. Zhang, Triboelectric nanogenerator based self-powered sensor for artificial intelligence, *Nano Energy* 84 (2021) 105887.
- [181] K. Zhao, G. Gu, Y. Zhang, B. Zhang, F. Yang, L. Zhao, M. Zheng, G. Cheng, Z. Du, The self-powered CO<sub>2</sub> gas sensor based on gas discharge induced by triboelectric nanogenerator, *Nano Energy* 53 (2018) 898–905.
- [182] J. Yang, J. Chen, Y. Su, Q. Jing, Z. Li, F. Yi, X. Wen, Z. Wang, Z. L. Wang, Eardrum-inspired active sensors for self-powered cardiovascular system characterization and throat-attached anti-interference voice recognition, *Advanced Materials* 27 (8) (2015) 1316–1326.
- [183] P. Bai, G. Zhu, Q. Jing, J. Yang, J. Chen, Y. Su, J. Ma, G. Zhang, Z. L. Wang, Membrane-based self-powered triboelectric sensors for pressure change detection and its uses in security surveillance and healthcare monitoring, *Advanced Functional Materials* 24 (37) (2014) 5807–5813.
- [184] F. Yi, L. Lin, S. Niu, P. K. Yang, Z. Wang, J. Chen, Y. Zhou, Y. Zi, J. Wang, Q. Liao, et al., Stretchable-rubber-based triboelectric nanogenerator and its application as self-powered body motion sensors, *Advanced Functional Materials* 25 (24) (2015) 3688–3696.
- [185] Z. Jia, B. Wang, S. Song, Y. Fan, Blue energy: Current technologies for sustainable power generation from water salinity gradient, *Renewable and Sustainable Energy Reviews* 31 (2014) 91–100. doi:10.1016/j.rser.2013.11.049.
- [186] R. S. Norman, Water salination: A source of energy, *Science* 186 (4161) (1974) 350–352. doi:10.1126/science.186.4161.350.
- [187] R. A. Tufa, S. Pawlowski, J. Veerman, K. Bouzek, E. Fontananova, G. di Profio, S. Velizarov, J. Goulão Crespo, K. Nijmeijer, E. Curcio, Progress and prospects in reverse electrodialysis for salinity gradient energy conversion and storage, *Applied Energy* 225 (2018) 290–331. doi:10.1016/j.apenergy.2018.04.111.
- [188] B. E. Logan, M. Elimelech, Membrane-based processes for sustainable power generation using water, *Nature* 488 (7411) (2012) 313–319. doi:10.1038/nature11477.
- [189] N. Y. Yip, D. Brogioli, H. V. M. Hamelers, K. Nijmeijer, Salinity gradients for sustainable energy: Primer, progress and prospects, *Environmental Science & Technology* 50 (22) (2016) 12072–12094. doi:10.1021/acs.est.6b03448.
- [190] A. Achilli, A. E. Childress, Pressure retarded osmosis: From the vision of Sidney Loeb to the first prototype installation —Review, *Desalination* 261 (3) (2010) 205–211. doi:10.1016/j.desal.2010.06.017.
- [191] S. Sarp, Z. Li, J. Saththasivam, Pressure retarded osmosis (pro): Past experiences, current developments, and future prospects, *Desalination* 389 (2016) 2–14. doi:10.1016/j.desal.2015.12.008.
- [192] J. Veerman, M. Saakes, S. Metz, G. Harmsen, Reverse electrodialysis: A validated process model for design and optimization, *Chemical Engineering Journal* 166 (1) (2011) 256–268. doi:10.1016/j.cej.2010.10.071.

- [193] A. H. Avci, R. A. Tufa, E. Fontananova, G. D. Profio, E. Curcio, Reverse electro-dialysis for energy production from natural river water and seawater, *Energy* 165 (2018) 512–521. doi:<https://doi.org/10.1016/j.energy.2018.09.111>. URL <https://www.sciencedirect.com/science/article/pii/S0360544218318759>
- [194] D. Brogioli, Extracting renewable energy from a salinity difference using a capacitor, *Physical Review Letters* 103 (5) (2009) 058501. doi:10.1103/PhysRevLett.103.058501.
- [195] T. Kim, B. E. Logan, C. A. Gorski, A ph-gradient flow cell for converting waste CO<sub>2</sub> into electricity, *Environmental Science & Technology Letters* 4 (2) (2017) 49–53. doi:10.1021/acs.estlett.6b00467.
- [196] S. Baek, S.-R. Kwon, S. Y. Yeon, S.-H. Yoon, C. M. Kang, S. H. Han, D. Lee, T. D. Chung, Miniaturized reverse electro-dialysis-powered biosensor using electrochemiluminescence on bipolar electrode, *Analytical Chemistry* 90 (7) (2018) 4749–4755. doi:10.1021/acs.analchem.7b05425.
- [197] J.-H. Han, K. B. Kim, H. C. Kim, T. D. Chung, Ionic circuits based on polyelectrolyte diodes on a microchip, *Angewandte Chemie International Edition* 48 (21) (2009) 3830–3833. doi:10.1002/anie.200900045.
- [198] S.-R. Kwon, S. H. Nam, C. Y. Park, S. Baek, J. Jang, X. Che, S. H. Kwak, Y.-R. Choi, N.-R. Park, J.-Y. Choi, Y. Lee, T. D. Chung, Electrodeless reverse electro-dialysis patches as an ionic power source for active transdermal drug delivery, *Advanced Functional Materials* 28 (15) (2018) 1705952. doi:10.1002/adfm.201705952.
- [199] E. Pakkaner, C. Smith, C. Trexler, J. Hestekin, C. Hestekin, Blood driven biopower cells: Acquiring energy from reverse electro-dialysis using sodium concentrations from the flow of human blood, *Journal of Power Sources* 488 (2021) 229440. doi:10.1016/j.jpowsour.2020.229440.
- [200] T. Luo, S. Abdu, M. Wessling, Selectivity of ion exchange membranes: A review, *Journal of Membrane Science* 555 (2018) 429–454. doi:10.1016/j.memsci.2018.03.051.
- [201] N. Wu, Y. Brahmī, A. Colin, Fluidics for energy harvesting: From nano to milli scales, *Lab on a Chip* 23 (5) (2023) 1034–1065. doi:10.1039/D2LC00946C.
- [202] F. G. Donnan, The theory of membrane equilibria., *Chemical Reviews* 1 (1) (1924) 73–90. doi:10.1021/cr60001a003.
- [203] H. Fan, Y. Huang, N. Y. Yip, Advancing ion-exchange membranes to ion-selective membranes: Principles, status, and opportunities, *Frontiers of Environmental Science & Engineering* 17 (2) (2022) 25. doi:10.1007/s11783-023-1625-0.
- [204] K. N. Mikhelson, A. Lewenstam, S. E. Didina, Contribution of the diffusion potential to the membrane potential and to the ion-selective electrode response, *Electroanalysis* 11 (10-11) (1999) 793–798. doi:10.1002/(SICI)1521-4109(199907)11:10/11<793::AID-ELAN793>3.0.CO;2-K.
- [205] Y. Oren, A. Litan, State of the solution-membrane interface during ion transport across an ion-exchange membrane, *The Journal of Physical Chemistry* 78 (18) (1974) 1805–1811. doi:10.1021/j100611a007.
- [206] F. G. Helfferich, *Ion Exchange*, Courier Corporation, 1995.
- [207] H. Strathmann, *Ion-exchange membrane separation processes*, Elsevier, 2004.
- [208] I. Rubinstein, Theory of concentration polarization effects in electro-dialysis on counter-ion selectivity of ion-exchange membranes with differing counter-ion distribution coefficients, *Journal of the Chemical Society, Faraday Transactions* 86 (10) (1990) 1857–1861. doi:10.1039/FT9908601857.
- [209] V. I. Zabolotsky, J. A. Manzanares, V. V. Nikonenko, K. A. Lebedev, E. G. Lovtsov, Space charge effect on competitive ion transport through ion-exchange membranes, *Desalination* 147 (1) (2002) 387–392. doi:10.1016/S0011-9164(02)00614-8.
- [210] C. Tang, M. L. Bruening, Ion separations with membranes, *Journal of Polymer Science* 58 (20) (2020) 2831–2856. doi:10.1002/pol.20200500.

- [211] R. abu Rjal, V. Chinaryan, M. Z. Bazant, I. Rubinstein, B. Zaltzman, Effect of concentration polarization on permselectivity, *Physical Review E* 89 (1) (2014) 012302. doi:10.1103/PhysRevE.89.012302.
- [212] P. Dlugolecki, K. Nymeijer, S. Metz, M. Wessling, Current status of ion exchange membranes for power generation from salinity gradients, *Journal of Membrane Science* 319 (1) (2008) 214–222. doi:10.1016/j.memsci.2008.03.037.
- [213] A.-L. Rollet, O. Diat, G. Gebel, A new insight into nafion structure, *The Journal of Physical Chemistry B* 106 (12) (2002) 3033–3036.
- [214] O. Stern, The theory of the electrolytic double-layer, *Z. Elektrochem* 30 (508) (1924) 1014–1020.
- [215] M. Gouy, Sur la constitution de la charge électrique à la surface d'un électrolyte, *Journal de Physique Théorique et Appliquée* 9 (1) (1910) 457–468. doi:10.1051/jphys:19100090045700.
- [216] Z. Zhang, L. Wen, L. Jiang, Nanofluidics for osmotic energy conversion, *Nature Reviews Materials* 6 (7) (2021) 622–639. doi:10.1038/s41578-021-00300-4.
- [217] S. Marbach, L. Bocquet, Osmosis, from molecular insights to large-scale applications, *Chemical Society Reviews* 48 (11) (2019) 3102–3144. doi:10.1039/C8CS00420J.
- [218] N. Y. Yip, D. A. Vermaas, K. Nijmeijer, M. Elimelech, Thermodynamic, energy efficiency and power density analysis of reverse electrodialysis power generation with natural salinity gradients, *Environmental Science & Technology* 48 (9) (2014) 4925–4936. doi:10.1021/es5005413.
- [219] A. Siria, P. Poncharal, A.-L. Bianco, R. Fulcrand, X. Blase, S. T. Purcell, L. Bocquet, Giant osmotic energy conversion measured in a single transmembrane boron nitride nanotube, *Nature* 494 (7438) (2013) 455–458. doi:10.1038/nature11876.
- [220] J. Gao, X. Liu, Y. Jiang, L. Ding, L. Jiang, W. Guo, Understanding the giant gap between single-pore- and membrane-based nanofluidic osmotic power generators, *Small* 15 (11) (2019) 1804279. doi:10.1002/smll.201804279.
- [221] R. Pattle, Production of electric power by mixing fresh and salt water in the hydroelectric pile, *Nature* 174 (1954) 660–660.
- [222] M. Turek, B. Bandura, P. Dydo, Power production from coal-mine brine utilizing reversed electrodialysis, *Desalination* 221 (1-3) (2008) 462–466.
- [223] J. Veerman, M. Saakes, S. Metz, G. Harmsen, Reverse electrodialysis: Performance of a stack with 50 cells on the mixing of sea and river water, *Journal of Membrane Science* 327 (1-2) (2009) 136–144.
- [224] D. A. Vermaas, M. Saakes, K. Nijmeijer, Doubled power density from salinity gradients at reduced intermembrane distance, *Environmental science & technology* 45 (16) (2011) 7089–7095.
- [225] Y. Brahmi, A. Colin, New membrane and electrode assembly concept to improve salinity energy harvesting., *Energy Conversion and Management* 254 (2022) 115297. doi:10.1016/j.enconman.2022.115297.
- [226] A. Daniilidis, D. A. Vermaas, R. Herber, K. Nijmeijer, Experimentally obtainable energy from mixing river water, seawater or brines with reverse electrodialysis, *Renewable energy* 64 (2014) 123–131.
- [227] A. L. Gotter, M. A. Kaetzel, J. R. Dedman, *Electrophorus electricus* as a model system for the study of membrane excitability, *Comparative Biochemistry and Physiology Part A: Molecular & Integrative Physiology* 119 (1) (1998) 225–241. doi:10.1016/S1095-6433(97)00414-5.
- [228] M. V. Brown, The electric discharge of the electric eel, *Electrical Engineering* 69 (2) (1950) 145–147. doi:10.1109/EE.1950.6434151.
- [229] T. B. H. Schroeder, A. Guha, A. Lamoureux, G. VanRenterghem, D. Sept, M. Shtein, J. Yang, M. Mayer, An electric-eel-inspired soft power source from stacked hydrogels, *Nature* 552 (7684) (2017) 214–218. doi:10.1038/nature24670.

- [230] J. Xu, D. A. Lavan, Designing artificial cells to harness the biological ion concentration gradient, *Nature Nanotechnology* 3 (11) (2008) 666–670. doi:10.1038/nano.2008.274.
- [231] P. He, J. He, Z. Huo, D. Li, Microfluidics-based fabrication of flexible ionic hydrogel batteries inspired by electric eels, *Energy Storage Materials* 49 (2022) 348–359. doi:10.1016/j.ensm.2022.04.019.
- [232] R. Banan Sadeghian, O. Pantchenko, D. Tate, A. Shakouri, Miniaturized concentration cells for small-scale energy harvesting based on reverse electrodialysis, *Applied Physics Letters* 99 (17) (2011) 173702. doi:10.1063/1.3656279.
- [233] T.-C. Tsai, C.-W. Liu, R.-J. Yang, Power generation by reverse electrodialysis in a microfluidic device with a nafion ion-selective membrane, *Micromachines* 7 (11) (2016) 205. doi:10.3390/mi7110205.
- [234] H.-K. Chang, E. Choi, J. Park, Paper-based energy harvesting from salinity gradients, *Lab on a Chip* 16 (4) (2016) 700–708. doi:10.1039/C5LC01232E.
- [235] S. H. Han, S.-R. Kwon, S. Baek, T.-D. Chung, Ionic circuits powered by reverse electrodialysis for an ultimate iontronic system, *Scientific Reports* 7 (1) (2017) 14068.
- [236] S. Y. Yeon, J. Yun, S.-h. Yoon, D. Lee, W. Jang, S. H. Han, C. M. Kang, T. D. Chung, A miniaturized solid salt reverse electrodialysis battery: A durable and fully ionic power source, *Chemical Science* 9 (42) (2018) 8071–8076. doi:10.1039/C8SC02954G.
- [237] Z.-H. Lin, W.-S. Hsu, A. Preet, L.-H. Yeh, Y.-H. Chen, Y.-P. Pao, S.-F. Lin, S. Lee, J.-C. Fan, L. Wang, Y.-P. Chiu, B.-S. Yip, T.-E. Lin, Ingestible polysaccharide battery coupled with a self-charging nanogenerator for controllable disinfection system, *Nano Energy* 79 (2021) 105440. doi:10.1016/j.nanoen.2020.105440.
- [238] M. Tepermeister, N. Bosnjak, J. Dai, X. Zhang, S. M. Kielar, Z. Wang, Z. Tian, J. Sun-tivich, M. N. Silberstein, Soft ionics: Governing physics and state of technologies, *Frontiers in Physics* (2022) 453.
- [239] K. Tybrandt, K. C. Larsson, A. Richter-Dahlfors, M. Berggren, Ion bipolar junction transistors, *Proceedings of the National Academy of Sciences* 107 (22) (2010) 9929–9932. doi:10.1073/pnas.0913911107.
- [240] P. Janson, E. O. Gabrielsson, K. J. Lee, M. Berggren, D. T. Simon, An ionic capacitor for integrated iontronic circuits, *Advanced Materials Technologies* 4 (4) (2019) 1800494. doi:10.1002/admt.201800494.
- [241] E. Pakkaner, J. L. Orton, C. G. Campbell, J. A. Hestekin, C. N. Hestekin, Development of an integrated salt cartridge-reverse electrodialysis (red) device to increase electrolyte concentrations to biomedical devices, *Membranes* 12 (10) (2022) 990. doi:10.3390/membranes12100990.
- [242] M. Zhu, O. G. Schmidt, Tiny robots and sensors need tiny batteries —Here’s How to Do It, *Nature* 589 (7841) (2021) 195–197. doi:10.1038/d41586-021-00021-2.
- [243] A. Heller, Potentially implantable miniature batteries, *Analytical and Bioanalytical Chemistry* 385 (3) (2006) 469–473. doi:10.1007/s00216-006-0326-4.
- [244] Z. Lin, Y. Wu, Q. He, C. Sun, E. Fan, Z. Zhou, M. Liu, W. Wei, J. Yang, An airtight-cavity-structural triboelectric nanogenerator-based insole for high performance biomechanical energy harvesting, *Nanoscale* 11 (14) (2019) 6802–6809.
- [245] H.-K. Chang, E. Choi, J. Park, based energy harvesting from salinity gradients, *Lab on a Chip* 16 (4) (2016) 700–708.
- [246] Y. Liu, C. Hu, Triboelectric nanogenerators based on elastic electrodes, *Nanoscale* 12 (39) (2020) 20118–20130.
- [247] Z. Li, Q. Zheng, Z. L. Wang, Z. Li, Nanogenerator-based self-powered sensors for wearable and implantable electronics, *Research* 2020 (2020).
- [248] J. Gao, W. Guo, D. Feng, H. Wang, D. Zhao, L. Jiang, High-performance ionic diode membrane for salinity gradient power generation, *Journal of the American Chemical Society* 136 (35) (2014) 12265–12272, PMID:

25137214. arXiv:<https://doi.org/10.1021/ja503692z>, doi:10.1021/ja503692z.  
URL <https://doi.org/10.1021/ja503692z>

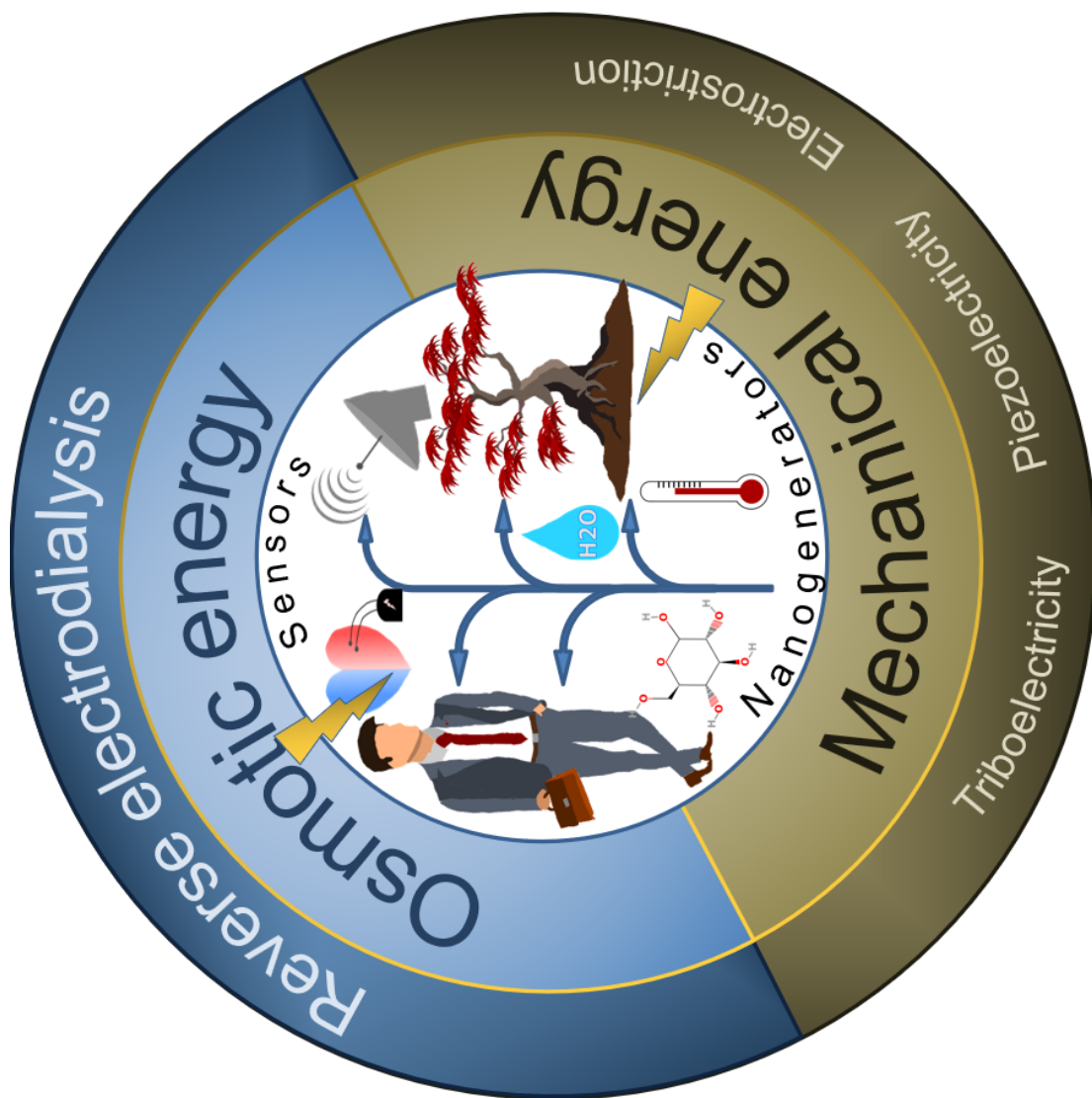
- [249] D. B. Deutz, J.-A. Pascoe, B. Schelen, S. Van Der Zwaag, D. M. De Leeuw, P. Groen, Analysis and experimental validation of the figure of merit for piezoelectric energy harvesters, *Materials Horizons* 5 (3) (2018) 444–453.
- [250] T. Zhang, T. Yang, M. Zhang, C. R. Bowen, Y. Yang, Recent progress in hybridized nanogenerators for energy scavenging, *Iscience* 23 (11) (2020) 101689.
- [251] C. Lagomarsini, C. Jean-Mistral, G. Lombardi, A. Sylvestre, Hybrid piezoelectric–electrostatic generators for wearable energy harvesting applications, *Smart Materials and Structures* 28 (3) (2019) 035003.
- [252] X.-S. Zhang, M. Han, B. Kim, J.-F. Bao, J. Brugger, H. Zhang, All-in-one self-powered flexible microsystems based on triboelectric nanogenerators, *Nano Energy* 47 (2018) 410–426.

## Highlights

### **Comparison of miniaturized mechanical and osmotic energy harvesting systems**

Nan Wu, Timothée Derkenne, Corentin Tregouet, Annie Colin

- Energy harvesting techniques to power low-power IoT devices, making them self-sustaining and eliminating the need for battery replacement or recharging are reviewed.
- Promising applications of piezoelectric nanogenerators and triboelectric nanogenerators in the field of IoT are reviewed.
- Blue energy is a source of energy for IoT.
- The performances of electrostrictive materials, triboelectric materials, piezoelectric materials and osmotic energy are compared.





Annie Colin is a professor at ESPCI Paris PSL and director of the Institut Pierre Gilles de Gennes. She is internationally recognized for her original contributions in the field of soft matter, rheology, materials for energy and microfluidics through her 160 papers and 15 patents.



Nan Wu received her bachelor's degree and master's degree from Beihang University. She received her general engineering degree from Ecole Centrale de Lyon. She currently holds a position as a Ph. D candidate at the laboratory of Matériaux Innovants pour l'Energie (MIE) in ESPCI-Paris at Paris Sciences & Lettres University (PSL). Her research focuses on developing innovative and efficient blue energy harvesting systems, especially enhancing energy harvesting efficiency of capacitive reverse electro dialysis systems. Her research interests include energy harvesting systems, capacitive reverse electro dialysis and capacitive electrodes.



Timothée Derkenne received bachelor's degree and master's degree from École Normale Supérieure de Rennes. He also received a master degree in microfluidics in the Institut Pierre Gilles de Gennes for microfluidics. He currently holds a position as a Ph. D candidate at the laboratory of Matériaux Innovants pour l'Energie (MIE) in ESPCI-Paris at Paris Sciences & Lettres University (PSL). His research focuses on transport phenomena in nanoporous materials coupled to fluid dynamics and interfaces, applied to osmotic flow for Blue Energy.



Corentin Tregouet is lecturer in the lab of Matériaux Innovants pour l'Energie (MIE) in ESPCI Paris PSL. He graduated from École Polytechnique in 2013 and defended his PhD on chemical physics in ESPCI Paris - PSL in 2016 about the interfacial rheology of microcapsules. His research focuses on transport phenomena coupled to fluid dynamics and interfaces, applied to foam and emulsion dynamics, interfacial rheology, and ionic transport in membranes.

Journal Pre-proof

Credit author statement

Nan Wu, Timothée Derkenne, Corentin Trégouët, Anne Colin wrote, reviewed and edited the manuscript.  
Annie Colin supervised the redaction of the manuscript.

Declaration of statement

**Declaration of interests**

The authors declare that they have no known competing financial interests or personal relationships that could have appeared to influence the work reported in this paper.

The authors declare the following financial interests/personal relationships which may be considered as potential competing interests:

Nan Wu reports financial support was provided by China Scholarship Council. Timothee Derkenne reports financial support was provided by PSL University.